



Swansea University
Prifysgol Abertawe

Backaction suppression in levitated optomechanics

Rafal Gajewski
Swansea University

Submitted to Swansea University in fulfillment of the requirements for the
Degree of
Doctor of Philosophy

June 2024

DECLARATION

This work has not previously been accepted in substance for any degree and is not being concurrently submitted in candidature for any degree.

Signed ... *Rafal Gajewski* (candidate)

Date... *28/02/2024*

STATEMENT 1

This thesis is the result of my own investigations, except where otherwise stated. Other sources are acknowledged by footnotes giving explicit references. A bibliography is appended.

Signed ... *Rafal Gajewski* (candidate)

Date... *28/02/2024*

STATEMENT 2

I hereby give consent for my thesis, if accepted, to be available for electronic sharing

Signed ... *Rafal Gajewski* (candidate)

Date... *28/02/2024*

STATEMENT 3

The University's ethical procedures have been followed and, where appropriate, that ethical approval has been granted.

Signed ... *Rafal Gajewski* (candidate)

Date... *28/02/2024*

Abstract

In this thesis, we show that the backaction noise acting on a small nanosphere levitated in a standing-wave trap can be considerably reduced by utilising a suitable reflective boundary. We examine the spherical mirror geometry as a case study of this backaction suppression effect, discussing the theoretical and experimental constraints. We model the backaction noise by computing the spectral density of force fluctuations acting on the particle trapped at the centre of a spherical mirror. We also compute the corresponding measurement imprecision in an interferometric, shot-noise-limited position measurement and show that backaction and imprecision agree, recovering the Heisenberg limit of detection. The remainder of the thesis is devoted to analysis and a report on the construction of two novel trapping configurations which could be used to study the backaction suppression effect.

Acknowledgements

Wanting to pursue a PhD ever since secondary school, I have largely underestimated the personal challenge that it is. When I finally got to do it in September 2020, I was lucky enough to get to work with a supervisor who would always support and keep me going. Working with James really felt like a team effort rather than a lonely venture, for which I would like to express my greatest gratitude. The progress made in this work would have been impossible without his expertise and the countless stimulating discussions we have had.

I would like to sincerely thank Kevin, who advised me and provided a grounded perspective on the whole PhD process when I needed it. For directly contributing to the research with their design expertise and the fabricated SWIFT mounts, I would like to thank James, Matthew and Paul from the Southampton Planar Optical Materials Research Group. I would be remiss in not mentioning Phil who produced the early iterations of the fibre mounts for us at the local workshop. I extend my thanks to Ardalan, Sahar and Will for helpful discussions and sharing indispensable lab equipment. Many thanks must also go to Hugh and Jonathan for helping us organise and maintain the lab. For generously allowing me to use computational resources for my simulations, I would like to acknowledge the dedicated members of the Swansea University Computer Society.

Carrying my work through to the end would have been out of the question without the support of my family and friends. Most importantly, I'm extremely grateful to my dear partner Aimee, for managing to keep me sane for the whole

duration of this project. I'm sure it wasn't easy! I am indebted to my friends Max, Laurence and especially Declan for staying in touch and absorbing my frustrations during this time. I wish them all the best on their PhD journeys that they are currently undertaking. I would also like to express deepest appreciation for my sister Paulina and her husband Mehdi. Thank you for hosting me in Plymouth several times, helping me to disconnect and have fun. Dziękuję za wszystko.

Lastly, I would like to mention my maths and physics teachers at Lipson Co-operative Academy, for their dedication to me as a student. In particular, I want to acknowledge my tutor Mr. Dale Bailey who personally helped me bridge the gap between BTEC Science and AS Physics. He didn't have to do that, but without his dedication I would have never been able to do any of this in the first place.

Contents

Abstract	1
Acknowledgements	3
1 Introduction	20
1.1 Cavity optomechanics	21
1.2 Why levitate nano-sized particles?	22
1.3 This work	24
2 Theoretical background	27
2.1 Dipole emission fields	27
2.2 Dipole scattering rate near boundaries	28
2.3 Spherical mirror Green's function	30
2.4 Dipole emission near a spherical mirror	34
2.5 Nanoparticle optical trapping	37
2.6 Particle dynamics	40
3 Backaction suppression in a structured environment	43
3.1 Problem statement	45
3.2 Measurement imprecision	47
3.2.1 Discussion	50
3.3 Measurement backaction	54
3.3.1 Single beam force noise in free-space	56
3.3.2 Force noise in front of a spherical mirror	59

3.4	Residual backaction noise	65
3.5	Other noise sources	66
3.5.1	Residual gas heating	67
3.5.2	Laser intensity noise	69
3.5.3	Laser phase noise in a standing wave	69
3.6	Concluding remarks	70
4	SMART: Spherical mirror angled-reflection trap	72
4.1	Beam reflection from a spherical mirror	73
4.2	Experimental implementation introduction	76
4.3	Laser system and trapping optics	76
4.4	Particle detection	80
4.4.1	Model of the detection signal	81
4.4.2	Detection optics	84
4.4.3	Detection methods	85
4.5	Vacuum system	87
4.6	Particle loading	87
4.7	Discussion	88
4.7.1	Trap performance	89
4.7.2	System alignment	92
4.7.3	Future improvements	93
4.8	Particle ejection by parametric excitation	97
4.9	Residual backaction noise in SMART	97
4.9.1	Influence of the SIBA force on trapping	100
5	SWIFT: Standing wave interference fibre trap	106
5.1	Trap description	106
5.2	Scatter collection efficiency	111
5.3	Particle position detection	114
5.4	Challenges and limitations	116
5.4.1	Fibre alignment	116
5.4.2	Trapping light reflection interference	118
5.4.3	Residual backaction noise in SWIFT	122

5.4.4 Residual nanoparticle charge	124
Conclusion	127
A Mathematical definitions and results	129
A.1 Mathematical definitions	129
A.2 Phase shift of focused fields	130
B Imprecision and backaction calculation details	132
B.1 Green's function derivatives	132
B.2 Solutions for perfectly reflecting mirror with varying NA . . .	133
Bibliography	135

List of Figures

2.1	Diagram depicting the geometry of the studied system - a particle with induced dipole moment \mathbf{p} at position \mathbf{r}_0 near a spherical mirror of radius $r_m = \mathbf{r}_m $ spanning an angle θ_m . The mirror is characterised by a complex reflectivity coefficient ρ .	31
2.2	Contour plot of the modified scattered power, expressed as a ratio with the free space scattering rate P/P_0 , evaluated at the mirror radius condition $kr_m = n\pi$	33
2.3	Angular spectrum representation lets us relate the 2-dimensional spatial Fourier transform $\tilde{\mathbf{E}}(k_x, k_y; z = 0)$ to fields \mathbf{E}^- and \mathbf{E}^+ evaluated on distant xy planes. If one specifies the direction of the wavevector component k_z in each halfspace, the fields \mathbf{E}^+ and \mathbf{E}^- can be related to each other. .	34
2.4	For small displacements light is approximately retroreflected, and the reflection from mirror surface maps to the other halfspace along antipodes (black dotted line). The change in phase of the outgoing scatter and its reflection is indicated by the optical path of the coloured arrows. The resulting image of the reflection appears as if it came from a source at $-\mathbf{r}_0$	36

3.1	Spherical mirror trapping configuration. A laser beam polarised out of the page is focused close to the centre of the spherical mirror, such that the beam retroreflects from the mirror surface and generates a standing wave trap. A particle is trapped at the central maximum. The remaining available solid angle not covered by the spherical mirror is used for position detection on differential detectors each covering a solid angle $d\Omega$	45
3.2	Diagram denoting different measurement domains. Since we assumed that $ \rho = 1$, no field gets transmitted and dipole emission is not accessible for measurement within domain (a). Because dipole scatter is retroreflected by the mirror surface, the mirror only affects the detected emission in domain (c). In (c), dipole emission is given by equation (3.2) and provides a self-homodyne measurement. Domain (b) corresponds to free-space dipole emission.	50
3.3	Measurement imprecision S_{imp}^i against spherical mirror half angle θ_m found by solving (3.12). Explicit solutions for the curves are given in B.2. Filled lines indicate variation at $k_0 r_m = n\pi$ and dotted lines at $k_0 r_m = n\pi \pm \pi/2$. Dashed lines indicate free-space levels in a standing wave (at $\theta_m = 0$). At $k_0 r_m = n\pi \pm \pi/4$ imprecision does not change from free-space levels with varying θ_m	51

3.4 Angular spread of position information here normalised to the total free-space imprecision $\mathcal{I}_i(\theta, \phi) = (S_{\text{imp}}^i)_{\text{free}}/dS_{\text{imp}}^i(\theta, \phi)$ from equation (3.10) . The mirror is perfectly reflecting ($\rho = -1$), has its axis of symmetry along $\hat{\mathbf{z}}$ as in figure 3.1 and was chosen to have $\theta_m = \pi/3$. The white region corresponds to domain (c) in 3.2, in which the scatter is affected by the mirror. The information in the white region of the top half-space is never accessible because this portion of the solid angle is covered by the mirror. At $k_0 r_m = n\pi$ the position information is inaccessible in the white region of both half-spaces. The colored region corresponds to free-space information. 52

3.5 Backaction noise $S_{ii}^F(\omega)$ against spherical mirror NA found by solving (3.39) with $\rho = -1$. Explicit solutions for the curves are given in B.2. Filled lines indicate backaction for $k_0 r_m = n\pi$ while dotted lines for $k_0 r_m = n\pi \pm \pi/2$. Dashed lines indicate free-space levels in a standing wave (at $\theta_m = 0$). 63

3.6 Backaction noise $S_{ii}^F(\omega)$ against displacement of the trap centre z_t along mirror axis, found by solving (3.37) to zeroth order in displacement about the trap centre. Dashed lines indicate free-space levels. Vertical lines show stable trapping positions for weak focusing ($A \approx 1$) where the solutions to (3.37) are valid approximations to backaction. 64

3.7 Threshold pressure (full red line) at which the heating rate from residual gas becomes comparable to laser recoil noise (based on equation (3.48)), plotted against trap depth for $r_p = 150$ nm and $\lambda = 1550$ nm. The red dashed lines with a shaded region denote trap depths achievable in the two experimental arrangements considered in the two arrangements considered in this thesis - the spherical mirror angled reflection trap (SMART) and the standing wave interference fibre trap (SWIFT). The teal and gray lines correspond to estimates of a trap depth based on the experimental parameters in an observation of laser recoil noise by Jain *et al.* [38,103] and Kamba *et al.* [104] respectively. We also show the corresponding threshold pressure trends using (3.48) for their experimental parameters marked with the same colours. 68

4.1 Diagram showing the difference between (right) the SMART configuration and (left) an ordinary standing wave trap formed along the mirror axis of symmetry. In both diagrams we are assuming that the beam is polarised out of the page. In the setup on the left, central region of the lens is swamped by laser retroreflection and the particle scatter cannot easily be accessed for detection. In the setup on the right, particle scatter is spatially separated from the trapping beam. In both diagrams the same portion of the solid angle is available, but it is easier to access isolated scatter when the trapping beam is angled. Because of the spherical symmetry about the mirror centre, the conditions for retroreflection in both setups are the same. . . . 73

4.2 Contribution of the Gouy phase shift of a Gaussian beam to the round-trip phase. The beam is focused to point F ($z = z_f$) about the mirror centre C ($z = 0$). The beam is reflected at M ($z = r_m$). When points C, F and M correspond to those that yield retro-reflection, the Gouy phase difference between C and M is equal to exactly $\pi/2$ 75

4.3 Implementation of the SMART arrangement, used to obtain the experimental results in this chapter. Crimson lines represent optical fibres. 10 % of the 1550 nm laser is used to seed the erbium-doped fibre amplifier (EDFA) that is then used for trapping via the trapping channel (CH1). The remaining 90 % is used either dumped or used as reference for heterodyne detection with the collected scatter via the detection channel (CH2) on the photodiode PD2. Photodiode PD1 was mainly used to assess alignment of CH1 beam by measurement of back-reflection coupled into fibre. $\lambda/2$ and $\lambda/4$ denote waveplates used to control polarisation. The local oscillator was used to modulate the trapping light's frequency for heterodyne detection, and the intensity via the acousto-optic modulators (AOMs). 77

4.4 Intensity profile of the trapping field in SMART about the beam focus - a superposition of two identical counter-propagating Gaussian beams with the waist $w_0 = 4.5 \mu\text{m}$. The beam axis is inclined at a shallow angle to the mirror axis of symmetry. On the plot x_{\parallel} and x_{\perp} denote coordinates parallel (fast) and perpendicular (slow) to the beam axis respectively. 78

4.5 Detection geometry in SMART. The lens is illuminated off-axis with trapping light \mathbf{E}_0 and focused. The trapping light is polarised out of the page along $\hat{\mathbf{y}}$. The particle, displaced from the focus by a distance $|\mathbf{r}_0| \ll f$, scatters with the field \mathbf{E}_s and detected off-axis at a distance L_d 80

List of Figures

4.6	Stochastic harmonic oscillator simulation data for simulation time of 34ms with $\Omega_x = 2\pi \times 20$ kHz, $\Omega_y = 2\pi \times 30$ kHz and $\Omega_z = 2\pi \times 300$ kHz. The temperature and the damping rate was chosen equal to $T = 300$ K and $\gamma = 2.2$ kHz respectively, which corresponds to 1 mbar environment pressure. Top: Position spectral densities of the oscillators along x, y, z . Bottom: Corresponding signal spectral density with $\theta_d = \pi/4$, a constant phase offset $\varphi = \pi/4$ and $f = 1.5$ cm.	82
4.7	Experimental spectral density of a homodyne signal captured at 1.9 mbar. Using our model we can identify the fast and slow trap frequencies to appear at about $\Omega_z = 2\pi \times 237$ kHz and $\Omega_x = 2\pi \times 17.3$ kHz respectively.	84
4.8	Signal spectra captured for a particle trapping event using the cross-homodyne reference (at 7.9 mbar) and with addition of a heterodyne reference (at 4.8 mbar) derived from the seed laser. The teal line corresponds to the heterodyne spectrum shifted down by 2 MHz for comparison. The power of both reference fields was tuned to about 10 μ W. The spectra were taken 3 minutes apart. The cross-homodyne method allowed us to consistently reach lower noise-floors compared with the other detection methods.	85
4.9	Picture of the vacuum system. The different labels denote the following components - (A) AR-coated viewport through which the laser was sent, (B) chamber door where the blue inset shows the inside of the chamber with the door open showing the optics inside the chamber, (C) flange connected to the pressure gauge ITR 90 from Leybold used to take pressure readings below 100 mbar, (D) Flange connected to the vacuum pumps.	86
4.10	Optics inside the vacuum chamber. Aluminium foil ring was fixed around the lens mount to contain the spread of the nanoparticle solution. The solution was sprayed through the narrow opening in the foil ring through a narrow tube.	88

List of Figures

4.11 Cross-homodyne signal PSD captured at 5.2×10^{-5} mbar. The bottom plots show the spectrum around the slow oscillation frequency range of Ω_x, Ω_y (bottom left) and the fast oscillations Ω_z (bottom right)	89
4.12 Series of signal spectrum snapshots captured using the cross-homodyne method during pump down from 50 mbar. Gray dashed lines are centred with the peaks in the first snapshot.	90
4.13 Simulated signal spectrum as described in section 4.4.3 with $\theta_d = \pi/4, \varphi = \pi/4$ and damping rate corresponding to 5×10^{-5} mbar and simulation time of 1.3 s. The mechanical frequencies were roughly matched to the experimental spectrum in figure 4.11 with $\Omega_x = \Omega_y = 2\pi \times 18.5$ kHz and $\Omega_z = 2\pi \times 230$ kHz.	92
4.14 CH1 back-coupled power of the reflected beam against time.	93
4.15 CH1 back-coupled power of the reflected beam during pump down from atmospheric pressure to about 1 mbar. At the end, the pressure was brought back to atmospheric.	94
4.16 Simulated intensity profile of a Gaussian beam of $NA = 0.3$ incident upon a perfectly reflecting hemispherical mirror of radius r_m . The mirror radius was varied $20\lambda \leq r_m \leq 20.5\lambda$, keeping the point to which the Gaussian beam was focused to fixed at $z_F^-(r_m = 20\lambda)$. The simulation was performed using the software suite SCUFF-EM [116, 117] implementing the boundary element method for scattering problems.	96
4.17 Series of signal spectrum snapshots demonstrating the result of parametric excitation procedure. The blue lines denote the modulation frequency during the snapshot. The modulation frequency was slowly ramped down from 38 kHz to 33 kHz at $\sim 10^{-4}$ mbar pressure.	98

4.18 Trapping forces acting on a silica nanosphere of radius $r_p = 150$ nm in a two counter-propagating Gaussian beams propagating along $\hat{\mathbf{y}}$. The beams are in-phase at the origin. **Top:** F_x, F_y and F_z components of the trapping force (pN) in free space **Middle:** F_x, F_y and F_z components of the trapping force (pN) including the effect of the spherical mirror **Bottom:** Slice of the contour plots for F_x, F_y and F_z . The inset figure for F_z shows the shift of the equilibrium position. 102

4.19 Trapping forces acting on a silica nanosphere of radius $r_p = 150$ nm in a two counter-propagating Gaussian beams propagating along $\hat{\mathbf{z}}$. The beams are in-phase at the origin. **Top:** F_x, F_y and F_z components of the trapping force (pN) in free space **Middle:** F_x, F_y and F_z components of the trapping force (pN) including the effect of the spherical mirror **Bottom:** Slice of the contour plots for F_x, F_y and F_z . The inset figure for F_z shows the shift of the equilibrium position. 103

4.20 Equilibrium position shift Δz and field gradient $|\partial_z \tilde{E}(\mathbf{r}_0)|^2 / (k_0 E_0)^2$ against particle radius r_p . Results are independent of laser power. As a reference for the scale on the y-axis, we note that at the focus of a weakly-focused Gaussian beam $|\partial_z \tilde{E}_x(\mathbf{r}_0)|^2 \approx (kE_0)^2$ 104

5.1	Standing wave interference fibre trap (SWIFT). The particle is trapped at the centre of a spherical mirror in an optical lattice formed by light propagating out of optical fibre endfaces. A heating element is used to stabilise mirror temperature, independently of trap position. In the octagonal arrangement, 4 orthogonal fibres are used for trapping with the other 4 used for pick-up of particle scatter. In the hexagonal arrangement, the 3 fibres are used for both trapping and pick-up of scatter. The figure also shows intensity profiles around the centre point of the hexagonal arrangement (top) and the octagonal arrangement (bottom) in the xy and xz planes relative to the coordinate system shown. For the octagonal arrangement, four orthogonal fibres are used for trapping, while the other fibres at 45° are used for pick-up of particle scatter.	107
5.2	Trap depth for laser power per fibre and fibre-centre distance in the hexagonal (left, 3 trapping fibres) and octagonal (right, 4 trapping fibres) fibre arrangements, for a silica particle with radius 150 nm. Note the different distance ranges on the x -axis, which were chosen based on the geometrical limits of the two different configurations.	108
5.3	An xy intensity profile (right) generated in a decagonal arrangement with a 5-fold symmetry of the fibres (left).	109
5.4	Testing the influence of the scattering force in the hexagonal arrangement. 100 particle trajectories from a 3d simulation of the Langevin equation which describes particle dynamics. Particles are initialised at a random position in a $(5 \mu\text{m})^3$ cube (blue circles). The red triangles show the final position of the particles 500 ms later.	110
5.5	Particle scatter fibre coupling calculation diagram	111
5.6	Particle scatter coupled into a fibre, normalised to the total scattered power in the hexagonal configuration. The plot accounts for increasing trap depth with decreasing distance L	113

List of Figures

5.7 (Top): Experimental time-trace of the particle passing through the observable region in the trap (Bottom): Signal reproducing the lineshape above based on the dependence in equation (5.8). 115

5.8 (Left) First iteration of the SWIFT mount - v-grooves drilled into a slab of aluminium using a corner of a flat end mill. (Middle) Microscope image of the v-grooves. The surface is visibly rough. (Right) Microscope image of the mount with fibres in place. 117

5.9 Fraction of total radiated power coupled into an opposing fibre separated by a distance L , measured on fibres clamped to the silicon mount. The solid line corresponds to equation (5.10) evaluated at $w_0 = 5.2 \mu\text{m}$ 118

5.10 Second iteration of the SWIFT configuration. (A) Silicon mount with micromachined trenches developed in collaboration with the Southampton Planar Optical Materials Research Group. (B) Microscope image of the mount cross-section with a fibre on the silicon substrate. (C) and (D) Microscope image of the silicon mount with the fibres in place. (E) Design of the 3d-printed outer mount used for initial delivery of fibres onto the silicon mount for alignment (F) Fibre trap in operation. Hexagonal M3 nut used as an ad-hoc clamping solution. . . . 119

5.11 Latest iteration of SWIFT for future testing. (Left): Fibres are initially aligned using translation stages and later fixed in place on the SWIFT mount using epoxy glue. (Right): fixed fibre arrangement after alignment. Fibre endfaces positioned $100 \mu\text{m}$ away from the midpoint. Fibre heights are aligned to less than $1 \mu\text{m}$ difference. 120

5.12	Trapping light reflection interference. (Left) Simulation setup. A Gaussian beam aligned with the mirror centre at a distance $d = 100\lambda$, propagating towards a patch of the simulated surface with radius $r_m = 300\lambda$. (Right) Plot of intensity modulation evaluated in a small patch of area $4\lambda^2$ around the mirror centre, plotted against mirror spanning angle θ_m . The simulation was performed using the software suite SCUFF-EM [116, 117] implementing the boundary element method for scattering problems.	121
5.13	Standing wave measurement imprecision S_{ii}^{imp} against spherical mirror NA found by solving (3.12) for a particle polarised along the mirror axis. Filled lines indicate variation with θ_m for $k_0 r_m = n\pi$. Dashed lines indicate free-space levels in a standing wave (at $\theta_m = 0$). For clarity, we note that in a standing wave, the beam axis direction does not enter the calculation.	122
5.14	Trapping forces acting on a Silica nanosphere of radius $r_p = 150$ nm in the hexagonal SWIFT configuration, with the fibres at a distance of 100 μm from the centre point. The beams are in-phase at the origin. Top: F_x, F_y and F_z components of the trapping force (pN) in free space Middle: F_x, F_y and F_z components of the trapping force (pN) including the effect of the spherical mirror Bottom: Slice of the contour plots for F_x, F_y and F_z	123
5.15	Equilibrium position shift Δz and field gradient $ \partial_z \tilde{E}(\mathbf{r}_0) ^2 / (k_0 E_0)^2$ against particle radius r_p for the hexagonal SWIFT configuration, with fibres separated by a distance 100 μm from the centre point. Results on the left and right plots show results for the positive and negative equilibrium position of the particle respectively.	124

Chapter 1

Introduction

Thorough theoretical studies from over 40 years ago, into the achievable performance of future gravitational wave detectors, elucidated the fundamental constraints on detection imposed by quantum mechanics when continuously monitoring the position of a free mass [1, 2]. In a continuous measurement, quantum fluctuations of the electromagnetic field introduce random perturbations to the motion of the mass. This *measurement backaction* places limits on the achievable measurement error, known as the standard quantum limit [3]. In recent years, technology has been reaching unprecedented displacement sensitivities approaching the fundamental limits of detection; best example being the celebrated first detection of gravitational waves at the LIGO facility in 2015 [4]. At the time, the LIGO detectors were capable of detecting a difference of 10^{-19} m/ $\sqrt{\text{Hz}}$ in the span of the two 4 km interferometer arms. Limits are also being approached by modern, relatively low-power, optomechanical devices; systems in which light strongly interacts with motion of a mechanical resonator. In the past two decades, optomechanics emerged as a promising experimental platform for detecting ultrasmall displacements on chip-sized devices for various commercial detector applications, quantum enhanced detection beyond the standard quantum limit, and potentially bringing the motion large masses into the quantum regime.

1.1 Cavity optomechanics

In the early 2000s, extension of fabrication techniques, used at the time for micromechanical devices, to the nano-scale [5] enabled fabricating high-finesse micro-cavities in various configurations deviating from the canonical example in optomechanics of an illuminated cavity with a vibrating end-mirror [6, 7]: silica micro-toroids [8, 9], periodic silicon nanobeams [10], and silicon nitride membranes [11] are notable examples.

Experiments utilising such devices have made remarkable progress in isolating and controlling the motion of the mechanical element. At sufficiently low energies typically quantum qualities become resolvable in the motion, such as quantised energy levels and zero-point fluctuations. Capitalising on the technique of cavity sideband cooling initially developed in atomic physics [12] allowed these resonators to reach exceedingly low centre-of-mass (CM) temperatures [9]. This method relies on scattering of light from a vibrating mechanical element, which modulates the phase of the scattered light at the mechanical frequency [9, 13]. In frequency domain, this generates positive (blue) and negative (red) *sidebands* in the optical spectrum. When the mechanical element scatters into a high-finesse cavity (with linewidth narrower than the mechanical frequency), the sidebands become resolvable; Cooling can be achieved by detuning the frequency of the illuminating laser to spectrally align it with the red sideband of the cavity linewidth, thereby enhancing scattering process responsible for removal of energy from the oscillator. In combination with cryogenic pre-cooling, cooling of motion down to its ground-state was eventually achieved [14].

Cavity optomechanical systems find a wide array of applications in quantum information processing, high-frequency gravitational wave detection [15] and other sensing applications [7], particularly of acceleration, force, mass. They also show promise of quantum-enhanced sensing beyond the standard quantum limit by employing squeezed light, [16–18] such as optomechanical magnetometry [19].

In context of fundamental applications, optomechanical systems offer a wide and untested parameter range for testing quantum behaviours of macroscopic

objects [7]. The extent of validity to which quantum mechanics holds on macroscopic scales was puzzling since the early days of quantum mechanics [20] and remains a long-standing open question in physics [21]. In order to probe the boundary between quantum and classical physics, great experimental effort is currently exerted with matter-wave experiments to test ever larger systems for exhibition of quantum properties [22]. In contrast to existing experiments, experimental recipe used for preparing the initial, coherent quantum state of a macroscopic optomechanical system demands cooling the system's mechanical mode to its ground state. This protocol requires extreme isolation from environmental noise and motional control. However, recent progress made in gaining quantum control over optomechanical systems may soon allow these systems to effectively investigate foundational questions pertaining to the quantum-to-classical transition in unexplored parameter regimes [23].

1.2 Why levitate nano-sized particles?

Larger systems couple more efficiently to the environment leading to a more rapid loss of quantum coherence. Cavity optomechanical systems are particularly susceptible, as the mechanical element is usually physically coupled to a larger substrate, which provides the dominating source of thermal dissipation in modern experiments [14, 24–26]. Motivated by the removal of this *clamping dissipation*, levitated particle systems were proposed [27–29] as a candidate optomechanical platforms to reach unprecedented degrees of isolation of macroscopic systems.

In *levitated optomechanics*, small dielectric particles (typically glass and around 10^{-7} m in diameter) are trapped by optical forces, (usually) in the focus of a laser beam. The particle constitutes a harmonic oscillator, vibrating at frequencies in the kHz range. Significantly larger than atoms, large masses and polarisabilities of the nanoparticles offer advantages in sensing and fundamental tests over existing experiments [30]. On the other hand, smaller than micro-scale objects, glass nanoparticles retain a simple description of a point-like dipole scatterer for typical laser wavelengths and good stability in

single-beam optical traps.

These optical traps rely on the principle of *optical tweezers*, pioneered by Ashkin and Dziedzic in their Nobel Prize-winning work in the 1970s and onwards [31–33]. Advancements to trapping in air [34] and the particle loading mechanism [35] sparked a series of achievements in the field. Crucially, cooling of particle motion in vacuum, first by utilising the scattering force of additional cooling beams [36] and later using a single beam by parametric feedback, exploiting the directional dependence of the optical gradient force [37] to CM temperatures below 1 Kelvin. The latter has been used in aid of first direct observation in levitated optomechanics of radiation pressure shot noise due to laser recoil [38] at pressures below 10^{-7} mbar. Both realise an *active* feedback scheme, in which a dynamic force acts on the trapped particle based on feedback signal that is derived from the particle position encoded in the detected particle scatter. This is in contrast to the aforementioned cavity cooling schemes which are examples of *passive* cooling techniques; that is, they do not require active experimental monitoring of the oscillator’s position to cool its motion. As originally envisioned, cavity cooling techniques were employed to cool the CM motion of trapped particles, initially achieving modest cooling performance [39], limited by laser phase noise within the cavity standing wave [40]. Employing the coherent scattering method of resolved-sideband cooling allowed researchers to overcome these limitations [41] and eventually led to the first report of ground state cooling of a trapped particle in room temperature environment [42]. This method of cavity cooling was recently used to simultaneously cool two motional degrees of freedom to their ground state [43]. Notably, ground state cooling by real-time active feedback without the use of a cavity was also later reported [44]. Unlike the previous active feedback schemes, in this case the method relies on exerting a force with feedback voltage on residual charge carried by the trapped particle in conjunction with optimal quantum control protocols.

Progress in ground-state cooling of levitated nanoparticles mark the first step in realising quantum superposition experiments with large masses, bringing the prospect of testing macroscopic superpositions with $\sim 10^6$ atomic

mass units within reach. Major steps in resolving quantum behaviours of more massive systems are being made in matter-wave interferometry experiments, in which interference of large fullerene molecules was demonstrated in a Talbot-Lau interferometer [45]. Similar experiments in recent years have demonstrated matter-wave interference of the heaviest objects to date [22]. Levitated optomechanical systems can operate under the same experimental principle. In the last decade, realistic experiments utilising levitated nano-sized spheres have been proposed [46] as one of the platforms in the pursuit of this goal and is actively pursued in the research campaign of the macroscopic quantum resonators (MAQRO) space mission [47]. In the classical regime, levitated optomechanics finds applications in non-equilibrium nano-scale thermodynamics [48], gravitational wave detection [49] with room-temperature sensors reaching force and acceleration sensitivities near the standard quantum limit [30].

The field of levitating nano-sized objects has grown into a large and diverse discipline of experimental physics. Recently, focus has also been placed on exploring the capabilities of optically trapped nano-objects of different shapes, with rotational degrees of freedom such as rods [50], torque sensor nanodumbbells [51] or hexagonal prisms for gravitational wave detection [52]. Levitated optomechanics is also established as a branch of a broader field of levitodynamics [53], using electric, magnetic, and hybridised trapping mechanisms to improve trap performance [54], cooling [44], or coupling with other degrees of freedom such as electronic spins embedded in levitated nanodiamonds [55].

1.3 This work

While the removal of the clamping mechanism enables levitated particle systems to reach extreme isolation from thermal dissipation, coherence times of the prepared motional states are limited by excessive backaction noise imposed by the measurement process. The measurement cannot be avoided so long as the trapped particle continuously scatters light of the confining laser

which reveals information about the particle's position that is encoded in the phase of the radiation. However, once the state is prepared, the measurement is not required for coherent evolution which limits experimental protocols following the preparation of the motional ground state.

The degree to which the backaction process can be controlled in levitated optomechanics without turning off the trapping light has not yet been fully explored. Recently, a recoil noise suppression method has been proposed [56] based on illumination by squeezed light [18], enabling control over the information encoded in particle scatter. A different method for limiting laser recoil relies on trapping hexagonal plates instead of spheres [52]. A different geometry of the trapped object alters its radiation pattern, thereby limiting the solid angle in which laser recoil noise can act.

In this work, we investigate an experimental scheme to suppress position information in scattered radiation by trapping the particle at the centre of a spherical mirror. Under appropriate conditions, the scheme is predicted to suppress first-order position information, thereby inhibiting the dominating contribution to mechanical noise from photon recoil. Laser recoil noise in an interferometer is not the property of the laser [1]. Instead, it can be understood as a result of interference of the laser field with the vacuum field fluctuations entering the empty port of the interferometer. In general, the vacuum fluctuations are function of the environment [57] and it is known that surfaces can lead to surface-induced noise larger than in free-space [58–60]. Here we show that a spherical geometry in conjunction with a standing wave optical trapping potential can lead to a substantial reduction in mechanical noise. This work has general implications for recoil noise reduction in a structured environment, and may aid in search for other useful configurations. We also present experimental results for two novel trapping geometries which could be used to probe the suppression effect at the centre of a spherical mirror.

The work in this thesis is organised as follows:

- **Chapter 2:** Introduction to the necessary theoretical tools and results used in the remainder of the thesis.
- **Chapter 3:** Theoretical study of the minimal measurement imprecision in an interferometric measurement of a particle's position, that is trapped in a standing wave at the centre of a spherical mirror. We find a condition necessary for suppression of first order position information and then compute the corresponding measurement backaction. We find that suppression of position information corresponds to inhibition of the dominating contribution of backaction to mechanical noise, satisfying the Heisenberg limit of detection.
- **Chapter 4:** Theoretical and experimental investigation of the spherical mirror angled reflection trap (SMART) as a platform for demonstration of the suppression effect. We study the unique feature of the SMART geometry, in which the appearance of an optical lattice trap site at the centre of the spherical mirror is coincident with the suppression condition found in the previous chapter. We present the experimental setup built during the project, and characterise the trap using experimental results. A simple theoretical model is also developed for position detection, which captures the unique spectral lineshapes acquired in the experiment.
- **Chapter 5:** A study of the standing wave interference fibre trap (SWIFT) as an alternative trapping geometry. We investigate the trap characterisation, the features of the optical potential and discuss experimental progress in its realisation. The study includes numerical analysis of particle detection on the optical fibres and trapping conditions.

Chapter 2

Theoretical background

Neutral nanoparticles are composed of many atoms and the associated charges. When the dimensions of this composite object are small compared with the wavelength of the illuminating laser light, to a good approximation the whole object interacts only with the field at its CM via its spatially-averaged dipole moment [13]. In this *dipole approximation*, the motion and emission of the nanoparticle illuminated by laser light can be modelled as that of a point-like dipole. In this chapter, we use this point-dipole model to introduce the theoretical language used to describe optical trapping forces and emission near boundaries of levitated nanoparticles. In addition, we briefly introduce the model of the trapped particle dynamics.

2.1 Dipole emission fields

Green's functions are solutions to inhomogeneous differential equations with the inhomogeneity given by a delta function. In homogeneous space, a point like dipole gives a singular inhomogeneity in the Helmholtz equation. Fields radiated by a point-like dipole are determined by the *dyadic Green's function* $\overline{\overline{\mathbf{G}}}$; a tensor of rank two which solves the equation, [13]

$$\nabla \times \nabla \times \overline{\overline{\mathbf{G}}}(\mathbf{r}, \mathbf{r}_0) - k^2 \overline{\overline{\mathbf{G}}}(\mathbf{r}, \mathbf{r}_0) = \overline{\overline{\mathbf{I}}}\delta(\mathbf{r} - \mathbf{r}_0) \quad (2.1)$$

with wavenumber $k = \omega/c$, unit dyad $\bar{\bar{\mathbf{I}}}$, source position \mathbf{r}_0 and observation point \mathbf{r} . The Green's function $\bar{\bar{\mathbf{G}}}$ is dyadic since each orientation of the dipole moment \mathbf{p} gives rise to a different three-dimensional vector field. Hence, each column of $\bar{\bar{\mathbf{G}}}$ represents dipole emission field components from a dipole moment oriented along a different orthogonal axis. For a harmonically driven dipole $\mathbf{p}(t) = \text{Re}[\mathbf{p} \exp(-i\omega t)]$ located at \mathbf{r}_0 , the complex amplitude of the electric field of dipole emission is given by,

$$\mathbf{E}(\mathbf{r}) = \frac{k^2}{\epsilon\epsilon_0} \bar{\bar{\mathbf{G}}}(\mathbf{r}, \mathbf{r}_0) \mathbf{p} \quad (2.2)$$

In free space, the solution for the Green's function is, [13]

$$\bar{\bar{\mathbf{G}}}_0(\mathbf{r}, \mathbf{r}_0) = \left[\bar{\bar{\mathbf{I}}} + \frac{1}{k^2} \nabla \nabla \right] \frac{\exp(ikr')}{4\pi r'} \quad (2.3)$$

where we wrote $r' = |\mathbf{r} - \mathbf{r}_0|$ and a direct product of two vectors corresponds to a dyadic product. In this thesis, we will be concerned with the free-space dipole emission fields evaluated far from the source position ($r' \gg \lambda$). In the far-field, Green's function terms scaling as $(kr')^{-3}$ and $(kr')^{-2}$ add a negligible contribution. Because of this, in the subsequent calculations we will make particular use of the part of $\bar{\bar{\mathbf{G}}}_0$ which scales as $(r')^{-1}$,

$$\bar{\bar{\mathbf{G}}}_{\text{ff}}(\mathbf{r}, \mathbf{r}_0) = \frac{\exp(ikr')}{4\pi r'} \left[\bar{\bar{\mathbf{I}}} - \frac{\mathbf{r}' \mathbf{r}'}{(r')^2} \right] \quad (2.4)$$

which is associated with far-field emission.

2.2 Dipole scattering rate near boundaries

The scattering rate of a point dipole emitter depends on its environment. This is easy to see by considering Poynting's theorem in the time-average where, [13]

$$\langle P \rangle = \frac{1}{2} \int_{\partial V} \text{Re}[\mathbf{E}^* \times \mathbf{H}] \cdot \mathbf{n} \, dA = -\frac{1}{2} \int_V \text{Re}[\mathbf{j}^* \cdot \mathbf{E}] \, dV, \quad (2.5)$$

which is a statement of energy conservation; total rate of energy transfer through surface ∂V is equal to the total rate of energy dissipation by the current density inside ∂V in the presence of field \mathbf{E} . When the current density is that of a point current located at \mathbf{r}_0 , $\mathbf{j}(\mathbf{r}) = -i\omega\mathbf{p}\delta(\mathbf{r} - \mathbf{r}_0)$, the right-hand side of (2.5) simplifies to, [13]

$$\langle P \rangle = \frac{6\pi P_0}{k} \mathbf{n}_p \cdot \text{Im} \left[\overline{\mathbf{G}}(\mathbf{r}_0, \mathbf{r}_0) \right] \cdot \mathbf{n}_p \quad (2.6)$$

where we introduced the dipole orientation \mathbf{n}_p and the free-space scattering rate $P_0 = |\mathbf{p}|^2 k^4 / (12\pi\epsilon_0 c)$. The scattering rate depends on the Green's function with the observation point evaluated at the position of the dipole. When in free-space $\mathbf{n}_p \cdot \overline{\mathbf{G}}_0(\mathbf{r}_0, \mathbf{r}_0) \cdot \mathbf{n}_p = ik/6\pi$, and the scattering rate reduces to $\langle P \rangle = P_0$. However, the Green's function in general is a function of the environment and is therefore subject to change. In this way surrounding boundaries can be used to either enhance or suppress the emission rate of a point-dipole relative to free-space emission. The exact details depend on the geometry and material response functions of the surrounding boundaries.

For a classical emitter, modification of the scattering rate can be viewed as due to interference of dipole emission field with its own reflection. In this picture, the particle is seen as a point dipole antenna driven by an external field. The oscillation of the current within the dipole generates the dipole emission field. The same field however, acts against the oscillating current inside the dipole which leads to energy dissipation at a rate equal to the scattering rate. When reflecting boundaries are present, the dipole current not only interacts with the driving field but also with the dipole field which has been reflected by the environment. The reflection provides an extra driving force for the dipole current, which modifies the rate of energy dissipation.

The physical significance of the quantity $\text{Im} \left[\overline{\mathbf{G}} \right]$ evaluated at the position of the source goes beyond the rate of emission by a classical emitter. The mutable character of radiative emission was originally demonstrated by Purcell in 1946 [61], who observed enhancement of emission in nuclear magnetic moment transitions coupled to a resonant circuit. This was later demonstrated in many physical configurations: spontaneous emission enhancement by Drexhage *et*

al. [62] for Eu^{+3} ions near a silver mirror, Goy *et al.* for atoms in a cavity [63], and inhibition by Kleppner [64] and others [65, 66]. This environmental dependence is expressed theoretically within Fermi's golden rule [67], which states that the rate of transition of a radiative emitter is proportional to the local density of optical states (LDOS). This density computes a spectral sum over the available optical mode frequencies ω_n , weighted by the local coupling of the optical mode amplitudes \mathcal{E}_n to the dipole orientation \mathbf{n}_p . The LDOS is a quantity directly connected to $\text{Im}[\overline{\mathbf{G}}]$ [68]. In the weak coupling regime of atom-field interactions, it can be shown that the QED treatment of emission rate by a quantum emitter is in agreement with results derived using classical electromagnetism for a classical antenna [13, 68]. In recent years, enhancement factors of order $\sim 10^1 - 10^2$ have been observed [69–71]. The field of study concerning the tailoring of the optical environment of quantum emitters and nanostructures currently enjoys a great amount of interest, due to its various applications in optics and nanophotonics [71, 72] and possibility of complete inhibition of spontaneous emission in a 3D photonic bandgap [73–75].

Electromagnetic boundaries alter the modes available in the system, and therefore modify the scattering rate. Modification of the density of states fundamentally alters the properties of vacuum fluctuations [57], which is used to explain other phenomena in various settings [76, 77], such as dispersion forces [78], Casimir interactions [59] and surfaced-induced heating in levitated optomechanics [60].

2.3 Spherical mirror Green's function

In a situation where a dipolar scatter is illuminated by an incident field \mathbf{E}_0 , we can always write the total field at any point as the sum of the incident and scattered fields $\mathbf{E} = \mathbf{E}_0 + \mathbf{E}_s$. When boundaries are present, the scattered fields in the same medium as the scatterer are a sum of free-space scatter and field reflected from the boundary $\mathbf{E}_s = \mathbf{E}_s^0 + \mathbf{E}_r$. Since each column of the dyadic Green's function $\overline{\mathbf{G}}$ quantifies the three-dimensional electric field vector of dipole emission \mathbf{E}_s for different orthogonal dipole orientations, The

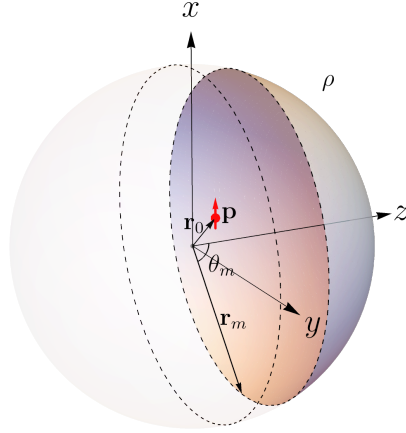


Figure 2.1: Diagram depicting the geometry of the studied system - a particle with induced dipole moment \mathbf{p} at position \mathbf{r}_0 near a spherical mirror of radius $r_m = |\mathbf{r}_m|$ spanning an angle θ_m . The mirror is characterised by a complex reflectivity coefficient ρ

Green's function can be decomposed similarly as,

$$\overline{\overline{\mathbf{G}}}(\mathbf{r}, \mathbf{r}_0) = \overline{\overline{\mathbf{G}}}_0(\mathbf{r}, \mathbf{r}_0) + \overline{\overline{\mathbf{G}}}_s(\mathbf{r}, \mathbf{r}_0) \quad (2.7)$$

where the first term corresponds to free-space emission, and the second term corresponds to the *reflected* field and depends on the boundary. Throughout this thesis, we will consider the system shown in figure 2.1, with the dipole emitter scattering at or near the centre of a spherical mirror. To find $\overline{\overline{\mathbf{G}}}_s$ at the location of the particle, we first need to model reflection of dipole emission from the mirror surface. This problem is greatly simplified when the spherical mirror radius is large ($r_m \gg \lambda$). In this case, only the far-fields from the scatter reach the mirror, and hence only the far-field component of the dyadic Green's function shown in equation (2.4) contributes to reflection.

For a large mirror, its surface is locally flat at every point on the wavelength scale. We take the origin of the coordinate system to coincide with the centre of the spherical mirror. Assuming that $|\mathbf{r}_0| \ll |\mathbf{r}|$ where \mathbf{r} is a vector to an observation point on the mirror surface, we can approximate $\hat{\mathbf{r}}' = (\mathbf{r} - \mathbf{r}_0)/|\mathbf{r} - \mathbf{r}_0|$ on the mirror surface as radial from the origin $\hat{\mathbf{r}}' \approx \mathbf{r}/|\mathbf{r}| = \hat{\mathbf{r}}$. Since the displacement is much smaller than the mirror radius, the wavevector of

the dipole field at the mirror is approximately normal at the mirror surface. Therefore, at every point, a plane-wave is at normal incidence to a plane surface, and the field upon reflection becomes,

$$\overline{\overline{\mathbf{G}}}_s(\mathbf{r}, \mathbf{r}_0) = \rho \overline{\overline{\mathbf{G}}}_{\text{ff}}(\mathbf{r}, \mathbf{r}_0) \quad (2.8)$$

where ρ is the Fresnel reflection coefficient at normal incidence between the mirror and the vacuum [79]. The spherical mirror acts like a lens and focuses the reflected fields back towards the origin. With the reflected field known on a spherical surface in the far-field, the focused reflected field at position \mathbf{s} near the origin can be expressed using angular spectrum representation as, [13, 80]

$$\overline{\overline{\mathbf{G}}}_s(\mathbf{s}, \mathbf{r}_0, \omega) = -\rho \frac{ikr_m e^{ikr_m}}{2\pi} \int_{\mathcal{M}} \overline{\overline{\mathbf{G}}}_{\text{ff}}(\mathbf{r}, \mathbf{r}_0, \omega) e^{-ik\hat{\mathbf{r}} \cdot \mathbf{s}} d\Omega \quad (2.9)$$

with $k = \omega/c$ and \mathcal{M} integration runs over the solid angle of the fields being focused, which in this case is the mirror surface. Equation (2.9) is valid since $\overline{\overline{\mathbf{G}}}_s$ is evaluated far from the mirror surface, hence evanescent wave components of the reflected field do not contribute. In the analysis of backaction noise at the centre of a spherical mirror we will use equation (2.9) expressed in terms of the free-space radiation pattern. For dipole orientation \mathbf{n}_p , the free-space radiation pattern is given by,

$$\rho_p(\theta, \phi) = \frac{3}{8\pi} (1 - (\hat{\mathbf{r}} \cdot \mathbf{n}_p)^2) \quad (2.10)$$

where $\hat{\mathbf{r}} = (\sin \theta \cos \phi, \sin \theta \sin \phi, \cos \theta)$. This allows us to express the element of the Green's function in equation (2.9) as,

$$\mathbf{n}_p \cdot \overline{\overline{\mathbf{G}}}_s(\mathbf{s}, \mathbf{r}_0, \omega) \cdot \mathbf{n}_p = -\rho \frac{ike^{2ikr_m}}{3\pi} \int_{\mathcal{M}} e^{-ik\hat{\mathbf{r}} \cdot (\mathbf{s} + \mathbf{r}_0)} \rho_p(\theta, \phi) d\Omega. \quad (2.11)$$

We can use these expressions for $\overline{\overline{\mathbf{G}}}_s$ to find how the scattered power changes with the mirror radius. Assuming the case of perfect reflection $\rho = -1$ and a full hemisphere solid angle ($\theta_m = \pi/2$), using equation (2.6) with $\mathbf{s} = \mathbf{r}_0 = (0, 0, 0)$, we find the expression for the total scattered power,

$$\langle P \rangle = 2 \cos^2(kr_m) P_0 \quad (2.12)$$

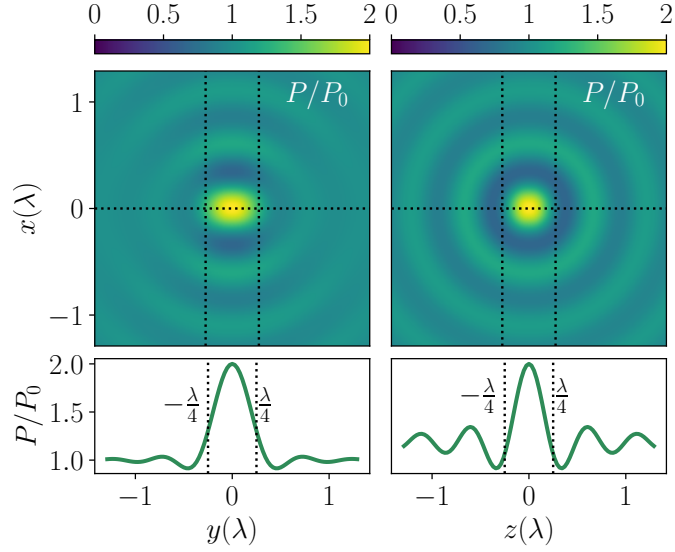


Figure 2.2: Contour plot of the modified scattered power, expressed as a ratio with the free space scattering rate P/P_0 , evaluated at the mirror radius condition $kr_m = n\pi$.

independent of dipole orientation. The result is consistent with the modified rate of spontaneous emission of an atom at the centre of a hemispherical mirror [81]. It shows that for the condition $kr_m = n\pi \pm \pi/2$ the emission can be fully suppressed for a dipole positioned at the mirror centre. On the other hand, at $kr_m = n\pi$ the dipole is predicted to radiate twice as much power. However, as in the case of a hemispherical mirror only half of the solid angle is exposed, the dipole radiates four times as much power along any angular element. In figure 2.2 we consider the total scattered power at $kr_m = n\pi$ for a dipole displaced from the mirror centre by numerically solving the angular integral in (2.9) with the observation point evaluated at the position of the particle $\mathbf{s} = \mathbf{r}_0$. In the next section, we consider the same situation by instead analysing the emission in the far-field.

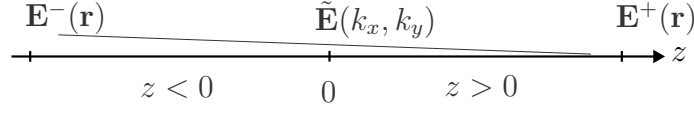


Figure 2.3: Angular spectrum representation lets us relate the 2-dimensional spatial Fourier transform $\tilde{\mathbf{E}}(k_x, k_y; z = 0)$ to fields \mathbf{E}^- and \mathbf{E}^+ evaluated on distant xy planes. If one specifies the direction of the wavevector component k_z in each halfspace, the fields \mathbf{E}^+ and \mathbf{E}^- can be related to each other.

2.4 Dipole emission near a spherical mirror

For use in later chapters, it will be useful to study the total far-fields of a point dipole, when that is located at \mathbf{r}_0 near the centre of a spherical mirror. The dipole probes the local phase of the driving field ϕ via its interaction with the incident field $\mathbf{E}(\mathbf{r}) = \mathcal{E}(\mathbf{r})e^{i\phi(\mathbf{r})}$ for a real amplitude \mathcal{E} . For $|\mathbf{r}_0| \ll \lambda \ll |\mathbf{r}|$, the far-field is specified by the Green's function $\overline{\mathbf{G}}_{\text{ff}}$ in equation (2.4) and can be approximated as,

$$\overline{\mathbf{G}}_{\text{ff}}(\mathbf{r}, \mathbf{r}_0) \approx \left[\frac{e^{ikr}}{4\pi r} \left(\overline{\mathbf{I}} - \frac{\mathbf{r}\mathbf{r}}{r^2} \right) \right] e^{-ik\hat{\mathbf{r}} \cdot \mathbf{r}_0} = \overline{\mathbf{G}}(\mathbf{r}, \mathbf{0}) e^{-ik\hat{\mathbf{r}} \cdot \mathbf{r}_0} \quad (2.13)$$

where $\mathbf{0}$ denotes the origin. In equation (2.13) we have expanded $r' = |\mathbf{r} - \mathbf{r}_0|$ to zeroth order in source position $r' \approx r$ for the amplitude and to first order for the phase $r' \approx r - \hat{\mathbf{r}} \cdot \mathbf{r}_0$. The dipole field for a particle at \mathbf{r}_0 can then be written as, [82]

$$\mathbf{E}_s(\mathbf{r}, \mathbf{r}_0) = \mathbf{E}_s(\mathbf{r}) e^{i\phi(\mathbf{r}_0)} e^{-ik\hat{\mathbf{r}} \cdot \mathbf{r}_0} \quad (2.14)$$

where \mathbf{E}_s with one position argument is the dipole emission with the dipole located at the origin. Note that we implicitly assumed harmonic time-dependence.

We are interested in computing the sum of equation (2.14) and its reflection from the spherical mirror at some point \mathbf{r}_d pointing away from the mirror where $|\mathbf{r}_d| \gg \lambda$. One could use equation (2.9) to compute the reflected field at \mathbf{r}_d but

it is simpler to relate the field at \mathbf{r}_d to the corresponding far-field on the mirror surface. This relationship exists because the angular spectrum representation allows us to relate the Fourier transform of a field on a plane to the field on another distant plane [13, 80]. This relationship ought to match on a plane which connects a positive and a negative halfspace (see figure 2.3 and the appendix section A.2). If the wavevector component $k_z < 0$ for both $z < 0$ and $z > 0$, then it can be shown that,

$$\mathbf{E}^-(\mathbf{r}) = -\mathbf{E}^+(-\mathbf{r})e^{2ikr} \quad (2.15)$$

for large r . Equation (2.15) shows that fields of a propagating beam map along antipodes with a π phase shift. One example of this is the limiting value for the Gouy phase shift of a Gaussian beam,

$$\begin{aligned} \Delta\phi &= \lim_{z \rightarrow \infty} (\phi(z) - \phi(-z)) \\ &= \lim_{z \rightarrow \infty} \left(2kz + \arctan\left(\frac{z}{z_R}\right) - \arctan\left(-\frac{z}{z_R}\right) \right) \\ &= 2kz + \pi. \end{aligned} \quad (2.16)$$

Phase shifts such as the Gouy shift are a general property of propagating fields [83] and the reflection of the dipole emission from the spherical mirror also experiences it, because the field propagates in the same direction in both half-spaces.

We now apply the result in equation (2.15) to the problem of finding the dipole emission reflected from the mirror to point \mathbf{r}_d . Since the fields map along antipodes, we find that,

$$\overline{\overline{\mathbf{G}}}_s(\mathbf{r}_d, \mathbf{r}_0) = -\frac{r_m}{r_d} e^{ik(r_m+r_d)} \overline{\overline{\mathbf{G}}}_s(\mathbf{r}_m, \mathbf{r}_0) \quad (2.17)$$

where $\mathbf{r}_m = -(r_m/r_d)\mathbf{r}_d$. Under the retroreflection approximation, the reflected field on the mirror surface at point \mathbf{r} is simply given by the far-field part of the free-space Green's function,

$$\overline{\overline{\mathbf{G}}}_s(\mathbf{r}, \mathbf{r}_0) = \rho \overline{\overline{\mathbf{G}}}_{\text{ff}}(\mathbf{r}, \mathbf{r}_0) = \rho \overline{\overline{\mathbf{G}}}_{\text{ff}}(-\mathbf{r}, -\mathbf{r}_0) \quad (2.18)$$

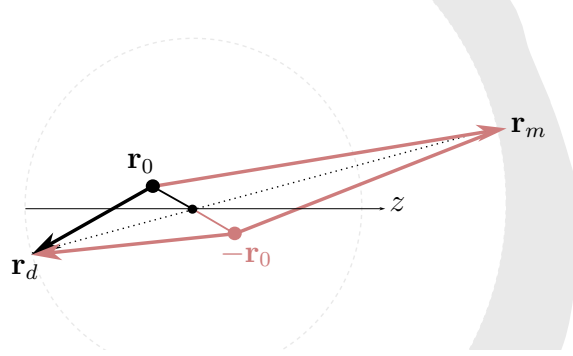


Figure 2.4: For small displacements light is approximately retroreflected, and the reflection from mirror surface maps to the other halfspace along antipodes (black dotted line). The change in phase of the outgoing scatter and its reflection is indicated by the optical path of the coloured arrows. The resulting image of the reflection appears as if it came from a source at $-\mathbf{r}_0$.

where ρ is the Fresnel reflection at normal incidence ($\rho = -1$ for a perfect reflector) and in the second equality we used the symmetry property of $\overline{\mathbf{G}}_{\text{ff}}$. Using this result and equation (2.17) we can express the Green's function of the reflected field at \mathbf{r}_d as,

$$\begin{aligned}\overline{\mathbf{G}}_s(\mathbf{r}_d, \mathbf{r}_0) &= -\rho \frac{r_m}{r_d} e^{ik(r_m+r_d)} \overline{\mathbf{G}}_{\text{ff}}((r_m/r_d)\mathbf{r}_d, -\mathbf{r}_0) \\ &= -\rho e^{2ikr_m} \overline{\mathbf{G}}_{\text{ff}}(\mathbf{r}_d, -\mathbf{r}_0)\end{aligned}\quad (2.19)$$

We see in the second line of equation (2.19) that the image of the reflected field at \mathbf{r}_d appears as if it came from a source at $-\mathbf{r}_0$ with a phase shift (see figure 2.4). Finally, adding the scattered field in (2.14) and its reflection in (2.19) results in the total field,

$$\mathbf{E}_{\text{tot}}(\mathbf{r}_d) = \mathbf{E}_s(\mathbf{r}_d) e^{i\phi(\mathbf{r}_0)} \left(e^{-ik\hat{\mathbf{r}}\cdot\mathbf{r}_0} - \rho e^{ik(\hat{\mathbf{r}}\cdot\mathbf{r}_0+2r_m)} \right) \quad (2.20)$$

where we also used (2.14) to express the mirror reflection in terms of free-space dipole emission from the source at the origin, in this case with $|\mathbf{r} - (-\mathbf{r}_0)| \approx r + \hat{\mathbf{r}} \cdot \mathbf{r}_0$ since the source appears to be located at $-\mathbf{r}_0$. Note however, that the local phase $\phi(\mathbf{r}_0)$ is the same for both free-space scatter and its reflection from the mirror, despite the image particle appearing at $-\mathbf{r}_0$. This is because

this phase is probed by the real particle at its location, and is the property of the incident field and not the Green's function. As a result, the local phase is carried as a phase offset by the reflected field. For $\rho = -1$, field in equation (2.20) reduces to,

$$\mathbf{E}_{\text{tot}}(\mathbf{r}_d) = 2\mathbf{E}_s(\mathbf{r}_d)e^{i(kr_m+\phi(\mathbf{r}_0))} \cos(k[\hat{\mathbf{r}} \cdot \mathbf{r}_0 + r_m]) \quad (2.21)$$

The expression in equation (2.21) differs from the expression found in [84] by $\pi/2$ in phase. The discrepancy seems to arise from the missing Gouy phase shift of the dipole reflection in their description. With the particle at the origin, the field is simply given by,

$$\mathbf{E}_{\text{tot}}(\mathbf{r}_d) = 2\mathbf{E}_s(\mathbf{r}_d)e^{i(kr_m+\phi(\mathbf{r}_0))} \cos(kr_m) \quad (2.22)$$

Substituting (2.22) into the left-hand side of (2.5) gives $\langle P \rangle = 2 \cos(kr_m)^2 P_0$ in agreement with equation (2.12) found in the previous section.

At $kr_m = n\pi$, (2.21) becomes independent of particle position to first order and for small displacements the particle appears to have a free-space radiation pattern. If the driving field is formed using counter-propagating beams, the local phase would appear in the amplitude. For example, in a standing wave formed with two counter-propagating plane waves along $\hat{\mathbf{x}}$, dipole emission would take the form,

$$\mathbf{E}_{\text{tot}}(\mathbf{r}_d) = 2\mathbf{E}_s(\mathbf{r}_d)e^{ikr_m} \cos(kx_0) \cos(k[\hat{\mathbf{r}} \cdot \mathbf{r}_0 + r_m]). \quad (2.23)$$

An expression of similar form will be used in the calculation of measurement imprecision in the next chapter.

2.5 Nanoparticle optical trapping

The force on a point dipole with dipole moment \mathbf{p} interacting with incident fields \mathbf{E} and \mathbf{B} is given by, [13]

$$\mathbf{F} \approx \sum_i p_i \nabla E_i + \frac{d}{dt} [\mathbf{p} \times \mathbf{B}]. \quad (2.24)$$

Assuming harmonic time dependence of the fields, in the time-average the force becomes, [13]

$$\langle \mathbf{F} \rangle = \frac{1}{2} \sum_i \text{Re} [p_i^* \nabla E_i] \quad (2.25)$$

where p_i and E_i in the above are the complex amplitudes associated with the dipole moment and the incident field respectively.

Lasers focused by an objective lens with a low numerical aperture or radiating from an end-facet of an optical fibre are well described within the paraxial approximation (small angle) by a Gaussian beam $\mathbf{E} = \mathcal{E}(\mathbf{r}) \exp(i\phi(\mathbf{r}))$ where, [85]

$$\begin{aligned} \mathcal{E}(\mathbf{r}) &= \mathbf{E}_0 \frac{w_0}{w(z)} \exp\left(-\frac{x^2 + y^2}{w(z)^2}\right) \\ \phi(\mathbf{r}) &= k \left(z + \frac{x^2 + y^2}{2R(z)} \right) - \psi(z) \end{aligned} \quad (2.26)$$

and,

$$\begin{aligned} w(z) &= w_0 \sqrt{1 + \left(\frac{z}{z_R}\right)^2} && \text{(Beam waist)} \\ R(z) &= z + \frac{z_R^2}{z} && \text{(Beam radius of curvature)} \\ \psi(z) &= \arctan\left(\frac{z}{z_R}\right) && \text{(Gouy phase shift)} \end{aligned} \quad (2.27)$$

specified by the minimum waist w_0 at beam focus and the Rayleigh range $z_R = \pi w_0^2 / \lambda$ at wavelength λ . For a field of the form $\mathbf{E} = \mathcal{E}(\mathbf{r}) \exp(i\phi(\mathbf{r}))$ together with the generally valid linear relationship $\mathbf{p} = \alpha(\omega)\mathbf{E}$, equation (2.25) can be rewritten as, [79]

$$\langle \mathbf{F} \rangle = \frac{1}{4} \text{Re} [\alpha] \nabla \mathcal{E}(\mathbf{r})^2 + \frac{1}{2} \text{Im} [\alpha] \mathcal{E}(\mathbf{r})^2 \nabla \phi(\mathbf{r}) \quad (2.28)$$

with complex polarisability α . Averaging of fields over a small dielectric sphere of radius r_p in vacuum allows to obtain the polarisability using the Clausius-Mossotti relation, [79]

$$\alpha = 4\pi r_p^3 \epsilon_0 \frac{\epsilon - 1}{\epsilon + 2} \quad (2.29)$$

where ϵ_0 is the permittivity of free space, relating the polarisability to the dielectric constant ϵ of the bulk material which makes up the sphere. Silica nanoparticles are typically used due to its low absorption at wavelengths used for trapping (1064 nm and 1550 nm). At these wavelengths, silica is non-dispersive and the dielectric constant takes the value $\epsilon \approx 2.25$ which makes α a real quantity. The imaginary part of the polarisability is associated with dissipation such as internal heating. Although silica has low absorption, its polarisability has to be supplemented with an additional term $\alpha_{\text{eff}} \approx \alpha + ik^3\alpha^2/6\pi\epsilon_0$ for wavenumber $k = 2\pi/\lambda$. This second term arises due to dipole's self emission fields within the particle which act against the oscillation of the dipole moment, leading to dissipation [13, 86].

The first term in (2.28) is the optical gradient force which acts towards the region of highest intensity and the second scattering force term acts in the direction of changing phase. In a Gaussian beam, the gradient force gives rise to a restoring force used for trapping at the beam focus. In the context of optical tweezer trapping, the scattering force term can push the particle out of the trap, hence the trapping stability is determined by specific particle and beam parameters which render the scattering force negligible. In a single beam, the stability is limited by particle size and requires high numerical apertures of the focusing objective [37]. In addition, accurate modelling of beams generated by tightly focusing objectives require a more involved treatment using the angular spectrum representation [13]. However, in this thesis we will be primarily concerned with weakly-focused counter-propagating beam traps for which the Gaussian beam model is sufficient. Assuming that the counter-propagating beams are well spatially matched, the scattering force cancels out and the optical force near the focus becomes,

$$\langle \mathbf{F} \rangle_{\text{sw}} \approx \text{Re} [\alpha] \nabla \mathcal{E}(\mathbf{r})^2 \cos(Akz)^2 \quad (2.30)$$

with $A \approx 1 - 1/kz_R$, [82] and for which we can write down the optical potential,

$$U_{\text{sw}} = -\text{Re} [\alpha] \mathcal{E}(\mathbf{r})^2 \cos(Akz)^2 \quad (2.31)$$

which gives a periodic optical potential (see figure 4.4). Since the scattering force does not destabilise the trap, the potential in equation (2.31) allows

trapping of large particles near the limit of the dipole approximation validity. However, this is highly dependent on beam alignment.

2.6 Particle dynamics

The CM position of a particle trapped in the optical potential given in equation (2.31) behaves as a harmonic oscillator. For small displacement about the trap equilibrium position, the dynamics of displacement components x_i along orthogonal axes are independent, with mechanical frequencies $\Omega_i \approx \sqrt{-\partial_i^2 U_{\text{sw}}/m}$ evaluated about the trap centre for particle of mass m . The particle is always in contact with a thermal bath, such as residual gas in a vacuum chamber. The bath acts upon the particle with a stochastic stationary white noise force $F_{\text{th}}(t)$ and the corresponding mechanical damping γ , linked together by fluctuation-dissipation theorem,

$$\langle F_{\text{th}}(t)F_{\text{th}}(t') \rangle = 2m\gamma k_B T \delta(t - t') \quad (2.32)$$

where m , k_B and T are the particle mass, Boltzmann constant and the thermal equilibrium temperature respectively. In the case of residual gas, the force corresponds to recoil kicks due to random collisions with gas particles while γ gives rise to damping due to motion in a viscous fluid. The CM dynamics are then well described by the Langevin equation,

$$\ddot{x}_i(t) + \gamma \dot{x}_i(t) + \Omega_i^2 x_i(t) = \frac{1}{m} F_{\text{th}}(t) \quad (2.33)$$

along each direction. We will numerically simulate particle trajectories using (2.33) to test trap stability and the motion detection signal in our experimental configurations.

The fluctuating force in (2.33) can kick the particle out of the trap. The potential trap depth and the thermal equilibrium energy give us a measure of trap stability; a trap depth several factors larger than $k_B T$ is necessary for long-term trapping. The trap depth is proportional to the local intensity of the incident laser. In single beam traps, large trap depths are achieved with tightly

focused beams. In standing wave traps, larger beam powers can compensate for weak focusing, with the additional advantage of being able to trap larger particles, since the potential scales with $\alpha \propto r_p^3$. In the setup discussed in chapter 4, we were able to trap 300 nm silica particles in a standing wave trap with an estimated trap depth of $-U_{\text{sw}}/k_B \sim 10^5$ K.

In frequency domain, equation (2.33) takes the form,

$$\tilde{x}_i(\omega) = \tilde{\chi}_i(\omega)\tilde{F}_{\text{th}}(\omega) \quad (2.34)$$

where $\tilde{\chi}_i(\omega) = (m[\Omega_i^2 - \omega^2 - i\gamma\omega])^{-1}$ is the mechanical response function. We define the spectral density of $\tilde{x}_i(\omega)$,

$$S_{ii}(\omega) = \int \langle \tilde{x}_i(\omega)\tilde{x}_i^*(\omega') \rangle d\omega' \quad (2.35)$$

which quantifies how much a specified frequency ω contributes to the spread of \tilde{x}_i . Substituting (2.34), we can express the position spread in terms of the spectral density of the force noise fluctuations,

$$S_{ii}(\omega) = |\tilde{\chi}_i(\omega)|^2 S_F \quad (2.36)$$

with a flat force noise spectral density S_F , where we used the fact that the force F_{th} was assumed to be a stationary process, hence having uncorrelated spectral components $\langle \tilde{F}_{\text{th}}(\omega)\tilde{F}_{\text{th}}^*(\omega') \rangle = S_F\delta(\omega - \omega')$ [13]. Equation (2.36) quantifies the mechanical noise on the trapped particle in terms of the force fluctuations it receives from environmental sources.

For typical optical traps in an evacuated environment at pressures above about $10^{-7} - 10^{-6}$ mbar (see section 3.5.1) the force fluctuations are dominated by collisions with gas particles, and at thermal equilibrium we have,

$$S_F^{\text{gas}} = \frac{2}{\pi}mk_B T\gamma_{\text{gas}} \quad (2.37)$$

At pressures below 1 mbar, gas damping is proportional to the gas pressure [37], therefore reducing the pressure can minimise the amount of mechanical noise added by the gas. At low enough pressures, the gas contribution no

longer dominates and the mechanical noise is fundamentally dominated by *measurement backaction*¹ - recoil noise due to scattering of laser light. In this case the force fluctuations are in balance with radiation damping [87], with the equilibrium temperature proportional to the trapping light photon energy $\hbar\omega_0/k_B$. The force fluctuations of laser recoil can be understood to arise as a result of interference of the trapping laser light with local, zero-point or thermal, field fluctuations $\delta\mathbf{E}$ [59, 88]. The fluctuations in the fields and the resulting force can be captured within a classical model by employing a stochastic process description of the field and a macroscopic description of the surrounding matter [13]. The fluctuation-dissipation theorem for these field fluctuations at equilibrium with temperature T states that the spectral field correlations are proportional to the dissipation of the fields by a point current,

$$\langle \delta\tilde{E}_i(\mathbf{r}, \omega)\delta\tilde{E}_i^*(\mathbf{r}, \omega') \rangle = \frac{\hbar\omega^2}{2\pi c^2 \epsilon_0} \coth\left(\frac{\hbar\omega}{2k_B T}\right) \text{Im}[G_{ii}(\mathbf{r}, \mathbf{r}, \omega)] \delta(\omega - \omega') \quad (2.38)$$

which as discussed before depends on the environment. Modelling the fluctuations in this fashion was used to model surface-induced heating in levitated optomechanics [59, 60]. It is frequently stated in literature that mechanical noise due to measurement backaction is unavoidable, as the scattered light which carries information about particle position encoded in its phase necessarily leads to recoil. This is true in free-space and in most cases also near boundaries. However, in the next chapter we show that a highly reflective boundary with a suitable geometry in combination with a standing wave trapping configuration can lead to a significant reduction in the mechanical noise added by recoil, while the particle continues to scatter laser light.

¹Other noise sources also contribute and can dominate mechanical noise, such as laser intensity noise or laser phase noise in standing wave traps. However, these sources of noise can be mitigated by feedback cooling particle motion and by frequency stabilisation techniques, respectively. We discuss these in more detail in the next chapter.

Chapter 3

Backaction suppression in a structured environment

Precision in the continuous measurement of an optical sensor is fundamentally limited by photon recoil noise [1], with the fundamental limit given by the *standard quantum limit* [3, 7]. Attempting to resolve the position of the levitated particle further by increasing illuminating power, irrevocably increases momentum fluctuations received in the form of force fluctuations from the laser field [38]. Under optimal illuminating power, which yields the minimum achievable noise in a continuous position measurement, fluctuations in the signal due to *measurement imprecision* and *measurement backaction* contribute equally. One can always make a trade-off between imprecision and backaction by changing the illuminating power, but it is also possible by employing squeezed light [18], which allows suppression of laser recoil noise and measurements beyond what is achievable under the standard quantum limit [16, 56].

Trapping near surfaces affects heating of particle motion [58–60]. Apart from the surface material, the heating also strongly depends on the surface geometry [57]. In this chapter, we investigate how the presence of a large spherical mirror affects position detection of a trapped nanoparticle and

the corresponding mechanical noise from backaction. The spherical mirror geometry was previously found to strongly modify the local density of optical states at its centre [81] allowing for full suppression of spontaneous emission from an atom. There is current experimental interest in studying QED effects of the hemisphere using trapped ions [89]. In the context of levitated optomechanics, optimal position measurement of a particle trapped at the centre of a spherical mirror was recently analysed [84] and realised in experiment using a focusing lens and a plane mirror [90]. The authors show that the spherical mirror, under appropriate condition on its radius, can be used to realise an ideal reference field for self-homodyne detection and is able to reach the Heisenberg limit of detection by observation from only half of the solid angle. A similar setup was also recently proposed for the purpose of backaction suppression [91].

In the following sections, we explore the utility of the hemispherical geometry in concealing first-order position information in an experimentally controllable fashion. In contrast to the findings presented in the recent paper [91], we find that suppression of scattered power *does not* correspond to the suppression of backaction. Instead, we find that the linear position read-out becomes inaccessible in an interferometric measurement of the far-field scatter when the scattered power is *maximally enhanced* by the spherical mirror and only in a standing wave trapping potential. Using a stochastic electrodynamics description of the local zero-point field fluctuations, we then compute the local optical force fluctuations on a point dipole, accounting for the presence of the mirror. Under the same conditions which render the signal insensitive to first-order motion, the dominating term in the noise spectral density of the force fluctuations vanishes. While the hemispherical geometry facilitates suppression of field gradient fluctuations, a standing wave trapping configuration is necessary to suppress residual field amplitude fluctuations. We show that the results found satisfy the Heisenberg limit of position detection, and therefore constitute a trade-off between measurement imprecision and backaction without altering the illuminating laser power.

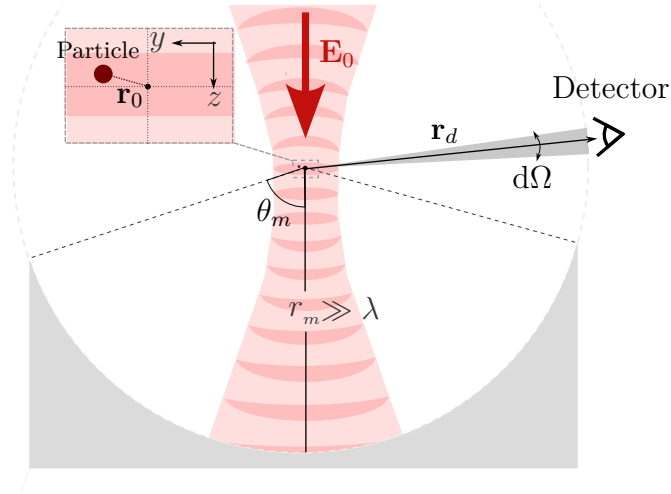


Figure 3.1: Spherical mirror trapping configuration. A laser beam polarised out of the page is focused close to the centre of the spherical mirror, such that the beam retroreflects from the mirror surface and generates a standing wave trap. A particle is trapped at the central maximum. The remaining available solid angle not covered by the spherical mirror is used for position detection on differential detectors each covering a solid angle $d\Omega$

3.1 Problem statement

We focus the study on two aspects of the position detection process in the subsequent sections:

- **measurement imprecision** which dictates the amount of particle position information gained from the detected scatter signal
- **measurement backaction** which quantifies the amount of mechanical noise imparted on the particle by the measuring field

We begin the analysis in this chapter by computing achievable measurement imprecision in an ideal position detection experiment of a particle trapped in a standing wave field in front of a spherical mirror. To do this, we follow the treatment presented in [92] based on the flow of Fisher information flux. We frame the discussion in terms of homodyne detection experiment of a particle trapped in a standing wave near the centre of a hemispherical mirror. The

setup which realises the optimal measurement scheme of the position detection experiment is depicted in figure 3.1. The particle motion is observed on an array of detectors in the far-field. Assuming that the detectors are shot-noise limited, it can be shown that this is an optimal way to localise the particle from far-field observation [82, 84, 93], as it allows one to localise the particle to the Heisenberg limit of detection. [3, 92, 94].

Throughout this analysis, we work in the quasistatic limit, ignoring any effects the motion has on the imprecision-backaction characteristics. Assuming that the mirror is not too large, this is considered permissible since the particle motion is significantly slower than time delay of the mirror-particle round trip. The considered particle is modelled as a point dipole (radius $r_p \ll \lambda$) with isotropic polarisability α . Due to its interaction with the laser light, the dynamics of the particle are described by the Langevin equation $\ddot{x}_i(t) + \gamma \dot{x}_i(t) + \Omega_i^2 x_i(t) = \delta F_i/m$, where γ and Ω_i are the mechanical damping and the trap frequency, respectively. The term δF_i is a component of a stochastic force $\delta \mathbf{F}$ which acts on the particle due to the thermal bath and laser recoil. We assume that we can ignore the contribution of residual gas and the force fluctuations are dominated by the contribution from laser recoil. The particle is located at $\mathbf{r}_0 = \mathbf{r}_t + \delta \mathbf{r}$, where \mathbf{r}_t is the equilibrium position of the trap centre and $|\delta \mathbf{r}| \ll \lambda$ is the displacement due to the motion about the trap centre. For the majority of this chapter, we take \mathbf{r}_t to coincide with the hemisphere centre, and the centre of the coordinate system. Later, we consider the situation of the trap centre displaced along mirror axis.

The beam is incident upon the mirror surface and forms a standing wave trap. We assume that the beam parameters are selected such that the beam is retroreflected and an intensity maximum appears at the mirror centre (see section 4.1 for details). The particle is trapped in the central maximum of the standing wave. Assuming that the beam is weakly-focused and the central maximum is sufficiently close to the beam waist, the standing wave field $\mathbf{E}_0(\mathbf{r}, t) = \text{Re} [\mathbf{E}_0(\mathbf{r}) e^{-i\omega_0 t}]$ resembles a field of two counter-propagating plane waves, [82]

$$\mathbf{E}_0(\mathbf{r}) = E_0 \cos(Ak_0 z) \hat{\mathbf{x}} \tag{3.1}$$

In equation (3.1), $k_0 = 2\pi/\lambda$ is the free-space wavenumber of the laser beam and the Gouy factor A arises due to the spatial confinement of the field and increases the effective wavelength, depending on the degree of focusing.

In the subsequent section, we extend the analysis to measurement backaction by employing a stochastic electrodynamics description of the local field fluctuations, [88, 93, 95, 96] and computing the spectral noise density of the recoil force, in free space and in a standing wave formed by reflection from a spherical mirror. For a particle trapped in free space, we recover known expressions for laser recoil noise, [38, 82] showing how the different contributions arise as a result of the trapping field coupling to the background field gradient fluctuations, and trapping field gradient coupling to the background field at the same frequency as the trapping light. In the final section, we discuss the result with its implications and analyse the residual noise in a possible experimental demonstration.

3.2 Measurement imprecision

To realise the ideal measurement scheme, we envision measuring the particle position \mathbf{r}_0 by observing the field which it scatters using an array of detectors each spanning a solid angle $d\Omega$, over the total solid angle not covered by the spherical mirror, as shown in figure 3.1. In front of a spherical mirror, particle position is encoded in the intensity modulation of the sum of the dipole emission field and its reflection. The reflection of the scatter from the mirror serves as a moving reference field [84]. Using equation (2.20), we can express the far-field of the dipole emission in front of a reflecting spherical mirror with reflection coefficient $|\rho| = 1$ driven by (3.1) as,

$$\mathbf{E}_{\text{tot}}(\mathbf{r}_d) = \mathbf{E}_s(\mathbf{r}_d) \cos(Ak_0 z_0) (e^{-ik_0 \hat{\mathbf{r}} \cdot \mathbf{r}_0} - \rho e^{ik_0 (\hat{\mathbf{r}} \cdot \mathbf{r}_0 + 2rm)}) \quad (3.2)$$

where \mathbf{E}_s is the free-space dipole emission field. The corresponding differential power $dP = \langle \mathbf{S} \rangle \cdot \hat{\mathbf{r}} dA$ incident upon a detector spanning a solid angle $d\Omega$ with

Poynting vector $\langle \mathbf{S} \rangle = (1/2)(\mathbf{E}_{\text{tot}} \times \mathbf{H}_{\text{tot}}^*)$ is found to be,¹

$$\begin{aligned} dP &= 2 \cos^2(Ak_0 z_0)(1 - \text{Re}[\rho e^{2ik_0 r_m}]) dP_0 \\ dP_0 &= P_0 \rho_x(\theta, \phi) d\Omega \end{aligned} \quad (3.3)$$

where P_0 is the free-space scattered power and ρ_x is the radiation pattern of an $\hat{\mathbf{x}}$ polarised dipole. Observation of (3.3) realises the self-homodyne detection scheme of [84] for an appropriate choice of mirror radius r_m .

We can formally quantify minimum measurement imprecision in far-field, shot-noise-limited detection of particle position using the recently developed formalism of Fisher information (FI) flow [92], which places a lower bound on the variance in the measured quantity. Specifically, the formalism introduces a local quantity of Fisher information flow, akin to the Poynting vector which describes the flow of electromagnetic energy. In the time average, the reciprocal of this quantity then places a bound on the average rate at which the variance of a variable can be reduced in a 1 Hz bandwidth of shot-noise-limited measurement. The treatment is equivalent to treating the problem of interference experiment depicted in figure 3.1 with a strong, mode-matching reference field. In a 1 Hz bandwidth we have,

$$\text{Var}(x_i) \geq \left(2\pi \int \mathbf{S}_{\text{FI}}^i \cdot \hat{\mathbf{r}} dA \right)^{-1} 2\pi [\text{Hz}] \quad (3.4)$$

where, [92]

$$\mathbf{S}_{\text{FI}}^i = \frac{2}{\hbar\omega_0} \text{Re}[\partial_i \mathbf{E}_{\text{tot}} \times \partial_i \mathbf{H}_{\text{tot}}^*] \quad (3.5)$$

defines the time-averaged FI flux with $\partial_i \equiv \partial/\partial x_i$, and the quantity in parentheses in equation (3.4) corresponds to the flat spectral density of minimum imprecision noise,

$$S_{\text{imp}}^i = \left(2\pi \int \mathbf{S}_{\text{FI}}^i \cdot \hat{\mathbf{r}} dA \right)^{-1} \quad (3.6)$$

¹ dP_0 represents the differential power radiated by an $\hat{\mathbf{x}}$ oriented dipole into the solid angle element $d\Omega$.

in the measurement of x_i . To obtain an optimal estimate of the particle's position for general mirror spanning angle θ_m (see figure 3.1), we need to find \mathbf{S}_{FI}^i in each angular domain over the element $dA = r_d^2 d\Omega$, as depicted in figure 3.2. To begin with, we consider domain (b) which corresponds to free-space dipole emission. In a standing wave, the electric field of emission in (b) is equal to, [82]

$$\mathbf{E}_s(\mathbf{r}_d, \mathbf{r}_0) = \mathbf{E}_s(\mathbf{r}_d) \cos(Ak_0 z_0) e^{-ik_0 \hat{\mathbf{r}} \cdot \mathbf{r}_0} \quad (3.7)$$

We insert (3.7) into (3.5), using the fact that in the far-field the fields are transverse with the relationship $\mathbf{H}_{\text{tot}} = -\epsilon_0 c \mathbf{E}_{\text{tot}} \times \hat{\mathbf{r}}$ and evaluating the derivatives about $\mathbf{r}_0 = (0, 0, 0)$,

$$S_{\text{imp}}^{i(b)} = \left(\frac{4\pi k_0 \epsilon_0}{\hbar} \int_b \hat{r}_i^2 |\mathbf{E}_s(\mathbf{r}_d)|^2 r_d^2 d\Omega \right)^{-1} \quad (3.8)$$

Using $\mathbf{E}_s(\mathbf{r}_d) = (k_0^2/\epsilon_0) \overline{\overline{\mathbf{G}}_{\text{ff}}}(\mathbf{r}_d, \mathbf{r}_0) \cdot \mathbf{p}$ and the definition of the free-space far-field dyadic Green's function, for $\hat{\mathbf{x}}$ polarised dipole we find,

$$S_{\text{imp}}^{i(b)} = \left(\frac{8\pi k_0}{\hbar c} \int_b \hat{r}_i^2 dP_0 \right)^{-1} \quad (3.9)$$

where we defined the free-space average scattered power $P_0 = k_0^4 c |\mathbf{p}|^2 / (12\pi\epsilon_0)$ and again used $dP_0 = P_0 \rho_x(\theta, \phi) d\Omega$. When integrated over the full solid angle, (3.9) reproduces the imprecision noise for a standing-wave field in the absence of the mirror, [82, 97]

$$\begin{aligned} (S_{\text{imp}}^x)_{\text{free}} &= \left(\frac{8\pi k_0}{\hbar c} \int_{4\pi} \sin^2 \theta \cos^2 \phi dP_0 \right)^{-1} = 5 \frac{\hbar c}{8\pi k_0} \frac{1}{P_0} \\ (S_{\text{imp}}^y)_{\text{free}} &= \left(\frac{8\pi k_0}{\hbar c} \int_{4\pi} \sin^2 \theta \sin^2 \phi dP_0 \right)^{-1} = \frac{5}{2} \frac{\hbar c}{8\pi k_0} \frac{1}{P_0} \\ (S_{\text{imp}}^z)_{\text{free}} &= \left(\frac{8\pi k_0}{\hbar c} \int_{4\pi} \cos^2 \theta dP_0 \right)^{-1} = \frac{5}{2} \frac{\hbar c}{8\pi k_0} \frac{1}{P_0} \end{aligned} \quad (3.10)$$

Note that the imprecision noise in the measurement of z_0 in (3.10) does not contain the factor A (see section 3.1). Unlike in a single beam setup [82], at

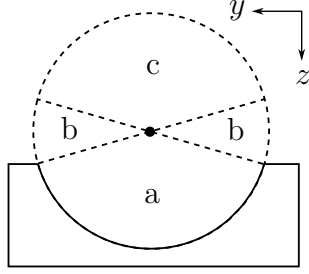


Figure 3.2: Diagram denoting different measurement domains. Since we assumed that $|\rho| = 1$, no field gets transmitted and dipole emission is not accessible for measurement within domain (a). Because dipole scatter is retroreflected by the mirror surface, the mirror only affects the detected emission in domain (c). In (c), dipole emission is given by equation (3.2) and provides a self-homodyne measurement. Domain (b) corresponds to free-space dipole emission.

a maximum of a standing wave, the local phase does not carry linear position information. We follow the same steps to find the imprecision noise in domain (c) using the field in (3.2) and find,

$$\begin{aligned}
 S_{\text{imp}}^i{}^{(c)} &= \left(\frac{8\pi k_0 \epsilon_0}{\hbar} \left(1 + \text{Re} \left[\rho e^{2ik_0 r_m} \right] \right) \int_c \hat{r}_i^2 |\mathbf{E}_s(\mathbf{r}_d)|^2 dA \right)^{-1} \\
 &= \left(\frac{16\pi k_0}{\hbar c} \left(1 + \text{Re} \left[\rho e^{2ik_0 r_m} \right] \right) \int_c \hat{r}_i^2 dP_0 \right)^{-1}
 \end{aligned} \tag{3.11}$$

Finally, combining measurement noise across angular domains (as specified in figure 3.2), we arrive at the total measurement imprecision,

$$S_{\text{imp}}^i = S_{\text{imp}}^i{}^{(b)} + S_{\text{imp}}^i{}^{(c)} \tag{3.12}$$

The first term in (3.12) represents noise in domain (b) for a measurement made under the optimal free-space scheme of [82], while the second term corresponds to domain (c) as described above. We now proceed to analyse the result (3.12).

3.2.1 Discussion

Firstly, we focus on the limit of a full hemisphere ($\theta_m = \pi/2$). In this case, the domain of integration (b) in (3.12) vanishes, and only the second term contributes to imprecision and we find,

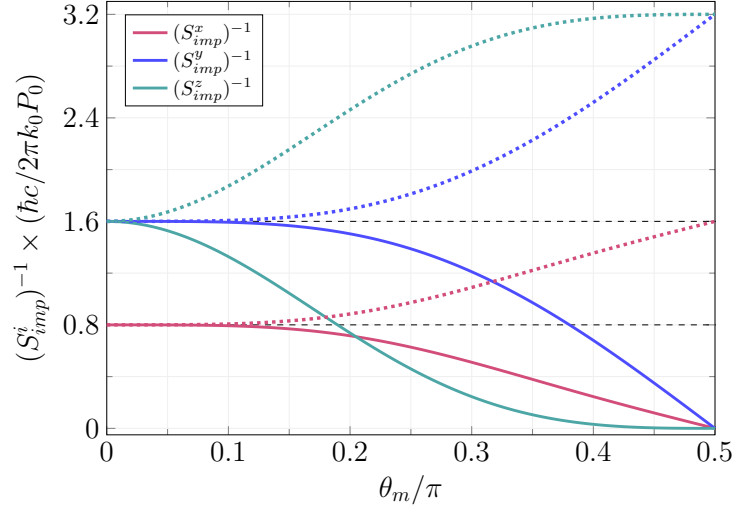


Figure 3.3: Measurement imprecision S_{imp}^i against spherical mirror half angle θ_m found by solving (3.12). Explicit solutions for the curves are given in B.2. Filled lines indicate variation at $k_0 r_m = n\pi$ and dotted lines at $k_0 r_m = n\pi \pm \pi/2$. Dashed lines indicate free-space levels in a standing wave (at $\theta_m = 0$). At $k_0 r_m = n\pi \pm \pi/4$ imprecision does not change from free-space levels with varying θ_m .

$$S_{\text{imp}}^i = \frac{5}{2} \frac{\hbar c}{8\pi k_0} \frac{1}{P_0} (1 + \delta_{ix}\delta_{xi}) \left(1 + \text{Re}[\rho e^{2ik_0 r_m}]\right)^{-1}. \quad (3.13)$$

In general, $\text{Re}[\rho] < 1$ makes the effect of the mirror on the imprecision less significant. We will focus on the discussion of (3.12) with $\rho = -1$ (perfect reflection) at three conditions on the mirror radius,

$$k_0 r_m = \begin{cases} n\pi \pm \pi/4 & \text{self-homodyne (l)} \\ n\pi \pm \pi/2 & \text{scattered power suppression (s)} \\ n\pi & \text{scattered power enhancement (e)} \end{cases} \quad (3.14)$$

for integer n . The optimal condition on mirror radius in the self-homodyne detection scheme is (l) as noted in [84]. At condition (l) we retain twice the free-space amount of linear information in any angular element in domain (c), and for which (3.12) gives the same total imprecision as is achievable in a free-space standing wave. For condition (s), equation (3.12) suggests that

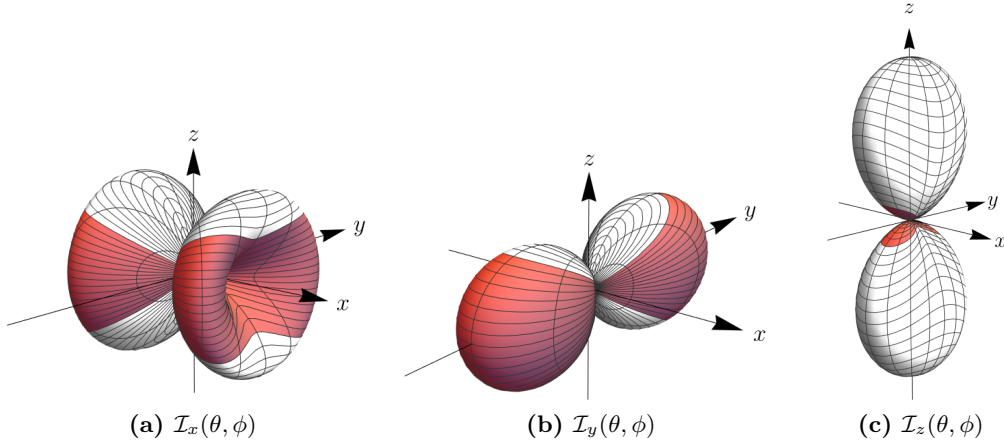


Figure 3.4: Angular spread of position information here normalised to the total free-space imprecision $\mathcal{I}_i(\theta, \phi) = (S_{\text{imp}}^i)_{\text{free}}/dS_{\text{imp}}^i(\theta, \phi)$ from equation (3.10). The mirror is perfectly reflecting ($\rho = -1$), has its axis of symmetry along $\hat{\mathbf{z}}$ as in figure 3.1 and was chosen to have $\theta_m = \pi/3$. The white region corresponds to domain (c) in 3.2, in which the scatter is affected by the mirror. The information in the white region of the top half-space is never accessible because this portion of the solid angle is covered by the mirror. At $k_0 r_m = n\pi$ the position information is inaccessible in the white region of both half-spaces. The colored region corresponds to free-space information.

half the total free-space imprecision is achievable. However, this condition also corresponds to the full suppression of scattered power, meaning that such reduction is likely not achievable or desirable in practice as the signal would be vanishingly small.

We now turn to the discussion of measurement noise at condition (e). At (e), the total scattered power is enhanced by a factor of 2 relative to free-space, but measurement noise in (3.12) diverges, suggesting that the signal contains no linear position information. Indeed, no mode-matching reference can be added to (3.2) to obtain a linear position signal since at (e), the dipole emission is equal to,

$$\mathbf{E}_{\text{tot}}(\mathbf{r}_d) \approx 2\mathbf{E}_s(\mathbf{r}_d) \quad (3.15)$$

to first order in \mathbf{r}_0 ; the free-space particle radiation away from the mirror is in phase with its image, making it impossible to distinguish between them to

first order.

Lastly, we discuss the variation of (3.12) with mirror polar angle θ_m . Figure 3.3 shows that at condition (e), $(S_{zz}^{\text{imp}})^{-1}$ decreases faster with θ_m than $(S_{xx}^{\text{imp}})^{-1}$ and $(S_{yy}^{\text{imp}})^{-1}$.

We can gain more insight into this result by analysing the angular distribution of radiated position information, quantified by the normalised integrand of equation (3.12). The resulting plots are shown in figure 3.4 for a mirror with an illustrative spanning angle of $\theta_m = \pi/3$. Firstly, we note that the shapes of \mathcal{I}_i are unchanged by the mirror compared with the spread of information in free space [82],² because the radiation pattern for a particle located near the mirror centre is unchanged to linear order. However, the information content changes discontinuously between the angular domain affected by the mirror (domain (a) and (c) in figure 3.2) and the unaffected domain (domain (b) in figure 3.2). At $k_0 r_m = n\pi$ information in the white regions of figure 3.4 is inaccessible. Because of the mirror's orientation, the information is symmetrically affected about the $\hat{\mathbf{z}}$ axis. This causes $(S_{zz}^{\text{imp}})^{-1}$ to decrease faster with θ_m , since \mathcal{I}_z is more tightly concentrated about the $\hat{\mathbf{z}}$ axis. In the next section we explore the same situation from the standpoint of measurement backaction in attempt to gain further insight in the results found for the solutions to (3.12).

²Note that \mathcal{I}_z appears symmetric unlike in [82] because in a standing wave the A focusing factor does not contribute to the imprecision

3.3 Measurement backaction

In this section, we quantify the mechanical noise on a trapped particle, by evaluating the spectral noise density of the optical force fluctuations which acts upon it, due to the laser field and background field fluctuations.

The particle interacts with the laser field and a fluctuating background field,

$$\mathbf{E}(\mathbf{r}_0, t) = \mathbf{E}_0(\mathbf{r}_0, t) + \delta\mathbf{E}(\mathbf{r}_0, t). \quad (3.16)$$

In (3.16) $\delta\mathbf{E}$ is a statistically stationary process with zero average [88], and \mathbf{E}_0 is the sum of the laser field and its reflection from the environment. In general, the particle also interacts with reflections of its own scatter, which lead to an infinite series of additional terms in (3.16) scaling in powers of $k^3\alpha$. Since $k^3\alpha \sim (r_p/\lambda)^3$ each of these terms contributes increasingly less. Since we are interested in computing the dominating contribution to laser recoil noise, we choose to truncate the series in α to zeroth order.³ Treating the particle as a point oscillating dipole located at \mathbf{r}_0 , the field in (3.16) induces a dipole moment \mathbf{p} which gives rise to a force, [79]

$$\mathbf{F}(\mathbf{r}_0, t) = \sum_i p_i(t) \nabla E_i(\mathbf{r}_0, t) + \frac{d}{dt} \left[\mathbf{p}(\mathbf{r}_0, t) \times \mathbf{B}(\mathbf{r}_0, t) \right]. \quad (3.17)$$

which, when written in the frequency domain becomes,

$$\tilde{\mathbf{F}}(\mathbf{r}_0, \omega) = \sum_i \left\{ \tilde{p}_i * \nabla \tilde{E}_i \right\}(\mathbf{r}_0, \omega) - i\omega \sum_{ijk} \epsilon_{ijk} \left\{ \tilde{p}_i * \tilde{B}_j \hat{\mathbf{x}}_k \right\}(\mathbf{r}_0, \omega) \quad (3.18)$$

The quantities in (3.18) with a tilde denote the respective Fourier transforms (defined by (A.1)),

$$\begin{aligned} \tilde{\mathbf{p}}(\mathbf{r}_0, \omega) &= \tilde{\alpha}(\omega) \tilde{\mathbf{E}}(\mathbf{r}_0, \omega) \\ \tilde{\mathbf{E}}(\mathbf{r}_0, \omega) &= \tilde{\mathbf{E}}_0(\mathbf{r}_0, \omega) + \delta\tilde{\mathbf{E}}(\mathbf{r}_0, \omega). \end{aligned} \quad (3.19)$$

³The first order of these terms is imaginary, and it is usually absorbed into the definition of free-space polarisability [13, 98]. Because of the omission of it made here, the average scattering force will be missing from (3.20). It is equivalent to ignoring the influence of the dipole emission on the force, which has a significantly smaller contribution than the incident field. Therefore, ignoring it here does not influence the subsequent calculation of the force noise spectral density.

and the symbol $*$ denotes a convolution for vectors (as defined in (A.3)). Absence of the internal dipole moment fluctuations in $\tilde{\mathbf{p}}$ of (3.19) indicates that we have also ignored the internal heating of the particle. We will continue to make this approximation in the calculation of the force noise by assuming real $\tilde{\alpha}$.

Note that the second force term in (3.18) is proportional to the frequency ω . In order to evaluate the mechanical noise on the trapped particle, we wish to evaluate the force at trap frequency. For typical optical wavelengths and optical powers, the trap frequency is significantly smaller than the optical frequency. For example, a fused silica nanoparticle trapped in a single 250 mW laser beam of wavelength $\lambda = 1550$ nm focused with a NA = 0.5 lens generates a trap with frequency of about 100 kHz orthogonal to beam propagation. Therefore, we can assume that $\omega \ll \omega_0$. In this regime, the contribution of the second term is negligible. More specifically, the cross terms between the first and second force term in the spectral density of the force have a contribution smaller than the largest terms arising from only the first term by a factor of (ω/ω_0) . Likewise, terms arising from the second term alone are smaller by a factor of $(\omega/\omega_0)^2$. We therefore neglect the second force term and proceed with the simplified expression,

$$\begin{aligned}\tilde{\mathbf{F}}(\mathbf{r}_0, \omega) &= \sum_i \left\{ \tilde{p}_i * \nabla \tilde{E}_i \right\}(\mathbf{r}_0, \omega) \\ &= \tilde{\mathbf{F}}_0(\mathbf{r}_0, \omega) + \delta\tilde{\mathbf{F}}(\mathbf{r}_0, \omega)\end{aligned}\tag{3.20}$$

In equation (3.20) we chose $\tilde{\mathbf{F}}$ to represent the deterministic force and $\delta\tilde{\mathbf{F}}$ to represent force fluctuations - that is, any terms containing fluctuations in the fields up to linear order,

$$\delta\tilde{\mathbf{F}}(\mathbf{r}_0, \omega) = \left\{ \tilde{\alpha} \tilde{E}_0 * \nabla \delta\tilde{E} \right\}(\mathbf{r}_0, \omega) + \left\{ \tilde{\alpha} \delta\tilde{E} * \nabla \tilde{E}_0 \right\}(\mathbf{r}_0, \omega),\tag{3.21}$$

where we assumed that \mathbf{E}_0 is $\hat{\mathbf{x}}$ polarised and dropped the subscript ‘ x ’ from the field components δE_x and E_{0x} for clarity. In a regime dominated by field fluctuations, $\delta\tilde{\mathbf{F}}$ acts as a noisy driving force for the harmonic dynamics generated by \mathbf{F}_0 ,

$$\ddot{x}_i(t) + \gamma \dot{x}_i(t) + \Omega_i^2 x_i(t) = \frac{1}{m} \delta F_i(t)\tag{3.22}$$

where γ is the mechanical damping and Ω_i is the trap frequency along x_i . In the next sections we evaluate (3.21) for a monochromatic driving field. As a first example consider the case of a plane-wave incident upon the particle in free-space and recover known results for the force noise. We then use the developed formalism to treat the problem of force noise on a particle trapped in the setup of figure 3.1.

3.3.1 Single beam force noise in free-space

In this section we compute the spectral density of the force noise $\delta\mathbf{F}$ in (3.21) at the location of the particle \mathbf{r}_0 evaluated at the trap frequency. Assuming force fluctuations $\delta\mathbf{F}$ is a wide-sense stationary process, we find the corresponding spectral density using,⁴ [80]

$$\begin{aligned} S_{ij}^F(\omega) &= \frac{1}{2\pi} \int_{\mathbb{R}} \langle \delta F_i(\mathbf{r}_0, t) \delta F_j(\mathbf{r}_0, t + \tau) \rangle e^{i\omega\tau} d\tau \\ &= \int_{\mathbb{R}} \langle \delta \tilde{F}_i(\mathbf{r}_0, \omega) \delta \tilde{F}_j^*(\mathbf{r}_0, \omega') \rangle d\omega' \end{aligned} \quad (3.23)$$

driven by a plane-wave monochromatic field, $\mathbf{E}_0(\mathbf{r}, t) = \text{Re} [\tilde{E}_0(\mathbf{r}) e^{-i\omega_0 t}] \hat{\mathbf{x}}$. Firstly, evaluating the Fourier transform of \mathbf{E}_0 we find,

$$\tilde{\mathbf{E}}_0(\mathbf{r}, \omega) = \frac{1}{2} \left(\tilde{E}_0(\mathbf{r}) \delta(\omega - \omega_0) + \tilde{E}_0^*(\mathbf{r}) \delta(\omega + \omega_0) \right) \hat{\mathbf{x}} \quad (3.24)$$

Substituting (3.24) into (3.21) and evaluating the convolutions leads to,

$$\begin{aligned} \delta \tilde{\mathbf{F}}(\mathbf{r}_0, \omega) &= \frac{1}{2} \tilde{\alpha} \left(\tilde{E}_0(\mathbf{r}_0) \nabla \delta \tilde{E}(\mathbf{r}_0, \omega - \omega_0) + \tilde{E}_0^*(\mathbf{r}_0) \nabla \delta \tilde{E}(\mathbf{r}_0, \omega + \omega_0) \right) \\ &\quad + \delta \tilde{E}(\mathbf{r}_0, \omega - \omega_0) \nabla \tilde{E}_0(\mathbf{r}_0) + \delta \tilde{E}(\mathbf{r}_0, \omega + \omega_0) \nabla \tilde{E}_0^*(\mathbf{r}_0) \end{aligned} \quad (3.25)$$

⁴ $\langle \cdot \rangle$ denotes an ensemble average over realisations of the fluctuations, or a time-average of a sufficiently long trajectory of a single realisation.

where we assumed that the polarisability $\tilde{\alpha}$ is real⁵ and ignored its dispersion⁶, introducing $\tilde{\alpha} = \tilde{\alpha}(\omega_0)$. Before we write down the correlation functions, it is convenient at this point to rewrite the spectral density in (3.23) in tensor form,

$$\overline{\overline{\mathbf{S}}}_F(\omega) = \int_{\mathbb{R}} \left\langle \delta \tilde{\mathbf{F}}(\mathbf{r}_0, \omega) \delta \tilde{\mathbf{F}}^*(\mathbf{r}'_0, \omega') \right\rangle d\omega' \Big|_{\mathbf{r}_0=\mathbf{r}'_0}, \quad (3.26)$$

where any direct product of two vectors throughout the rest of this chapter denotes the tensor product. We now proceed to substitute (3.25) into (3.26) and apply the fluctuation-dissipation theorem of the $\hat{\mathbf{x}}$ component of the background field in thermal equilibrium with the environment at temperature T , [13, 57, 88]

$$\left\langle \delta \tilde{E}(\mathbf{r}, \omega) \delta \tilde{E}^*(\mathbf{r}', \omega') \right\rangle = \frac{\hbar \omega^2}{2\pi c^2 \epsilon_0} \coth \left(\frac{\hbar \omega}{2k_B T} \right) \text{Im} [G_{xx}(\mathbf{r}, \mathbf{r}', \omega)] \delta(\omega - \omega'), \quad (3.27)$$

where G_{xx} is an element of the Green's tensor $\overline{\overline{\mathbf{G}}}$ of the system, corresponding to the $\hat{\mathbf{x}}$ field component of the dipole emission of an $\hat{\mathbf{x}}$ polarised point dipole. In the *zero-temperature limit* ($\hbar\omega_0 \gg k_B T$), the quantity $\coth(\hbar|\omega_0|/2k_B T) \approx 1$ and $\coth(-\hbar|\omega_0|/2k_B T) \approx -1$, therefore positive and negative frequencies around ω_0 contribute equally with opposite signs. In this limit, substituting (3.25) into (3.26) with the use of (3.27), we finally arrive at an expression for the spectral density of force fluctuations,

$$\begin{aligned} \overline{\overline{\mathbf{S}}}_F(\omega) = & \frac{\hbar \tilde{\alpha}^2}{4\pi c^2 \epsilon_0} \sum_{\pm} (\omega \pm \omega_0)^2 \left[\tilde{E}_0^*(\mathbf{r}_0) \tilde{E}_0(\mathbf{r}'_0) \nabla \nabla' + \nabla \tilde{E}_0^*(\mathbf{r}_0) \nabla' \tilde{E}_0(\mathbf{r}'_0) \right. \\ & \left. + \tilde{E}_0^*(\mathbf{r}_0) \nabla' \tilde{E}_0(\mathbf{r}'_0) \nabla + \tilde{E}_0(\mathbf{r}'_0) \nabla \tilde{E}_0^*(\mathbf{r}_0) \nabla' \right] \text{Im} [G_{xx}(\mathbf{r}_0, \mathbf{r}'_0, |\omega \pm \omega_0|)]_{\mathbf{r}_0=\mathbf{r}'_0} \end{aligned} \quad (3.28)$$

⁵Measurement of the imaginary part of the polarisability of nanospheres in vacuum presents an ongoing experimental challenge [99]. However, $\text{Im}[\alpha]$ can be estimated using the bulk properties of the material [46, 59]. Based on the data reported in [46, 99] for silica at $\lambda = 1550$ nm, we can deduce that the contribution of $\text{Im}[\alpha(\omega_0)]$ to the noise spectral density is relatively small with $\text{Im}[\alpha]/\text{Re}[\alpha] \sim 10^{-8}$. We therefore choose to neglect the influence of $\text{Im}[\alpha(\omega_0)]$, and proceed with a purely real polarisability.

⁶To obtain the final expression we take the limit $|\omega \pm \omega_0| \approx \omega_0$. Hence, under our approximations, ignoring dispersion of polarisability at this point makes no difference in the final expression.

where the sum runs over the top and bottom sign of \pm and we used the fact that $\text{Im}[G_{xx}]$ is an odd function of ω . We simplify the expression further with $|\omega \pm \omega_0| \approx \omega_0$, which yields the final expression,

$$\begin{aligned} \bar{\bar{\mathbf{S}}}_F(\omega) = & \frac{\hbar\omega_0^2}{4\pi c^2 \epsilon_0} \tilde{\alpha}^2 \left[\tilde{E}_0^*(\mathbf{r}_0) \tilde{E}_0(\mathbf{r}'_0) \nabla \nabla' + \nabla \tilde{E}_0^*(\mathbf{r}_0) \nabla' \tilde{E}_0(\mathbf{r}'_0) \right. \\ & \left. + \tilde{E}_0^*(\mathbf{r}_0) \nabla' \tilde{E}_0(\mathbf{r}'_0) \nabla + \tilde{E}_0(\mathbf{r}'_0) \nabla \tilde{E}_0^*(\mathbf{r}_0) \nabla' \right] \text{Im}[G_{xx}(\mathbf{r}_0, \mathbf{r}'_0, \omega)]_{\mathbf{r}_0=\mathbf{r}'_0} \end{aligned} \quad (3.29)$$

We therefore find that the spectral density of the noise within our approximations depends only on the frequency of the illuminating laser. In the above we used the fact that spectral components of the force fluctuations at different frequencies do not correlate.

We can physically interpret the three terms in (3.29) in the following way: the second term represents the fluctuations of the scattering force, which depends on the spectral correlation of the field fluctuations. It is present only for force fluctuations along the direction of the phase gradient of the driving laser field. The first term depends on the correlation of the field gradient fluctuations, hence we can physically interpret it with the gradient force fluctuations. The remaining terms depend on correlations of the field and its gradient, which can give rise to cross-correlations of different force components. Within our approximations, our expression agrees with [59] for a model of a particle trapped in front of a flat plane, in the framework of macroscopic QED [60, 78]. In that context, the dominant contribution to noise arise from the driven-Casimir-Polder interaction term in the Hamiltonian of the trapped particle dynamics. This term is a result of interference of the classical driving field with medium-assisted vacuum fields.

We now apply (3.29) to the case of a particle illuminated by a focused laser field (propagating along $\hat{\mathbf{z}}$ and polarised along $\hat{\mathbf{x}}$) in free-space. Assuming that the particle is located close to the focus of the laser ($|\mathbf{r}_0| \ll \lambda$), we can approximate the spatial complex amplitude which describes the laser with $\tilde{E}_0(\mathbf{r}) = E_0 e^{iAk_0 z}$, [82] as considered in section 3.2 in the free-space calculation of measurement imprecision. In free-space, where the environment

is characterised by the free-space Green's tensor, the imaginary part of the Green's tensor component and its derivatives can be evaluated by taking $|\mathbf{r}_0 - \mathbf{r}'_0| \rightarrow 0$, and it can be shown that, (see appendix section B.1)

$$\begin{aligned} \text{Im}[G_{xx}(\mathbf{r}_0, \mathbf{r}_0, \omega)] &= \frac{1}{6\pi} \left(\frac{\omega}{c}\right) \\ \nabla \text{Im}[G_{xx}(\mathbf{r}_0, \mathbf{r}'_0, \omega)]_{\mathbf{r}_0=\mathbf{r}'_0} &= \mathbf{0} \\ \nabla \nabla' \text{Im}[G_{xx}(\mathbf{r}_0, \mathbf{r}_0, \omega)]_{\mathbf{r}_0=\mathbf{r}'_0} &= \frac{1}{30\pi} (2\bar{\bar{\mathbf{I}}} - \hat{\mathbf{x}}\hat{\mathbf{x}}) \left(\frac{\omega}{c}\right)^3 \end{aligned} \quad (3.30)$$

where $\bar{\bar{\mathbf{I}}}$ is the unit dyad. Therefore, in free space the terms in (3.29) which depend on the first derivative of $\text{Im}[G_{xx}]$ vanish. Defining the free space scattered power driven at frequency ω_0 , [13]

$$P_0 = \frac{E_0^2 k_0^4 c}{12\pi\epsilon_0} \tilde{\alpha}(\omega_0)^2. \quad (3.31)$$

and using the evaluated derivatives leads to the final expression,

$$\bar{\bar{\mathbf{S}}}_F(\omega) = \frac{\hbar k_0}{2\pi c} P_0 \left(\frac{1}{5} (2\bar{\bar{\mathbf{I}}} - \hat{\mathbf{x}}\hat{\mathbf{x}}) + A^2 \hat{\mathbf{z}}\hat{\mathbf{z}} \right) \quad (3.32)$$

which is in agreement with the known free-space results, [82, 97]

$$\begin{aligned} S_{xx}^F(\omega) &= \frac{1}{5} \frac{\hbar k_0}{2\pi c} P_0, \\ S_{yy}^F(\omega) &= \frac{2}{5} \frac{\hbar k_0}{2\pi c} P_0, \\ S_{zz}^F(\omega) &= \left(\frac{2}{5} + A^2 \right) \frac{\hbar k_0}{2\pi c} P_0, \end{aligned} \quad (3.33)$$

and $S_{ij}^F(\omega) = 0$ for $i \neq j$. In the next section, we turn to the problem of computing the force noise for a particle trapped at and near the centre of a spherical mirror.

3.3.2 Force noise in front of a spherical mirror

In this section, we consider the backaction noise for a particle trapped near the centre of a spherical mirror as depicted in figure 3.1. Firstly, we note

that dipole emission reflected back by the boundary acts as an extra field which further interacts with the particle. In some situations, this field can significantly alter the trapping potential, and in literature is known as self-induced backaction (SIBA) (see section 4.9.1) However, based on the analysis shown in later chapters, SIBA can always be made to have a negligible influence on the trap equilibrium position, by appropriate choice of beam and particle parameters. We therefore choose to ignore its influence throughout this section.

Assuming that the beam is retroreflecting from the mirror surface with a field maximum at the centre, the total driving field near the focus is a sum of two counter-propagating beams, such that the complex amplitude of the total driving field near the mirror centre where the particle is located is simply given by $\tilde{E}_0(\mathbf{r}) = E_0 \cos(Ak_0 z)$. When this expression for the incident field is substituted into equation (3.29) we get,

$$\begin{aligned} \bar{\bar{\mathbf{S}}}_F(\omega) = \frac{\hbar k_0}{2\pi c} P_0 \frac{6\pi}{k_0^3} \left[\right. \\ \left. \begin{aligned} & ((Ak_0)^2 \sin(Ak_0 z_0)^2 \hat{\mathbf{z}}\hat{\mathbf{z}} + \cos(Ak_0 z_0)^2 \nabla \nabla') \text{Im} [G_{xx}(\mathbf{r}_0, \mathbf{r}'_0, \omega_0)] \\ & - \frac{Ak_0}{2} \sin(2Ak_0 z_0) \text{Im} [\nabla G_{xx}(\mathbf{r}_0, \mathbf{r}'_0, \omega_0) \hat{\mathbf{z}} + \hat{\mathbf{z}} \nabla' G_{xx}(\mathbf{r}_0, \mathbf{r}'_0, \omega_0)] \end{aligned} \right]_{\mathbf{r}_0=\mathbf{r}'_0}. \end{aligned} \quad (3.34)$$

In equation (3.34), the first and the last two terms do not contribute up to second order in position. Rejecting those terms at this point allows us to simplify the spectral density to,

$$\bar{\bar{\mathbf{S}}}_F(\omega) \approx \frac{\hbar k_0}{2\pi c} P_0 \frac{6\pi}{k_0^3} \nabla \nabla' \text{Im} [G_{xx}(\mathbf{r}_0, \mathbf{r}'_0, \omega_0)]_{\mathbf{r}_0=\mathbf{r}'_0} \quad (3.35)$$

where we find that the term corresponding to the scattering force fluctuations does not contribute to second order. This makes sense, since the scattering force scales with the gradient of the driving field at the particle's position. Expression (3.35) is in agreement with [59] for the spectral density of noise in a standing wave in front of a plane surface.

Let us now evaluate the spectral density of the force fluctuations, accounting for the presence of the spherical mirror. The presence of boundaries alters the correlations of background field fluctuations [57]. In a medium-assisted environment, the fluctuation-dissipation theorem in (3.27) holds true, but the Green's function is now altered by the presence of the boundary. In (3.35), the contribution of the boundary is encompassed in $\overline{\mathbf{G}}_s$ that makes up the total Green's function $\overline{\mathbf{G}} = \overline{\mathbf{G}}_0 + \overline{\mathbf{G}}_s$. We have already found an expression $\overline{\mathbf{G}}_s(\mathbf{r}_0, \mathbf{r}'_0)$ evaluated near the origin for a large mirror ($r_m \gg \lambda$) in section 2.3. Its derivatives can be easily evaluated since, unlike $\overline{\mathbf{G}}_0$, $\overline{\mathbf{G}}_s$ in equation (2.11) is not singular for equal position arguments,

$$\begin{aligned} \left. \nabla G_{xx}^s(\mathbf{r}_0, \mathbf{r}'_0, \omega_0) \right|_{\mathbf{r}_0=\mathbf{r}'_0} &= -\rho k^2 \frac{e^{2ik_0 r_m}}{3\pi} \int_{\mathcal{M}} d\Omega e^{-2ik_0 \hat{\mathbf{r}} \cdot \mathbf{r}_0} \rho_x(\theta, \phi) \hat{\mathbf{r}}, \\ \left. \nabla \nabla' G_{xx}^s(\mathbf{r}_0, \mathbf{r}'_0, \omega_0) \right|_{\mathbf{r}_0=\mathbf{r}'_0} &= i\rho k^3 \frac{e^{2ik_0 r_m}}{3\pi} \int_{\mathcal{M}} d\Omega e^{-2ik_0 \hat{\mathbf{r}} \cdot \mathbf{r}_0} \rho_x(\theta, \phi) \hat{\mathbf{r}} \hat{\mathbf{r}}, \end{aligned} \quad (3.36)$$

where $\hat{\mathbf{r}}$ is the radial unit vector pointing towards the mirror surface and ρ is the reflection coefficient with $|\rho| = 1$. Substituting the second derivatives into (3.35) at $\mathbf{r}_0 = (0, 0, 0)$ we have,

$$\overline{\mathbf{S}}_F(\omega) = \frac{\hbar k_0}{2\pi c} \left(\frac{1}{5} (2\overline{\mathbf{I}} - \hat{\mathbf{x}}\hat{\mathbf{x}}) P_0 + 2\text{Re} \left[\rho e^{2ikr_m} \right] \int_{\mathcal{M}} \hat{\mathbf{r}} \hat{\mathbf{r}} dP_0 \right). \quad (3.37)$$

where $dP_0 = P_0 \rho_x(\theta, \phi) d\Omega$ is the differential power radiated into the solid angle element $d\Omega$. The first term corresponds to the free space result found in the previous section for field gradient correlations, while the second term is a new term which depends only on the boundary. It can be shown that for $k_0 r_m = n\pi$ the position dependence in (3.36) vanishes to second order. The configuration of figure 3.1 studied in this section, only allows trapping of particles at mirror centre when $k_0 r_m = n\pi$ (see section 4.1). Note however, that the expression in (3.37) does not depend on the direction of beam propagation. Because of this, we find that the same expression holds for any standing wave trap polarised along $\hat{\mathbf{x}}$, such as one propagating along the $\hat{\mathbf{y}}$ direction. Such a standing wave

trap need not be formed with the beam reflection from the mirror, hence the choice of $k_0 r_m$ is not restricted in principle. We explore one example of such experimental configuration in chapter 5, with a fibre-based optical lattice formed orthogonal to the mirror axis of symmetry.

Equation (3.37) can already be evaluated, but we can write it in a more intuitive form if we write the free-space term in integral form,

$$\frac{1}{5}(2\bar{\mathbf{I}} - \hat{\mathbf{x}}\hat{\mathbf{x}}) = \int_{4\pi} \hat{\mathbf{r}}\hat{\mathbf{r}}\rho_x(\theta, \phi)d\Omega \quad (3.38)$$

Using the fact that the integral in (3.37) is symmetric about $\theta = \pi/2$ and introducing a unit step function $\Theta_m(\theta)$, we can write both terms under one integral,

$$\bar{\mathbf{S}}_F(\omega) = \frac{\hbar k_0}{2\pi c} \int_{4\pi} dP_0 \left(1 + \Theta_m(\theta)\text{Re}[\rho e^{2ik_0 r_m}]\right) \hat{\mathbf{r}}\hat{\mathbf{r}}. \quad (3.39)$$

where,

$$\Theta_m(\theta) = \begin{cases} 1, & -\theta_m \leq \theta < \theta_m, \quad \pi - \theta_m \leq \theta < \pi + \theta_m \\ 0, & \text{otherwise.} \end{cases} \quad (3.40)$$

Equation (3.39) is the main result of this section. It represents the dominating backaction noise term. For a perfectly reflecting ($\rho = -1$) full hemisphere ($\theta_m = \pi/2$) we find,

$$\bar{\mathbf{S}}(\omega) = \frac{\hbar k_0}{2\pi c} P_0 \times \begin{cases} \frac{2}{5}(2\bar{\mathbf{I}} - \hat{\mathbf{x}}\hat{\mathbf{x}}) & kr_m = n\pi \pm \pi/2 \\ \frac{1}{5}(2\bar{\mathbf{I}} - \hat{\mathbf{x}}\hat{\mathbf{x}}) & kr_m = n\pi \pm \pi/4 \\ 0 & kr_m = n\pi \end{cases} \quad (3.41)$$

Backaction noise is twice as large as the first free space noise term found in (3.32) when $k_0 r_m = n\pi \pm \pi/2$. On the other hand, at $k_0 r_m = n\pi$, the backaction noise term vanishes⁷. This *backaction suppression* condition coincides with the mirror radius condition needed for trapping at the

⁷In this case, the backaction is dominated by smaller terms which are unaccounted for in this calculation. In a later discussion, we estimate the magnitude of the residual backaction noise.

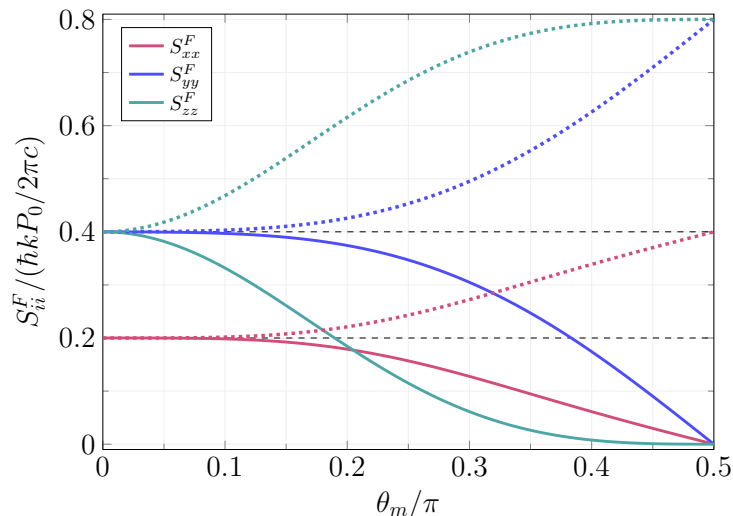


Figure 3.5: Backaction noise $S_{ii}^F(\omega)$ against spherical mirror NA found by solving (3.39) with $\rho = -1$. Explicit solutions for the curves are given in B.2. Filled lines indicate backaction for $k_0 r_m = n\pi$ while dotted lines for $k_0 r_m = n\pi \pm \pi/2$. Dashed lines indicate free-space levels in a standing wave (at $\theta_m = 0$).

mirror centre (see section 4.1), and is also the condition yielding maximum enhancement of scattered power (see section 2.3). In figure 3.5 we show how backaction in (3.39) varies with mirror polar angle θ_m . Just like in the case of measurement imprecision, we find that the rate at which backaction decreases with $k_0 r_m = n\pi$ is faster for S_{zz}^F than for S_{xx}^F and S_{yy}^F . It is easy to see by inspecting figures 3.5 and 3.3 that the shapes of the curves for the corresponding position components are the same. Indeed, when we multiply the solutions of (3.39) and (3.12) for varying θ_m (given in (B.8) and (B.6)) we find,

$$S_{\text{imp}}^i S_{ii}^F = \left(\frac{\hbar}{4\pi} \right)^2 \quad (3.42)$$

corresponding to the Heisenberg limit [3, 82, 88].⁸ Equation (3.42) is valid for

⁸Sometimes the Heisenberg limit is quoted as $\hbar^2/4$. [3]. The factor $(2\pi)^{-2}$ arises from the definition of the spectral densities in terms of angular frequencies $\omega = 2\pi f$ instead of f .

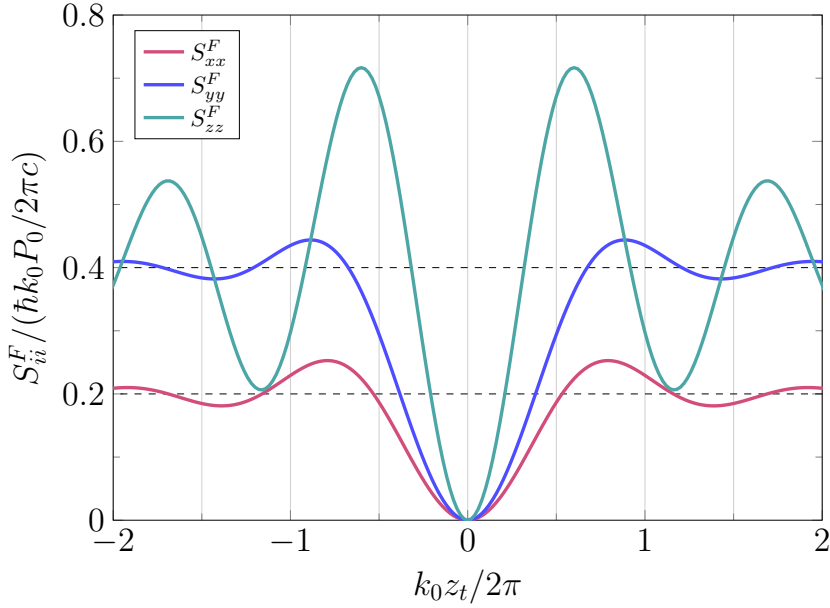


Figure 3.6: Backaction noise $S_{ii}^F(\omega)$ against displacement of the trap centre z_t along mirror axis, found by solving (3.37) to zeroth order in displacement about the trap centre. Dashed lines indicate free-space levels. Vertical lines show stable trapping positions for weak focusing ($A \approx 1$) where the solutions to (3.37) are valid approximations to backaction.

all θ_m and ρ with $|\rho| = 1$. In contrast to a free-space system, by utilising a spherical mirror one can make a trade-off between measurement imprecision and backaction by choosing an appropriate mirror radius or wavelength. For a perfectly reflecting hemisphere at $k_0 r_m = n\pi$, the detected scatter is maximally enhanced, but contains no linear position information. Correspondingly, the dominating term of backaction noise received by the particle vanishes. This reflects the fact that the flow of energy does not necessarily carry information [92]. One example of this from levitated optomechanics is for a particle trapped in a single focused beam. In that scenario, while the particle scatters light symmetrically in all directions, information about the particle's position along the beam axis propagates primarily into half-space opposite to the direction of beam propagation [82].

In view of the measurement imprecision and backaction, We can now

understand the derived suppression result. Under the suppression condition for the mirror radius, photons detected along an antipode of the spherical mirror surface do not carry linear position information as, to first order, one cannot discern whether the photons came from the particle or from its image. In direct correspondence, the spectral density of the recoil force imparted by the photons vanishes as the free-space field gradient fluctuations destructively interfere with the field gradient fluctuations from the mirror at the location of the particle. However, we note once more that this full suppression is only possible because of a standing wave trapping configuration, which suppresses fluctuations in the field amplitude for a particle located close to the intensity maximum.

To finish the analysis in this section, we consider the backaction for varying trap centre position \mathbf{r}_t along the mirror axis. We solve (3.37) with $\mathbf{r}_0 = z_t \hat{\mathbf{z}} + \delta \mathbf{r}$, expanding the expression in the integral about $(0, 0, z_t)$. The result is shown in figure 3.6, which shows oscillations of the different backaction components with the moving trap centre position. While S_{xx}^F and S_{yy}^F quickly return to their free-space value with increasing z_t , S_{zz}^F overshoots to almost twice its free-space value at around $k_0 z_t = \pm \pi$. This suggests that these points might be suitable to make significantly more sensitive measurements of position in a self-homodyne fashion.

3.4 Residual backaction noise

The suppression result found in the previous section predicts vanishing of the dominating backaction noise term under a suitable condition on the mirror radius. This however does not mean that backaction noise vanishes completely; Even under perfect experimental conditions, the calculation is subject to several approximations such as ignoring higher order scattered fields. Lifting these approximations would lead to small, additional heating terms from backaction. In sections 4.9 and 5.4.3 we investigate residual backaction noise which would arise in the experimental trapping configurations considered in this thesis as a result of scattered fields modifying the trapping potential.

The largest contributions to residual backaction noise are likely to arise from technical limitations in the experimental realisation. Imperfect mirror reflectivity will limit suppression of backaction noise to a few percent. A realisation scheme will also require surface quality and long-term mirror radius stability $\delta r_m \ll \lambda/2\pi$. Considering the coefficient of linear expansion of aluminium $\alpha_{\text{Al}} = 2.3 \times 10^{-5} \text{K}^{-1}$ and a mirror with radius of about 1 mm, sufficient radius stability can be achieved with thermal stability $\delta T < 1\text{K}$. A recent experimental proposal utilising a spherical mirror for similar application suggests that such temperature stabilisation and the quality of the fabricated mirror surface should be easily achievable [89, 100]. The mirror is also subject to thermal noise. In context of LIGO interferometers the noise is problematic in a low frequency band (up to a few hundred Hz), [101] but may require further investigation for our application.

3.5 Other noise sources

In this section, we frame the discussion of suppressed backaction noise in terms of the reheating rate, defined as the rate at which oscillation quanta are added to the oscillator's energy to compare it with other noise sources that would be present. As mentioned previously, the dynamics of a particle in an optical trap can be captured by decoupled Langevin equations for each direction (see equation (2.33)). In this case and in the absence of a feedback cooling force, the average energy of the oscillator evolves according to the following equation derived from the Fokker-Planck equation, [38, 102]

$$\langle \dot{E} \rangle = -\gamma(\langle E \rangle - E_\infty) \quad (3.43)$$

where γ and E_∞ are the mechanical damping and the equilibrium energy of thermal bath respectively. When the system is prepared in a state of low occupation out of equilibrium, the energy is subject to a constant heating rate γE_∞ . For a particle constituting a harmonic oscillator at frequency Ω this reheating rate is given by,

$$\Gamma = \frac{E_\infty}{\hbar\Omega} \gamma. \quad (3.44)$$

As a first step, we express the reheating rate due to a fluctuating force in terms of the force noise spectral density to make a link to results found in the previous section. Using the property of the spectral density for particle position component, x_i , and the Langevin equation with $\gamma \ll \Omega$, the position spread is given by,

$$\begin{aligned} \langle x_i^2 \rangle &= \int S_{ii}(\omega) d\omega \\ &= \int |\chi_i(\omega)|^2 S_{ii}^F(\omega) d\omega \\ &= S_{ii}^F \frac{\pi}{m^2 \Omega^2 \gamma} \end{aligned} \quad (3.45)$$

where we took S_{ii}^F as frequency independent. Invoking the equipartition theorem and using (3.44) leads to,

$$\Gamma_i = \frac{\pi}{2m\hbar\Omega} S_{ii}^F \quad (3.46)$$

For typical experimental parameters, free-space backaction adds quanta to the system at a rate $\Gamma \sim 10$ kHz which is consistent with experimental observations [38]. Given the discussion of residual backaction noise in the previous section, if we assume that the force noise can be attenuated by a factor $\sim 10^{-2}$, we can expect a reheating rate of $\sim 10^2$ Hz contribution from backaction. At this level, it no longer presents the dominant source of heating. In the next sections we discuss other sources of noise and their relevance in an experimental protocol for backaction suppression observation.

3.5.1 Residual gas heating

Laser induced recoil noise is a relatively weak effect. Therefore, in order to observe its influence on the motion of the trapped particle, other sources of mechanical noise have to be minimised. The particle needs to be sufficiently well-isolated from other noise sources for backaction to be visible through observations of particle dynamics. At pressures below 1 mbar, residual gas results in mechanical damping, [37, 38]

$$\gamma_{\text{th}} \approx 15.8 \frac{r_p^2}{m_p v_g} P_g \quad (3.47)$$

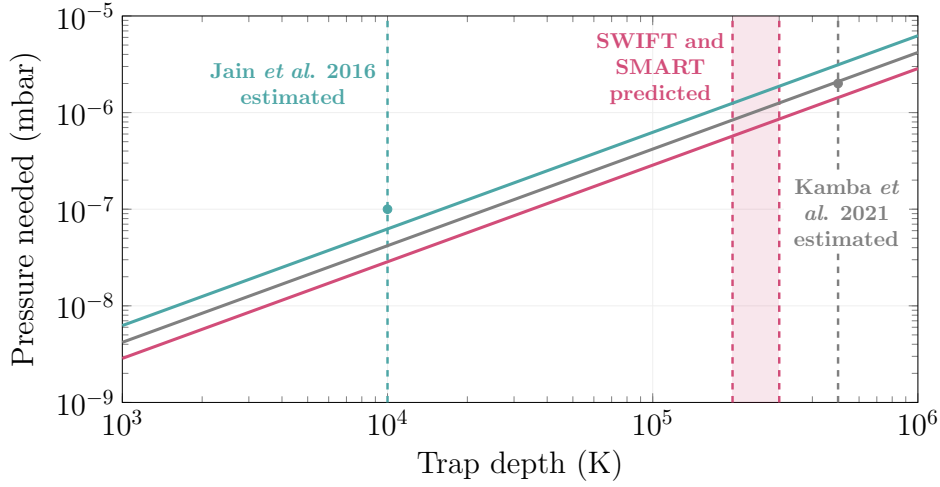


Figure 3.7: Threshold pressure (full red line) at which the heating rate from residual gas becomes comparable to laser recoil noise (based on equation (3.48)), plotted against trap depth for $r_p = 150$ nm and $\lambda = 1550$ nm. The red dashed lines with a shaded region denote trap depths achievable in the two experimental arrangements considered in the two arrangements considered in this thesis - the spherical mirror angled reflection trap (SMART) and the standing wave interference fibre trap (SWIFT). The teal and gray lines correspond to estimates of a trap depth based on the experimental parameters in an observation of laser recoil noise by Jain *et al.* [38, 103] and Kamba *et al.* [104] respectively. We also show the corresponding threshold pressure trends using (3.48) for their experimental parameters marked with the same colours.

where v_g and P_g are the r.m.s. velocity and pressure of the gas molecules, and r_p and m_p are the radius and mass of the trapped particle, respectively.

Comparing the reheating rate due to (3.47) with backaction reheating gives an estimate for the threshold pressure needed for free-space backaction noise observation. Using (3.47), (3.44), (3.46) and expressions for free-space recoil heating (3.33), we find,

$$P_g \approx 0.16 \frac{v_g}{r_p^2 k_B T} \frac{\hbar k_0}{2\pi c} P_0. \quad (3.48)$$

Figure 3.7 shows the threshold pressure plotted against trap depth for a 150 nm radius silica particle. Although excessively large trap depths may be unnecessary or even detrimental in common experiments, it is imperative if laser recoil noise observation is the primary objective, and ultrahigh vacuum

pressures are not accessible. Since observation of recoil noise is the main subject of this thesis, in the following chapters discussing experimental arrangements we consider larger particles (within the dipole approximation) and high laser powers.

3.5.2 Laser intensity noise

The spring constant in an optical trap is proportional to local field intensity, which makes the particle susceptible to parametric heating due to fluctuations in the laser power. Intensity noise leads to heating of the oscillator energy at a rate, [105]

$$\langle \dot{E} \rangle = \frac{\pi}{2} \Omega^2 S_{\text{RIN}}(2\Omega) \langle E \rangle, \quad (3.49)$$

where Ω is the trap frequency and S_{RIN} is the one-sided spectral density of relative intensity noise of the laser. Since the intensity noise is evaluated at twice the trap frequency, the heating rate is different along orthogonal directions. The expression is also proportional to the average oscillator energy $\langle E \rangle$, making this heating mechanism exponential. If residual gas heating is minimised, the intensity noise is the dominant heating mechanism in the absence of feedback cooling. Using the shot-noise level as an estimate, in our laser setup,⁹ we find $S_{\text{RIN}} = -132$ dB/Hz. If the oscillator is in equilibrium with the thermal bath (here assumed the residual gas) then $\langle E \rangle = (1/2)k_B T$, at room temperature intensity noise gives rise to a reheating rate of $\Gamma \sim 2$ MHz. However, the effect of intensity noise can easily be rendered negligible with feedback cooling, as was done in [38], by cooling the center of mass motion below ~ 1 K.

3.5.3 Laser phase noise in a standing wave

Standing wave traps are susceptible to noise in the position of the trap centre due to laser frequency instabilities. Laser frequency stability can be improved by orders of magnitude by employing the Pound-Drever-Hall (PDH) technique

⁹Seed laser: LN-focus 32, EDFA: HPOA-S

[104,106]. The technique relies on tuning the laser frequency using a frequency error measurement, derived from light reflected from an optical resonator. In standing wave traps formed by laser retroreflection, this laser phase noise is proportional to the mirror-particle distance. For large separations, the resulting fluctuations in the trap centre can be the dominating source of mechanical noise [104]. A combination of frequency stabilisation and reduction of the particle-mirror separation in a standing wave trap experiment has recently enable to render laser phase noise negligible [104], enabling laser recoil-limited detection and ground state cooling.

3.6 Concluding remarks

In summary, we have analysed the effect of the spherical mirror geometry on the minimum imprecision in a trapped particle position tracking experiment, and the corresponding backaction noise experienced by the particle. We have found that under a suitable condition on the mirror radius, the mirror significantly attenuates the attainable acquisition rate of linear position information, at the same time suppressing the largest backaction noise term. In the case that the mechanical noise experienced by the particle is dominated by backaction and the detection is shot-noise limited, we have shown that the imprecision and backaction noise satisfy the Heisenberg limit of detection for any choice of mirror radius r_m and spanning half-angle $\theta_m < \pi/2$. Experimental considerations show that the suppression scheme should be achievable in a realistic setting.

The main result shows a strong dependence of the imprecision-backaction characteristics on the surrounding mirror geometry. The spherical mirror geometry is uniquely suited for point-like particles as the mirror reflection can perfectly match dipole emission away from the mirror. Other geometries may present similar useful properties in future investigations, such as a plane mirror-lens system. Other practical arrangements suitable for the scattering properties of particles with different and more complex morphologies may be found by adapting existing analysis tools, used for tailoring the optical

properties of nanoscale emitters [72, 107]. We once again note that although the spherical mirror geometry plays a necessary role for the suppression effect, it is not sufficient; a standing wave trapping potential is also required to remove the contribution of the local phase gradient, which would be present in a single-beam configuration [82].

In the next chapters, we propose and analyse two experimental trapping arrangements which could be used for the purpose of studying particle dynamics at the centre of a (hemi-)spherical mirror. A protocol for feedback cooling and systematically positioning the particle at the centre of the spherical mirror will require further investigation. It is worth noting that second-order position information in suppressed scatter is still available, which should be sufficient for parametric feedback cooling [102]. Away from the suppression condition on the mirror radius, it may be possible to employ a passive cooling scheme, by dynamical backaction mediated by the spherical mirror itself [108]. Such a scheme would further extend the utility of trapping near a spherical geometry.

Chapter 4

SMART: Spherical mirror angled-reflection trap

There are many ways to realise an optical trap which confines the particle to the centre of a spherical mirror. One that takes advantage of the available solid angle, allowing us to trap in front of a full hemisphere, uses the mirror to reflect the incident laser beam to form a counter-propagating beam trap (as shown on the left figure 4.1). In this way, the standing-wave pattern of the trapping field becomes dependent upon the beam-mirror alignment. This places constraints on the mirror radius and the focus position of the beam which yield sufficient intensity modulation for trapping and a field maximum at the mirror centre. In the next section we discuss these constraints.

While convenient for trapping, aligning the beam along the mirror's axis of symmetry obstructs particle observation, as the signal is swamped by the trapping beam backreflection. We experimentally circumvent this limitation by illuminating the trapping lens off-centre, yielding the beam inclined about the mirror centre in order to spatially separate the trapping beam from particle scatter (see figure 4.1). Following section 4.2, we present we discuss experimental results obtained in the implemented SMART arrangement.

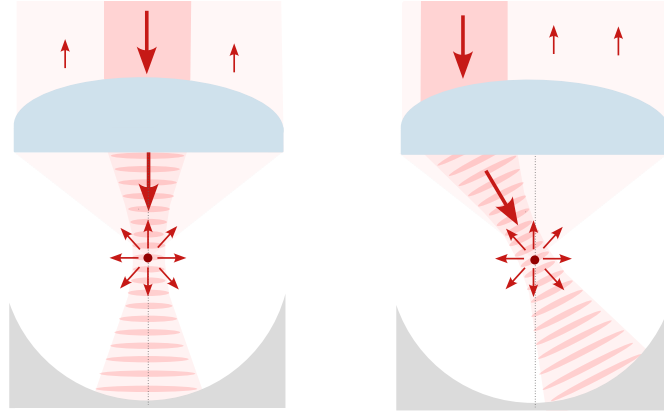


Figure 4.1: Diagram showing the difference between (right) the SMART configuration and (left) an ordinary standing wave trap formed along the mirror axis of symmetry. In both diagrams we are assuming that the beam is polarised out of the page. In the setup on the left, central region of the lens is swamped by laser retroreflection and the particle scatter cannot easily be accessed for detection. In the setup on the right, particle scatter is spatially separated from the trapping beam. In both diagrams the same portion of the solid angle is available, but it is easier to access isolated scatter when the trapping beam is angled. Because of the spherical symmetry about the mirror centre, the conditions for retroreflection in both setups are the same.

4.1 Beam reflection from a spherical mirror

Let us first consider the setup depicted on the left of figure 4.1. In the setup, the origin of the coordinate system coincides with the centre of the spherical mirror. The laser beam is propagating along the z axis, and is focused to a point z_f .

We initially focus on maximising the modulation of the intensity standing wave pattern. In a counter-propagating beam trap, intensity modulation is maximum when the two interfering beams have equal magnitudes in space but propagate in opposite directions. For this we require the incident laser beam to be *retroreflected* from the mirror surface, which occurs when the curvature of the beam's wavefronts matches the curvature of the mirror [85]. To this end, we seek a condition on the beam focus position z_f that matches this requirement. We refer to this as the *retro-reflection condition*.

Modelling the laser as a paraxial Gaussian beam with waist w_0 , [85]

$$\mathbf{E}(\rho, z) = E_0 \frac{w_0}{w(z)} \exp\left(-\frac{\rho^2}{w(z)^2}\right) \exp\left(i\left[kz + k\frac{\rho^2}{2R(z)} - \phi_g(z)\right]\right) \hat{\mathbf{x}} \quad (4.1)$$

where the characteristic beam parameters are,

$$\begin{aligned} w(z) &= w_0 \sqrt{1 + \left(\frac{z}{z_R}\right)^2} && \text{Waist radius} \\ R(z) &= z + \frac{z_R^2}{z} && \text{Radius of curvature} \\ \phi_g(z) &= \arctan\left(\frac{z}{z_R}\right) && \text{Gouy shift} \\ z_R &= \frac{\pi w_0^2}{\lambda} && \text{Rayleigh range} \end{aligned} \quad (4.2)$$

and we are considering field of a beam focused at z_f , $\mathbf{E}(\rho, z - z_f)$. The beam is retroreflected at the mirror surface when its radius of curvature matches that of the mirror,

$$r_m = R(z - z_f) = z - z_f + \frac{z_R^2}{z - z_f} \quad (4.3)$$

which has two solutions for the focus position,

$$\begin{aligned} z_f^\pm &= \frac{r_m}{2} \left(1 \pm \sqrt{1 - 4\frac{z_R^2}{r_m^2}}\right) \\ &\approx \frac{r_m}{2} \left(1 \pm \left[1 - 2\frac{z_R^2}{r_m^2}\right]\right) \end{aligned} \quad (4.4)$$

where we assumed that $z_R \ll r_m$. Solutions z^+ and z^- correspond to the beam focus close to the mirror centre or to the mirror surface respectively. Since we want the laser intensity at the trapping position to be as large as possible, we choose the negative sign solution. Therefore, we can achieve maximum modulation when the beam is focused a distance z_R^2/r_m from the mirror centre towards its surface. Note that since $z_R \approx \lambda/\pi(\text{NA})^2$ for a beam of numerical aperture specified by NA, the tighter the focus of the beam, the closer the

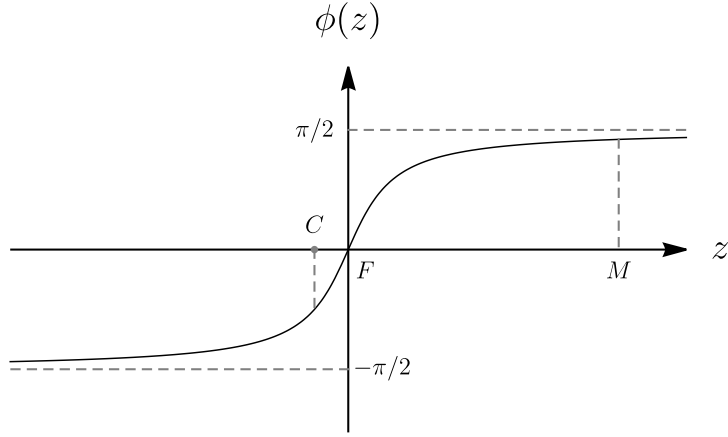


Figure 4.2: Contribution of the Gouy phase shift of a Gaussian beam to the round-trip phase. The beam is focused to point F ($z = z_f$) about the mirror centre C ($z = 0$). The beam is reflected at M ($z = r_m$). When points C, F and M correspond to those that yield retro-reflection, the Gouy phase difference between C and M is equal to exactly $\pi/2$.

solution z_f^- is to the centre of the mirror. We now turn to the problem of finding a condition on the mirror radius which yields an intensity maximum at the centre of the mirror. To do this, we consider the round-trip phase about the mirror centre. For a plane wave reflecting from a perfect plane mirror a distance r_m away this round-trip phase would simply be equal to $2kr_m + \pi$. For a Gaussian beam, there is an additional contribution arising from the Gouy phase shift. With the focus at z_f^- we find that,

$$\Delta\phi = 2kr_m + \pi + \underbrace{2[\phi_g(z_f) + \phi_g(r_m - z_f)]}_{\pi} = 2kr_m \quad (4.5)$$

that is, the contribution of the Gouy phase shift to the round-trip phase is equal to exactly π when the beam is retroreflected (see figure 4.2), such that the total phase is fixed only by the round-trip distance. To ensure that the incident beam is in-phase with its reflection at the centre, the mirror radius has to be restricted to,

$$kr_m = n\pi \quad (4.6)$$

where k is the wavenumber. This condition corresponds to the maximum enhancement of scattered power from a trapped particle. In the trapping configuration considered in this section, the adjustment of the mirror radius away from (4.6) in an experiment would shift the intensity from a maximum to a minimum. However, as we discussed in the previous chapter, the condition in (4.6) is exactly the condition needed to achieve suppression of force noise acting on a trapped particle. This coincidental feature of the SMART arrangement ensures that the recoil noise suppression condition is matched when the particle is brought to the centre of the spherical mirror.

4.2 Experimental implementation introduction

In the following sections we discuss the experimental implementation of the SMART arrangement, constructed during the project and used for trapping of 300 nm diameter silica particles in front of a spherical mirror. We begin the discussion by looking at the setup of hybrid fibre and free-space optics used for trapping and detection, followed by the method of particle loading and the vacuum system used. We also develop a model for the SMART detection system, which generates unique spectral lineshapes for the motion of the nano-sphere. We then present the experimental results and use them for trap characterisation. Although we have not reached the final observation at the centre of the spherical mirror, at the end of the chapter we outline potential protocols for positioning the particle at the mirror centre and recoil noise suppression observation.

4.3 Laser system and trapping optics

The setup used is shown in figure 4.3. The system is based on the low-noise 1550 nm telecom fibre laser LN-focus-32 from LN Solutions. The laser generates about 50 mW of optical power, 10 % of which was used to seed the erbium-doped fibre amplifier (EDFA), to be used for trapping. The remaining 90 % was either dumped, used as reference for interferometric measurement,

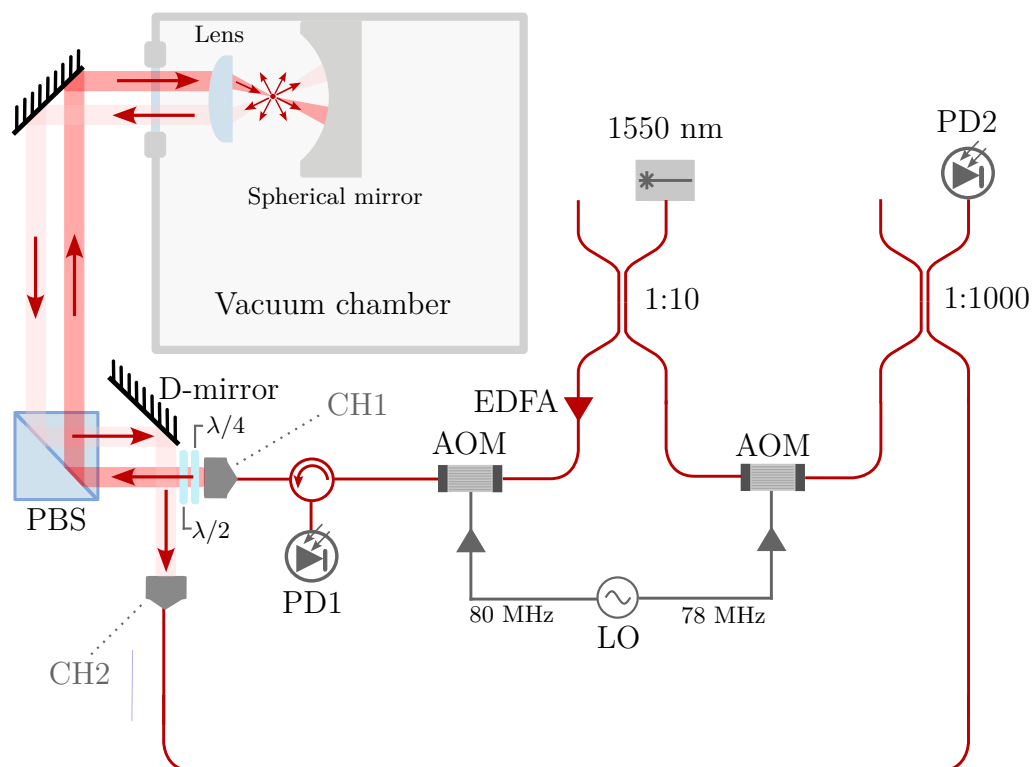


Figure 4.3: Implementation of the SMART arrangement, used to obtain the experimental results in this chapter. Crimson lines represent optical fibres. 10 % of the 1550 nm laser is used to seed the erbium-doped fibre amplifier (EDFA) that is then used for trapping via the trapping channel (CH1). The remaining 90 % is used either dumped or used as reference for heterodyne detection with the collected scatter via the detection channel (CH2) on the photodiode PD2. Photodiode PD1 was mainly used to assess alignment of CH1 beam by measurement of back-reflection coupled into fibre. $\lambda/2$ and $\lambda/4$ denote waveplates used to control polarisation. The local oscillator was used to modulate the trapping light's frequency for heterodyne detection, and the intensity via the acousto-optic modulators (AOMs).

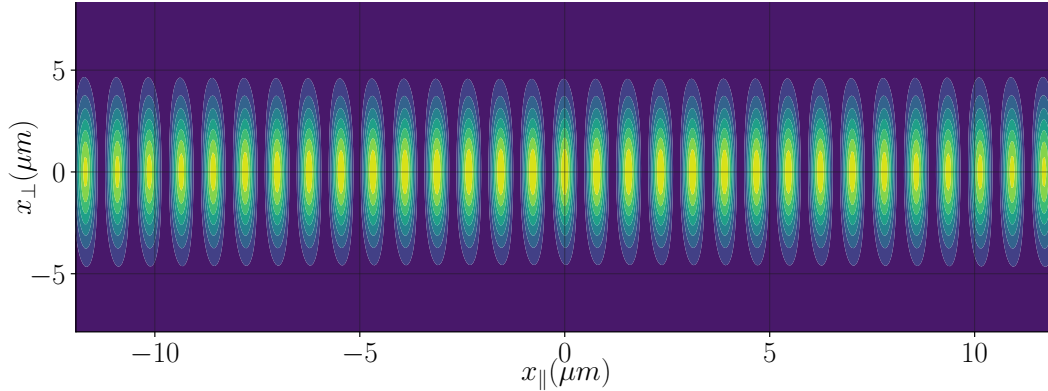


Figure 4.4: Intensity profile of the trapping field in SMART about the beam focus - a superposition of two identical counter-propagating Gaussian beams with the waist $w_0 = 4.5 \mu\text{m}$. The beam axis is inclined at a shallow angle to the mirror axis of symmetry. On the plot x_{\parallel} and x_{\perp} denote coordinates parallel (fast) and perpendicular (slow) to the beam axis respectively.

or sent through the detection channel (labelled CH2 in figure 4.3) to assess alignment. The erbium-doped fibre amplifier (EDFA) (BKTEL HPOA-S from Laser 2000) was used to amplify the trapping light to powers upwards of 4 W. Due to unavoidable losses in the acousto-optic modulator (AOM), the final power sent into the trap site via the trapping channel (labelled CH1 in figure 4.3) was kept at around 1.5 W - 2 W. Although these powers may seem excessively high compared with other experiments utilising the 1064 nm wavelength, our laser system allowed us to stably trap silica nanoparticles at pressures below 7×10^{-6} mbar.

Fibre optic components were connected using the single-mode telecom fibre SMF-28, which is not polarisation maintaining. Because of this, the system was subject to thermal drifts in polarisation, which we controlled using half- and quarter-wave plates in free-space upon the light leaving the fibre (denoted $\lambda/2$ and $\lambda/4$ on the figure 4.3)

The SMART trapping potential was realised by significantly underfilling an aspheric lens with a collimated beam, translated horizontally away from the lens's centre as depicted in figure 4.1. The laser light leaving the fibre was collimated using the TC18APC-1550 triplet collimator from Thorlabs, and

focused with a 25 mm diameter, 0.83 NA aspheric lens from Edmund optics¹. Using the specifications of the lens and the collimator we estimate the effective numerical aperture used for trapping as 0.11. This is a relatively low degree of focusing that allows us to safely treat the focused light as a paraxial Gaussian beam. When aligned with the spherical mirror for retroreflection as discussed in the previous section, this arrangement generates a standing wave intensity profile with a waist $w_0 = \lambda/(\pi\text{NA}) = 4.5 \mu\text{m}$ and is non-diverging near the waist over many wavelengths along the beam axis (see figure 4.4). In a well-aligned setup, the scattering force is negligible and we can estimate the trap depth using the optical potential $U = -\alpha I/4$ from the optical intensity I at the waist, and the local second derivative to estimate the trap frequencies from the spring constant. At 1.5 W illuminating power, the SMART arrangement should generate a trap depth of about $2.8 \times 10^5 \text{ K}$, with slow and fast oscillation frequencies $\Omega_{\perp} \approx 2\pi \times 24 \text{ kHz}$ and $\Omega_{\parallel} \approx 2\pi \times 315 \text{ kHz}$ respectively. We have observed notable discrepancies from these estimates in the captured spectra of the signal, which we will discuss later on in the chapter.

For the spherical mirror, we have used a 25 mm diameter, protected gold spherical mirror with radius of curvature of 20 mm, from Edmund optics². The mirror is specified at $>96 \%$ reflectivity and has an numerical aperture of about 0.63. Results found in the previous chapter suggest that a mirror of this NA should exhibit appreciable suppression of backaction noise (at least $\sim 50\%$ reduction along the mirror axis, see figure 3.5 at $\theta_m \approx 0.22\pi$), appropriate for an initial demonstration; A future experiment can always be extended to incorporate a full hemispherical mirror.

The spherical mirror was mounted on a three-axes, vacuum-compatible translation stage from Standa³ which we used for system alignment. The intensity profile of the trapping light is strongly dependent on the degree of

¹<https://www.edmundoptics.co.uk/p/25mm-dia-083-na-uncoated-1550nm-nir-aspheric-lens/45821/>

²<https://www.edmundoptics.co.uk/p/25mm-dia-x-10mm-fl-protected-gold-concave-mirror/5325/>

³https://www.standa.lt/products/catalog/vacuum_compatible_stages?item=404&prod=vacuum-compatible-translation-system

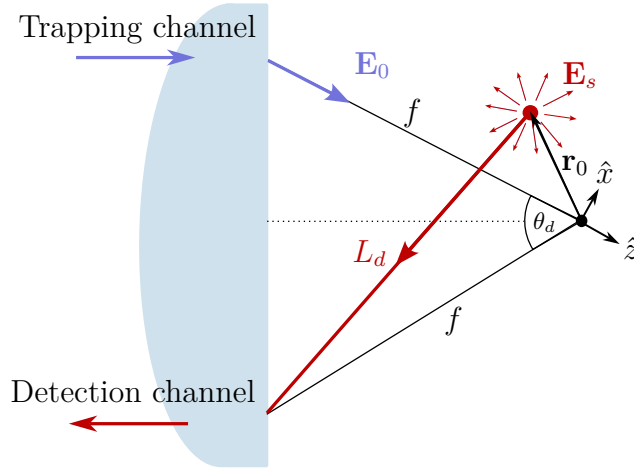


Figure 4.5: Detection geometry in SMART. The lens is illuminated off-axis with trapping light \mathbf{E}_0 and focused. The trapping light is polarised out of the page along $\hat{\mathbf{y}}$. The particle, displaced from the focus by a distance $|\mathbf{r}_0| \ll f$, scatters with the field \mathbf{E}_s and detected off-axis at a distance L_d .

alignment, which was assessed based on reflected power coupled back into fibre at CH1 and CH2 collimators, and measured on PD1 and PD2 respectively.⁴ The power which couples back into fibre relies on mode-matching of the reflected beam-spot at the endface of the collimators (see section 5.4.1). In the experiments, we have reached a maximum back-coupled power of reflected light of about 40 % on both channels.

4.4 Particle detection

We begin the discussion of particle position detection by presenting a simple model for the detection signal. We then follow with the experimental details of detection in our implementation of SMART.

⁴To align the detection channel, fibres were reconnected to send the seed laser light, ordinarily used as a reference field for detection, down CH2 to measure the reflected power coupled back into fibre.

4.4.1 Model of the detection signal

In order to correctly identify individual particles using interferometric detection, we need a model for the detection signal. Interferometric particle detection in SMART gives rise to a unique lineshape of the signal spectrum where spectral peaks appear not only at frequencies corresponding to the mechanical motion but also at frequency sidebands corresponding to the sum and difference of the fast and slow oscillation frequencies. We show this by considering ordinary homodyne detection of the particle scatter as depicted in figure 4.5. The particle scatters laser light which is captured on the other end of the lens, separating it from the trapping light. The motion of the particle at the trap site modulates the phase ϕ_d of the detected scatter, which is probed by mixing the captured light with a reference field.

Since the trapping light forms a standing wave with its reflection from a spherical mirror, to first order in the particle displacement the trapping light does not contribute to phase sensitivity⁵. Therefore, the phase sensitivity only depends on the distance L_d of the particle to the lens along the detection channel, and we approximate the scatter as having constant amplitude. Using the simple geometric model presented in figure 4.5 we find that the phase response to the particle displacement decomposed at the focus with respect to the trapping channel is given by,

$$\phi_d = kL_d - kf = k\sqrt{r_0^2 + f(x_0 \sin \theta_d - z_0 \cos \theta_d)} \quad (4.7)$$

where $r_0^2 = x_0^2 + y_0^2 + z_0^2$. When the detected scatter is mixed with a reference field at the same optical frequency, the signal observed on the photodetector has the form,

$$V(t) \propto \cos(\phi_d(t) + \varphi(t)) \quad (4.8)$$

where ϕ_d corresponds to phase modulation kL_d by particle motion and φ is the remaining phase accrued due to the optical path difference between the detected scatter and the reference light. Note that we explicitly kept

⁵motion at an intensity maximum of a standing wave only modulates the intensity of the scatter from second order of particle displacement

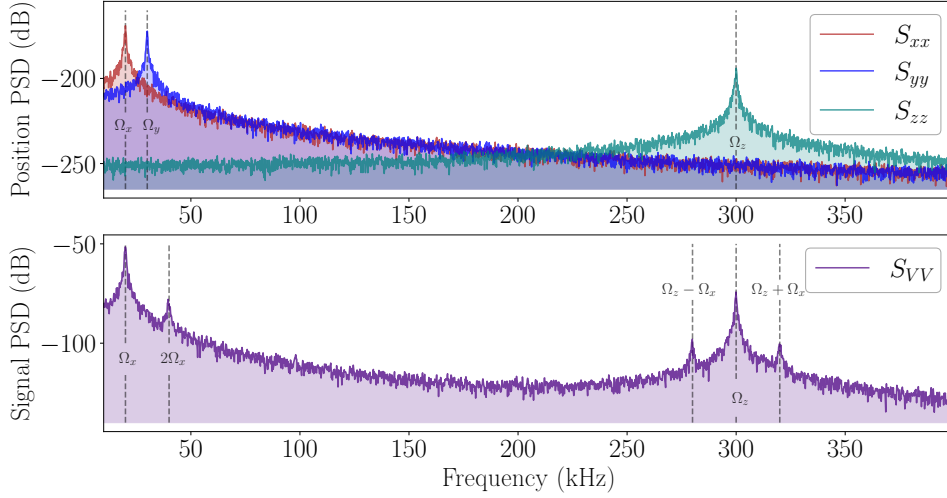


Figure 4.6: Stochastic harmonic oscillator simulation data for simulation time of 34ms with $\Omega_x = 2\pi \times 20$ kHz, $\Omega_y = 2\pi \times 30$ kHz and $\Omega_z = 2\pi \times 300$ kHz. The temperature and the damping rate was chosen equal to $T = 300$ K and $\gamma = 2.2$ kHz respectively, which corresponds to 1 mbar environment pressure. **Top:** Position spectral densities of the oscillators along x, y, z . **Bottom:** Corresponding signal spectral density with $\theta_d = \pi/4$, a constant phase offset $\varphi = \pi/4$ and $f = 1.5$ cm.

time dependence in both terms; in φ the time dependence can arise due to incoherent instabilities in either of the interferometer arms, such as slow thermal drifts in optical fibre and free-space optical elements or mechanical vibrations.

It is difficult in general to accurately model the analytical spectrum of the signal (4.7) generated by the particle motion [109]. To understand the spectral features of the detection signal in the SMART geometry, we instead use the signal in (4.7) as a transfer function for particle displacement data derived from a numerical simulation of a stochastically-driven damped harmonic oscillator simulated using the Euler-Maruyama method. We model each component of particle displacement as an independent oscillator with its own mechanical frequency $\Omega_x, \Omega_y, \Omega_z$ subject to damping γ and bath temperature T , [110]

$$\begin{aligned}\ddot{i}(t) + \gamma\dot{i}(t) + \Omega_i^2 i(t) &= \frac{1}{m}\mathcal{F}_i(t) \\ \langle \mathcal{F}_i(t)\mathcal{F}_i(t') \rangle &= \sqrt{2m\gamma k_B T}\delta(t-t')\end{aligned}\tag{4.9}$$

for $i = x, y, z$. Results of one simulation run are shown in figure 4.6. We find that apart from spectral peaks corresponding to first-order harmonics of the x and z motion, additional peaks appear on the spectrum at $\Omega_z \pm \Omega_x$. The sidebands are a feature of the signal rather than mechanical motion, a feature reminiscent of the spectra of modulated signals in radiofrequency communications and in other levitated optomechanical systems such as motional spectra of non-spherical levitated particles [111].

Although in a well-aligned system we expect the frequencies Ω_x and Ω_y to be equal, for the simulation we have chosen $\Omega_x \neq \Omega_y$ to see how the two frequencies are represented in the signal. As expected, a first-order harmonic corresponding to Ω_y is not visible in the signals since the phase ϕ_d does not carry linear y information. More interestingly, there appears a strong second-order peak $2\Omega_x$, but the second order peak at $2\Omega_y$ is not visible. This is because the peak at $2\Omega_x$ originates from the second term under the square-root in equation (4.7). The sensitivity of this term is amplified by the length factor f which in the experiment is larger than particle displacement by several orders of magnitude. The other, second-order term is visible on the spectrum at lower pressures.

The relative amplitude of the spectral peaks of the signal depends on the offset phase φ and the angle θ_d . At $\theta_d = 0$ and $\theta_d = \pi/2$ we only retain first-order peaks of either z or x motion respectively, and there is no sideband structure. This is clear from the diagram in figure 4.5, as in the case of $\theta_d = 0$ or $\pi/2$ the system is sensitive to only one of either z or x to first order. In the experiment, the centres of the beam spots of the trapping and detection channels were separated by about 1 cm with the lens focal length of 1.27 cm giving $f = 1.62$ cm and $\theta_d = 37.7^\circ$. These values are comparable to those chosen for the simulation. While θ_d is under experimental control, φ is determined by the remainder of the optical path. This phase determines the relative height of even- and odd-numbered spectral peaks. Note that the peaks

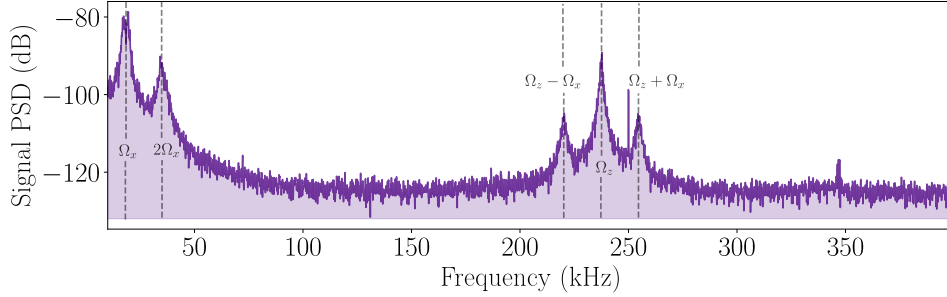


Figure 4.7: Experimental spectral density of a homodyne signal captured at 1.9 mbar. Using our model we can identify the fast and slow trap frequencies to appear at about $\Omega_z = 2\pi \times 237$ kHz and $\Omega_x = 2\pi \times 17.3$ kHz respectively.

in the spectrum of figure 4.6 at Ω_x , Ω_z are first-order (odd-numbered), while $2\Omega_x$ and the sidebands $\Omega_z \pm \Omega_x$ are second-order (even-numbered). Therefore, variation of φ affects the contrast between Ω_z and its sidebands. In the simulation we have chosen $\varphi = \pi/4$ which qualitatively agrees with typical signal spectra obtained in the experiment (see figure 4.7), which shows that both the first-order and second-order peaks are visible.

4.4.2 Detection optics

To observe the motion of the particle we have used the collimator F280APC-1550 from Thorlabs, which has similar specifications to the collimator on the trapping channel and gives a collection NA of 0.1. In this way we expected to capture about 1 % of the particle scatter or 3.5 μW for a 300 nm diameter nanoparticle.

For detection, we have used the InGaAs PIN photodiode HCA-S-200M-IN. The detector has noise-equivalent power (NEP) of 5.2 $\text{pW}/\sqrt{\text{Hz}}$, making 300 nm particles easily detectable. The linear response of this photodiode saturates at 60 μW . To stay within this range we have tuned the power of the reference field to about 10 μW .

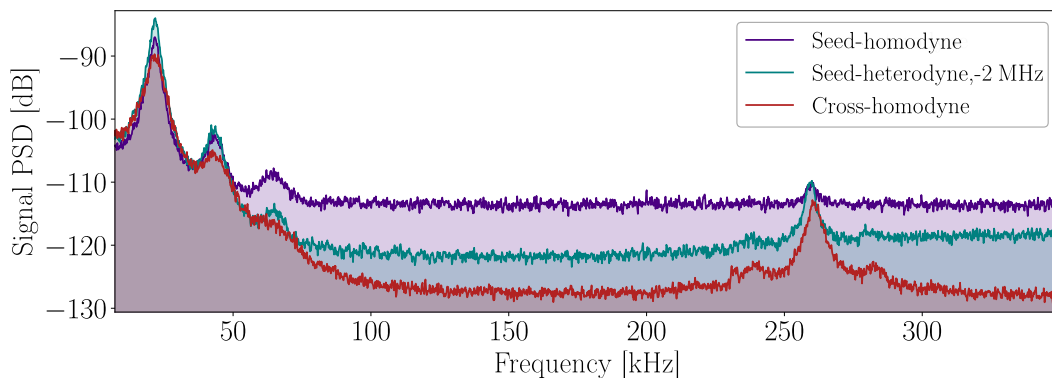


Figure 4.8: Signal spectra captured for a particle trapping event using the cross-homodyne reference (at 7.9 mbar) and with addition of a heterodyne reference (at 4.8 mbar) derived from the seed laser. The teal line corresponds to the heterodyne spectrum shifted down by 2 MHz for comparison. The power of both reference fields was tuned to about 10 μW . The spectra were taken 3 minutes apart. The cross-homodyne method allowed us to consistently reach lower noise-floors compared with the other detection methods.

4.4.3 Detection methods

In developing the experiment, we have explored various detection methods, differing in the source of the reference field. For ease of reference, we will name them as follows:

1. *Seed-homodyne*: Detection with a portion of the seed laser's power used as reference, mixed with the detected scatter using a fibre tap coupler at PD2 (see figure 4.3)
2. *Seed-heterodyne*: Detection with a portion of the seed laser's power used as reference, offset from the detected scatter by 2 MHz by the AOM modulation
3. *Cross-homodyne*: Detection with a small portion of the trapping laser power, back-reflected from the spherical mirror and *cross-coupled* onto the detection channel

Due to the large path difference in the constructed setup between the seed reference field and the detected scatter, seed-homodyne detection was

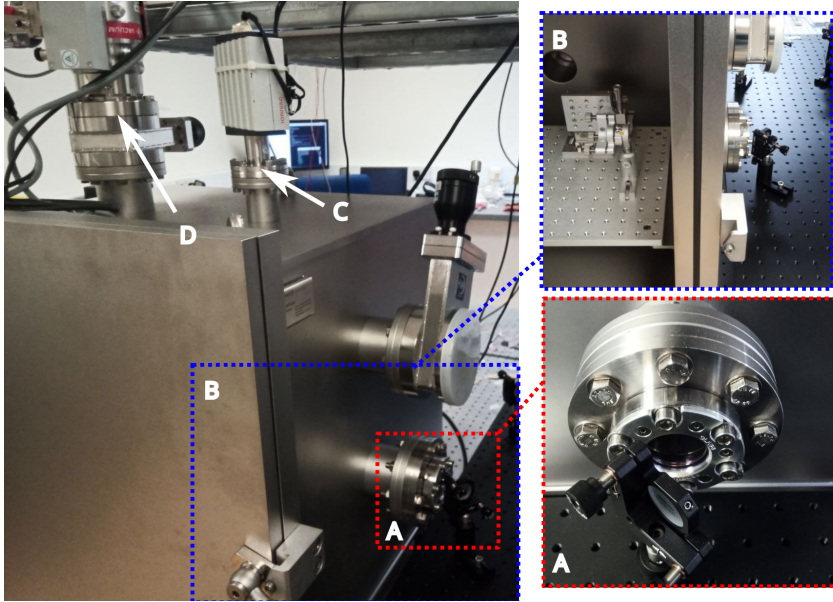


Figure 4.9: Picture of the vacuum system. The different labels denote the following components - (A) AR-coated viewport through which the laser was sent, (B) chamber door where the blue inset shows the inside of the chamber with the door open showing the optics inside the chamber, (C) flange connected to the pressure gauge ITR 90 from Leybold used to take pressure readings below 100 mbar, (D) Flange connected to the vacuum pumps.

extremely sensitive to thermal drifts and mechanical vibrations of the fibres and free-space optical elements, necessarily leading to additional noise.

The trapping and detection channel collimators were mounted on 5-axis kinematic mounts, initially used to ensure that only scatter gets captured onto the detection channel. We have found that a homodyne reference field can be derived by bringing the trapping and detection collimators closer together to couple a small portion of trapping light onto the detection channel. This limits the path difference to the roundtrip between the particle and the mirror, which results in a significantly more stable signal less susceptible to perturbations of the constructed setup. We show one example comparison of the spectra in figure 4.8. Because of the improvement to stability, a cross-homodyne detection reference field was used for the majority of the data captured in the experiment.

4.5 Vacuum system

To be able to house the trapping optics and the translation stage on which the spherical mirror was mounted (in total at least $\sim 0.008 \text{ m}^3$), we employed a large vacuum chamber DN 500 cubical from Pfeiffer Vacuum with internal volume of 0.125 m^3 . For evacuation, we used two pumps operated in different pressure regimes; Scroll pump nXDS6i from Edwards Vacuum was used to bring the chamber from atmospheric pressure down to $10^0 - 10^{-2}$ mbar. At 1 mbar, we engaged the turbo pump HiPace 80 from Pfeiffer Vacuum to lower the pressure further into the high vacuum regime. The constructed vacuum system is depicted in figure 4.9. Using this system we have reached a minimum pressure of 5×10^{-6} mbar. For the considered laser and particle parameters, according to figure 3.7 this pressure is insufficiently low for photon recoil noise observation. However, the chamber is specified to be able to reach 10^{-7} mbar, therefore a future experiment could be extended to reach the necessary pressure threshold with additional pumping. This pressure threshold can also be brought up closer to the pressure attained in the chamber by trapping larger particles or increasing the laser power (see equation (3.48)).

4.6 Particle loading

Particles were introduced into the trap site by spraying an aerosolised nanoparticle solution with a medical nebuliser (MICRO AIR from Omron) before evacuating the vacuum chamber. The particles were prepared with a concentrated 10 mg/mL solution of 300 nm diameter silica nanospheres from nanoComposix. The solution was then further diluted with distilled water to a concentration of $2 \text{ }\mu\text{g/mL}$ to yield about ~ 3 particles per droplet forced through the mesh of the nebuliser. Before use, each solution batch was sonicated for about 1 hour in an ultrasonic bath.

We delivered the spray of nanoparticles through the main door of the vacuum chamber. The open door visibly exposed the trap site to perturbing air which prevented successful trapping. To contain the spread of the aerosol

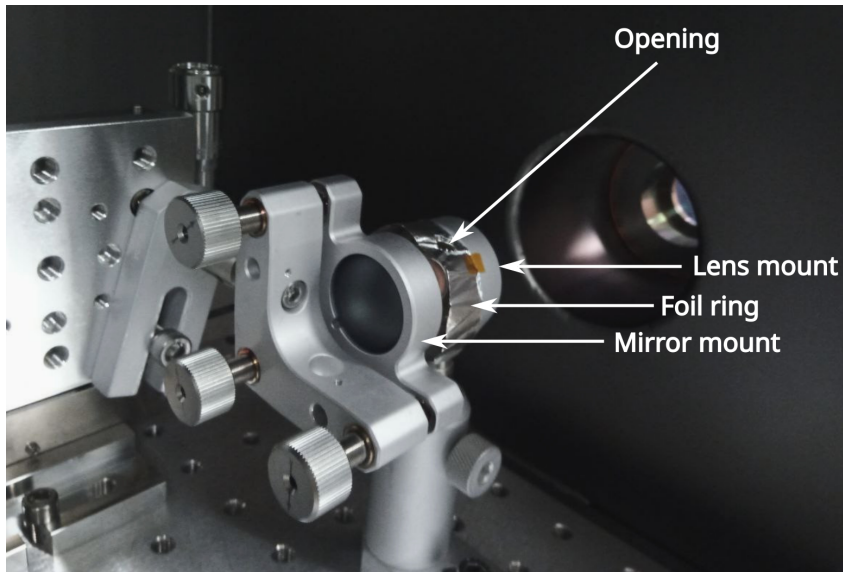


Figure 4.10: Optics inside the vacuum chamber. Aluminium foil ring was fixed around the lens mount to contain the spread of the nanoparticle solution. The solution was sprayed through the narrow opening in the foil ring through a narrow tube.

in the chamber and shield particles from persisting air currents, we introduced a narrow aluminium foil ring around the lens mount (see figure 4.10). The particles were delivered through a small opening in the foil ring.

4.7 Discussion

In the experiment, the SMART configuration proved to be a robust platform for trapping in levitated optomechanics. In this first iteration of the experiment, we were able to reach 6.2×10^{-6} mbar pressure without losing the particle, with trapping times on the order of days without feedback cooling. However, we have made several observations which deviate from the desired trap performance. To be able to make the necessary improvements, we describe these observations in this and the following sections.

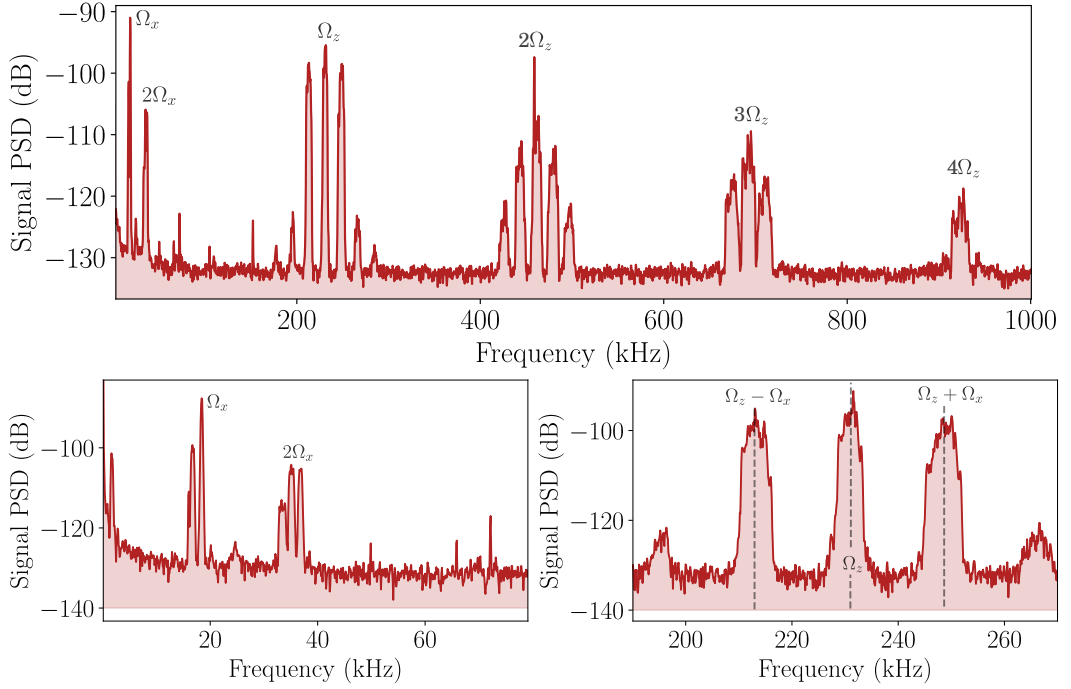


Figure 4.11: Cross-homodyne signal PSD captured at 5.2×10^{-5} mbar. The bottom plots show the spectrum around the slow oscillation frequency range of Ω_x , Ω_y (bottom left) and the fast oscillations Ω_z (bottom right)

4.7.1 Trap performance

Consistently, the mechanical frequencies of the trapped particles measured lower than what is expected from a calculation based on the local intensity (see section 4.3). Let us focus the discussion on the fast oscillation frequency Ω_z for which we expected 315 kHz. For most particles trapped, we observed Ω_z of around 250 kHz. Trapping around 315 kHz was possible, although less probable and unstable. Figure 4.12 shows a series of snapshots captured during pump down from 50 mbar which demonstrates this. Spectral peaks corresponding to two particles at 220 kHz and 315 kHz are clearly visible. As the pressure decreases, the lower frequency peak remains at 220 kHz, while the 315 kHz drifts down in frequency before the particle eventually

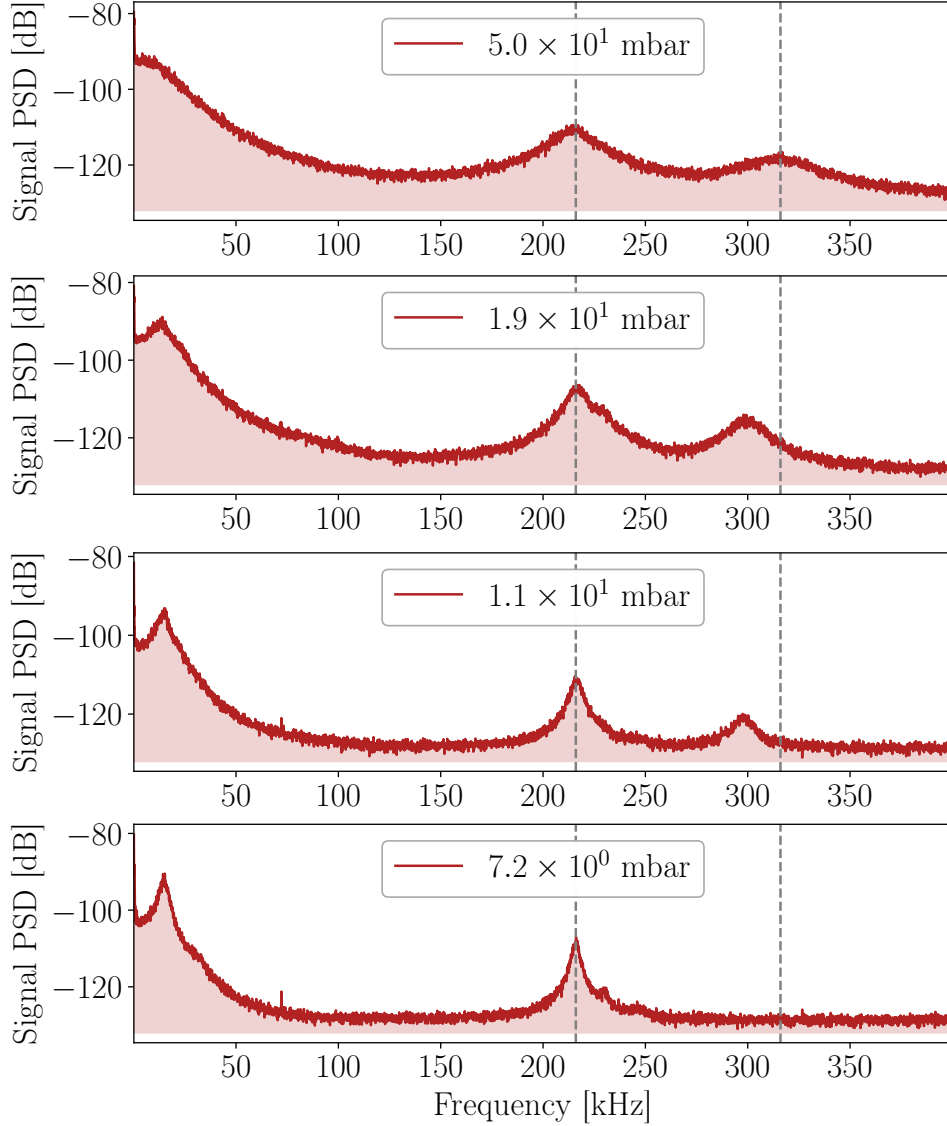


Figure 4.12: Series of signal spectrum snapshots captured using the cross-homodyne method during pump down from 50 mbar. Gray dashed lines are centred with the peaks in the first snapshot.

falls out at around 7.2 mbar. This suggests that the trapping potential in the highest region of intensity is unstable, possibly due to misalignment or distortion of the trapping beam reflection. Such misalignments may prevent from systematically bringing the particle to the centre of the spherical mirror in a future experiment. We discuss system alignment in more detail in the next section.

Let us now discuss the spectral lineshape of the signal at low pressure. Figure 4.11 shows a cross-homodyne spectrum captured at 5.2×10^{-5} mbar, and a corresponding simulated spectrum in figure 4.13. In comparison, the spectra are in good qualitative agreement aside from the peak at around 2 kHz on the experimental signal spectrum. The spectra vastly differ in the shapes of the individual peaks; the experimental peaks are not Lorentzian and the simulated lineshapes are significantly narrower. These differences arise since the statistics of the stochastic force implemented in the simulation only account for the steady-state reached under the influence of the surrounding gas. At pressures as low as 10^{-5} mbar, the particle is strongly affected by the noise and the broadening mechanisms associated with the laser, such as intensity noise. Intensity noise translates to fluctuations in the trap frequency, which broadens the spectral peaks when averaged over many cycles [112].

It is also plausible that the peaks are broadened by the presence of multiple particles in a narrow spectral range (see bottom right of figure 4.11). For the purpose of observing suppression, it is preferable to contain only one particle as other visible particles obstruct reliable detection. Presence of other particles also lends itself as an explanation for the appearance of a peak around 2 kHz. Small differences in the slow mechanical frequencies Ω_x of different particles could lead to the appearance of sidebands in the signal. In section 4.8 we present results for an experiment in which we successfully eject unwanted particles by parametric excitation.

Another possible explanation for the peak at around 2 kHz is the misalignment of the detection channel along the \hat{y} axis, a description of which is missing from our model of the detection signal. Such misalignment could give rise to first order information about the motion in the \hat{y} direction in

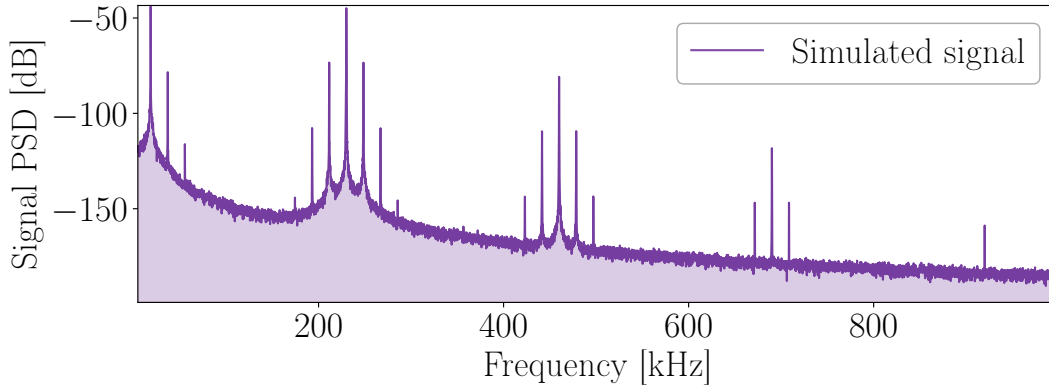


Figure 4.13: Simulated signal spectrum as described in section 4.4.3 with $\theta_d = \pi/4$, $\varphi = \pi/4$ and damping rate corresponding to 5×10^{-5} mbar and simulation time of 1.3 s. The mechanical frequencies were roughly matched to the experimental spectrum in figure 4.11 with $\Omega_x = \Omega_y = 2\pi \times 18.5$ kHz and $\Omega_z = 2\pi \times 230$ kHz.

the signal. The interference of the \hat{x} and \hat{y} motion on signal level could lead to the formation of sidebands at $\Omega_x \pm \Omega_y$. Small differences in the trap frequencies Ω_x and Ω_y occur if the beam spot transverse to the beam axis is not symmetric; this is most common in the case of strongly focused beams [37]. In our case the trapping beam is weakly focused, but it is subject to misalignment with its reflection.

4.7.2 System alignment

The constructed experiment was extremely sensitive to thermal variations and mechanical vibrations. This has implications for detection (as discussed in section 4.4.3) and trapping.

Using the percentage of total beam power reflected and coupled back into the CH1 collimator as a metric of alignment, in figure 4.14 we observed slow drift in alignment on the order of hours, which we attribute to local temperature fluctuations. Although coupled power fluctuated over a large range of around 10 %, the trap proved itself to be quite tolerant - a nanoparticle remained trapped for the duration of gathering the data in figure 4.14.

The system alignment was also highly sensitive to changes in pressure

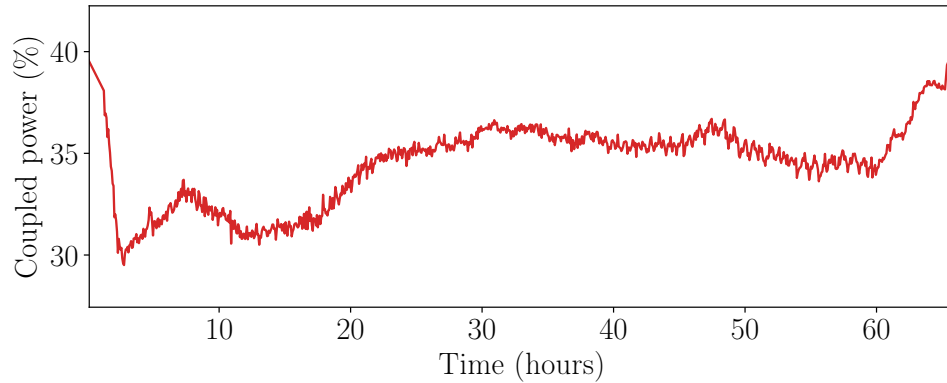


Figure 4.14: CH1 back-coupled power of the reflected beam against time.

between atmospheric pressure and about 1 mbar, as shown in figure 4.15. While this sensitivity has no real implications for trap performance once the lower pressure is reached, the system required active adjustment in beam alignment during pump down in order to ensure that the particle remains trapped.

4.7.3 Future improvements

Given the discussion in the previous sections, we identify four main aspects of the experiment which require improvement or development, necessary prior to recoil noise suppression observation:

- (i) Trap stability for reaching ultra high vacuum pressures
- (ii) Minimisation of residual intensity noise
- (iii) Positioning protocol for bringing the particle to the mirror centre
- (iv) Particle loading method

We now discuss these in order and present a plausible roadmap for recoil noise suppression observation.

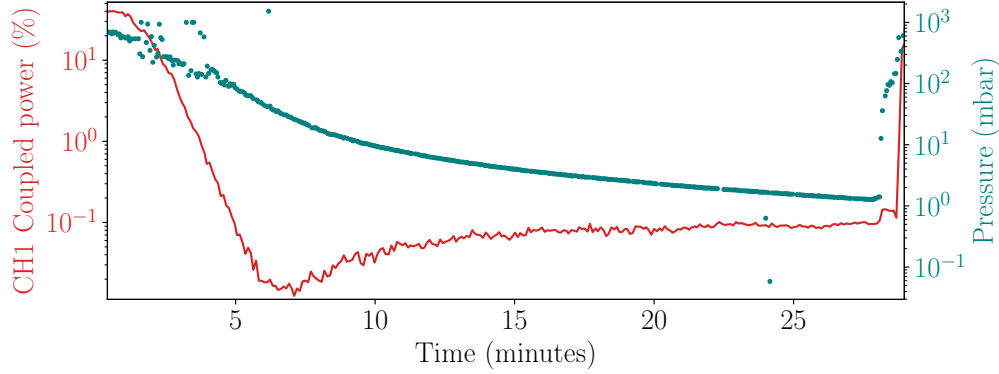


Figure 4.15: CH1 back-coupled power of the reflected beam during pump down from atmospheric pressure to about 1 mbar. At the end, the pressure was brought back to atmospheric.

- (i) In this first iteration, we were not able to reach the pressures below 6.2×10^{-6} mbar without losing the particle during pump down. Our results show that our setup is sensitive to beam misalignments, making the system susceptible to slow thermal drifts. Poor alignment could also affect trap stability at low pressures and give rise to additional mechanical noise. Further experiments will require improvements to beam alignment to ensure that the particle can be stably trapped and systematically brought to the centre of the spherical mirror. Active alignment control with electric motors or piezo drivers [113] may be required to ensure long-term stability.
- (ii) Observation of recoil noise requires minimising the effects of laser intensity noise, which is proportional to the oscillator energy and reheats the motion of the particle significantly faster. For this reason, further experiments will require the implementation of feedback cooling. With additional electronics to process the detected scatter and generate a feedback signal, our experimental setup has the components necessary to cool the motion of the particle via intensity modulation with the AOM. The optical potential in the SMART configuration may also allow

for the application of the recently developed method of ‘optical cold damping’ for reflected beam standing waves, which was used for ground state cooling [114]. The method relies on periodically modulating the phase of the trapping beam to put an imbalance between the red and blue sideband amplitudes, leading to a cooling effect.

- (iii) A particle loaded into the trap site can get confined in a standing wave maximum a long distance away from the mirror centre. Approximating the optical potential away from the centre as the same as at the focus of a Gaussian beam with a larger waist, the slow frequency of oscillation is given by $\Omega_x(z) = \Omega_x(0)w_0/w(z)$, where a similar expression holds for the fast oscillation frequency Ω_z . In this way, the frequency readout can serve as a gauge for the distance away from the focus. Using figure 4.11 as an example, ignoring possible misalignments, for our experimental parameters the above expression for the frequency suggests that the particle is located about 35 μm away from the focus.

It is possible to transfer the particle between adjacent trap sites of a standing wave by parametric amplification, as was done in previous works [115]. By exploiting our implementation of the standing wave trap, a particle can also be shifted along the beam axis by tuning the laser wavelength. For a mirror of radius $r_m = n\lambda/2$, where $n \sim 10^3$ is an integer, a shift of only $\Delta\lambda = \lambda/n$ is required to shift the standing wave pattern by $\lambda/2$. Such shifts are achievable using tunable laser sources. We can show that the shifts cause negligible deviation from the retroreflection condition by considering the optimal focus position in equation (4.4). We find that shifting the wavelength by $\Delta\lambda = (m/n)\lambda$ shifts the optimal beam focus position by,

$$\Delta z_F \approx \frac{m\lambda}{n^2\pi^2\text{NA}^4} \quad (4.10)$$

for $n > m$. For a 4 mm diameter spherical mirror, and $\text{NA} = 0.1$ we get $\Delta z_F = 6 \times 10^{-4}m\lambda$, hence in this way the standing wave pattern can be shifted by many integer steps m without affecting the modulation

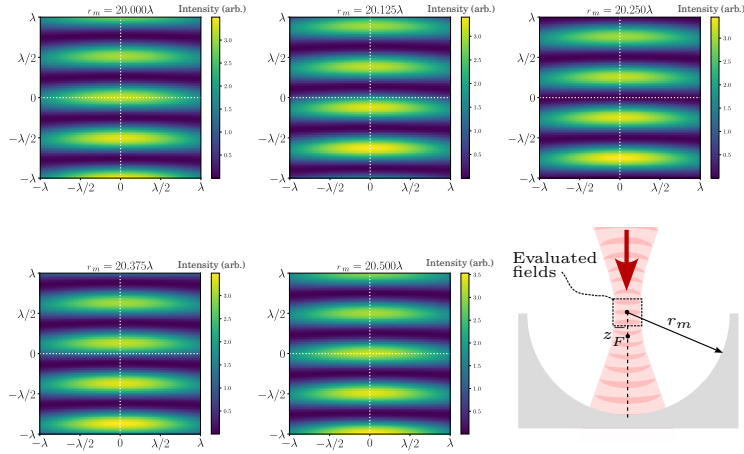


Figure 4.16: Simulated intensity profile of a Gaussian beam of $\text{NA} = 0.3$ incident upon a perfectly reflecting hemispherical mirror of radius r_m . The mirror radius was varied $20\lambda \leq r_m \leq 20.5\lambda$, keeping the point to which the Gaussian beam was focused to fixed at $z_F^- (r_m = 20\lambda)$. The simulation was performed using the software suite SCUFF-EM [116, 117] implementing the boundary element method for scattering problems.

depth of the trapping potential. To perform an additional check, we simulate the shifting intensity pattern for a small hemispherical mirror with varying radius. The results are shown in figure 4.16. Note the unchanging colour scale of the intensity profile as the radius is varied. As discussed at the beginning of this chapter, it is a unique feature of the SMART geometry, that the suppression condition coincides with an appearance of intensity maximum of the standing wave at the centre of the spherical mirror. Because of this, the detected spectrum provides sufficient information needed to determine whether the particle is shifted to the mirror centre. In a well aligned SMART setup, the mechanical frequency of the particle approaching the mirror centre should increase, and in close proximity to the centre, the first-order peak of mechanical motion should vanish. It can therefore be verified whether the particle has reached the mirror centre by systematic observation of the disappearance of the first order peak in the detected signal spectrum.

- (iv) Optical suppression of the detected scatter is insufficient to determine whether the motion of the particle was affected. To confirm whether the spherical mirror is affecting recoil noise, reheating trajectories of a particle cooled below the temperature of the thermal bath need be measured over many experimental runs as was done in [38]. Such a protocol requires a robust method for loading the particle, preferably at low pressures in case the particle escapes. The nebuliser method used in our experiment is only applicable at atmospheric pressures and introduces many particles which is undesirable. It would be beneficial for a future experiment to use one of the other popular methods of particle loading, such as using a piezoelectric element inside the vacuum chamber [113,118] or the LIAD method [119, 120].

4.8 Particle ejection by parametric excitation

In order to rule out the presence of additional unwanted particles, we attempted to eject them by intensity modulating at twice the trap frequency $2\Omega_x$. We modulated the intensity with a depth of a few percent. The frequency of modulation was slowly ramped down during the ejection attempt, to follow the decreasing trap frequency of a particle with an excited amplitude. A result of this procedure is shown in figure 4.17. The figure shows a clear change in the spectrum after the frequency ramp down, around both the slow oscillation frequencies, but also fast oscillations around 270 kHz which were unaffected by the modulation. The spectrum lineshape remains complicated after excitation suggesting that several particles may have been present after ejection. In a future experiment, multiple frequency sweeps may be required to eliminate all but a single particle.

4.9 Residual backaction noise in SMART

The case of a *large, perfectly-reflecting hemi-sphere* corresponds to three approximations which hide additional heating - large mirror radius

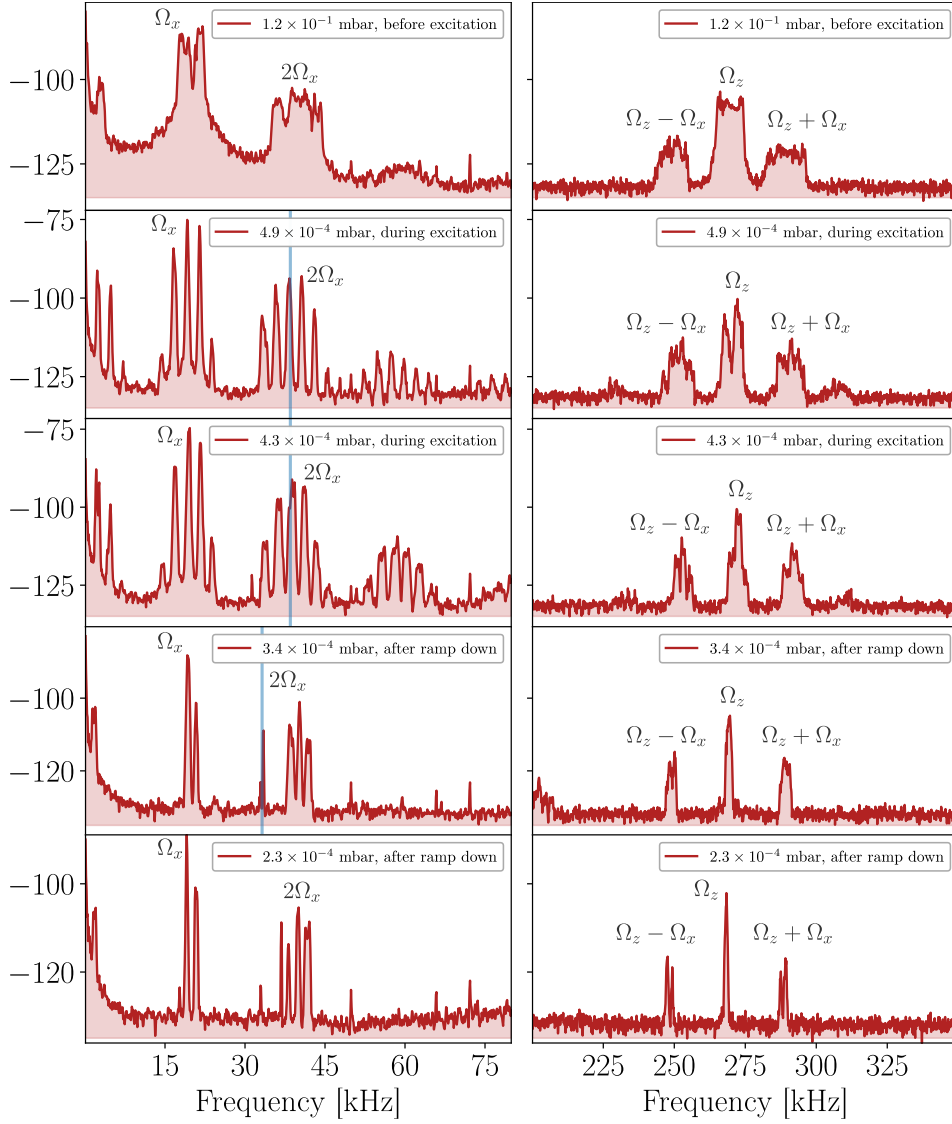


Figure 4.17: Series of signal spectrum snapshots demonstrating the result of parametric excitation procedure. The blue lines denote the modulation frequency during the snapshot. The modulation frequency was slowly ramped down from 38 kHz to 33 kHz at $\sim 10^{-4}$ mbar pressure.

$r_m \gg \lambda, |\mathbf{r}_0|$, mirror reflectivity $\rho = -1$ and mirror spanning angle $\theta_m = \pi/2$, respectively. The final result in (3.41) depends linearly on the mirror reflectivity. While mirrors of state of the art metallic mirror reflectivities of $\text{Re}[\rho] \approx 0.99$ are available, perfect reflection is not possible, which immediately constrains the minimum achievable backaction noise level to 10^{-2} of its free-space value.

Dipole emission of a particle located at the centre of a spherical mirror is retro-reflected. This is not the case when the particle is displaced from the centre. However, assuming a large mirror radius allows us to make the retro-reflection approximation of the dipole scatter, which corresponds to neglecting the change in the direction of the wavevector direction of the reflected scatter. To first order, this amounts to neglecting electric field terms proportional to $|\mathbf{r}_0|/r_m$. We can assume that these neglected field terms lead to additional heating to place limits on the achievable suppression level. Since $|\mathbf{r}_0| \lesssim \lambda$, so long as the mirror has a radius of $r_m \gtrsim 1$ mm, the additional backaction heating due to non-retro-reflected scatter is constrained to $\sim 10^{-3}$ of its free-space value.

A smaller spanning angle of the mirror $\theta_m < \pi/2$ leads to additional heating as shown in figure 3.5. For the SMART arrangement, it is possible to utilise a full hemisphere for trapping, hence we can assume that θ_m is not a limitation.⁶

As briefly discussed in the previous chapter, the particle interacts with an infinite series of reflection fields of its own scatter from the mirror. In the preceding calculations, we have fully neglected the influence of these reflected dipole fields on backaction noise. A simple estimate might lead one to believe that the scattered fields have a negligible effect on heating; the reflected scatter which returns to influence the particle has the form $|\mathbf{E}_s| \sim k^3 |\mathbf{p}| = k^3 \alpha |\mathbf{E}_0|$ and is smaller than the trapping field in magnitude by a factor of $k^3 \alpha \sim (r_p/\lambda)^3$. For a particle of radius $r_p = 0.1\lambda$ we could therefore expect the scattered fields to contribute a factor of 10^{-6} in additional heating, since backaction noise spectral density scales quadratically with the field. However, the reflected scatter has an additional effect - it exerts an additional optical force on the

⁶This is not the case for the fibre trap arrangement SWIFT, which we discuss in the next chapter.

particle which can shift the equilibrium position away from the mirror centre. Not only is suppression less effective away from the mirror centre, but the particle can be shifted to a point of non-zero field gradient, which increases backaction noise further. In the next section we numerically analyse this effect.

4.9.1 Influence of the SIBA force on trapping

Suppression of backaction in a counter-propagating beam trap, which was computed in section 3.3, relies on the vanishing of the trapping field gradient to first order about the centre of the spherical mirror. This point should coincide with the particle's equilibrium position, however, this may not be the case if the reflected scatter exerts a force which significantly shifts the equilibrium position of the particle. This is known as the self-induced backaction (SIBA). It has been shown experimentally that SIBA can play an active role in trapping near resonant structures [121] by shifting the resonant frequency of the structure as the particle moves [122]. In this section we analyse this SIBA force for a particle trapped near the centre of a spherical mirror, with various beam and particle parameters. We find that SIBA only has a strong influence on trapping of large Rayleigh particles along directions of weak confinement by the trapping beams. For appropriately chosen beam and particle parameters, SIBA provides a negligible contribution to trapping and does not shift the equilibrium position.

We follow the treatment presented in [98], which accounts for the influence of the environment on the particle by defining an effective polarisability which is a tensor quantity that varies at each point in space,

$$\bar{\alpha}_{\text{eff}}(\mathbf{r}_0) = \left(\bar{\mathbf{I}} - \alpha_0 \frac{k_0^2}{\epsilon_0} \left[\frac{1}{6\pi} \bar{\mathbf{I}} - \bar{\mathbf{G}}_s(\mathbf{r}_0, \mathbf{r}_0) \right] \right)^{-1} \alpha_0. \quad (4.11)$$

This expression follows when the first-order scattering part of the self-consistent field which the particle interacts with is absorbed into the definition of the polarisability. Assuming harmonic time dependence throughout, the complex amplitude of the dipole moment is then given by,

$$\mathbf{p} = \bar{\alpha}_{\text{eff}} \mathbf{E}_0. \quad (4.12)$$

The time-averaged force which acts on the particle is then given by equation (2.25) where the field \mathbf{E} is the sum of the trapping field and reflected dipole field at the position of the particle. Accounting for the dipole emission reflected back onto the particle by the mirror to first order, this field reads,

$$\mathbf{E} = \mathbf{E}_0(\mathbf{r}_0) + \frac{k_0^2}{\epsilon_0} \overline{\overline{\mathbf{G}}}_s(\mathbf{r}_0, \mathbf{r}_0) \cdot \mathbf{p} \quad (4.13)$$

To find the effect of the scatter reflection from the spherical mirror has on the trapping forces, we compute (2.25) with (2.9) with a particular focus on a trapping configuration of a standing wave along the mirror axis ($\hat{\mathbf{z}}$).

Throughout this numerical study we model the trapping beams as Gaussian beams with $\lambda = 1550$ nm of $\text{NA} = 0.3$. Each beam carries a power of 500 mW and has a waist w_0 . We assume that the mirror spans $\text{NA}_m = 0.9$ ($\theta_m = 64.2^\circ$ in figure 2.1), it is perfectly reflecting with radius constrained to $k_0 r_m = n\pi$ and is oriented as shown in figure 2.1. We did not restrict the calculation to small displacements, computing $\overline{\overline{\mathbf{G}}}_s$ numerically on a square grid of side length 2λ . The considered particle is a silica nanosphere with $\rho = 2300$ kg/m³.

Comparison of figure 4.18 with 4.19 reveals that SIBA has a pronounced effect when the confinement along a direction is relatively weak, due to a shallow field gradient.

The effect is always stronger along the mirror axis. This is evident when counter-propagating beam traps in figures 4.18 and 4.19 are compared; the F_z force curve is significantly distorted and the point about which the force component F_z changes direction in the $\hat{\mathbf{y}}$ standing wave of figure 4.18 shifts from the origin by about 75 nm away from the mirror surface along $\hat{\mathbf{z}}$. On the other hand, no such shifts are visible in the F_x and F_y of the $\hat{\mathbf{z}}$ standing wave of figure 4.19. Instead a small shift is visible for F_z . Note that relatively large Rayleigh particles were considered in this numerical study of the standing wave traps ($r_p = 150$ nm). This is because, in a counter-propagating beam trap the scattering force along the propagation direction of the beams does not contribute, and one might want to choose larger particles for trapping. However, SIBA provides an additional pushing force along the mirror axis, which is stronger for larger particles. Indeed, the position shifts become

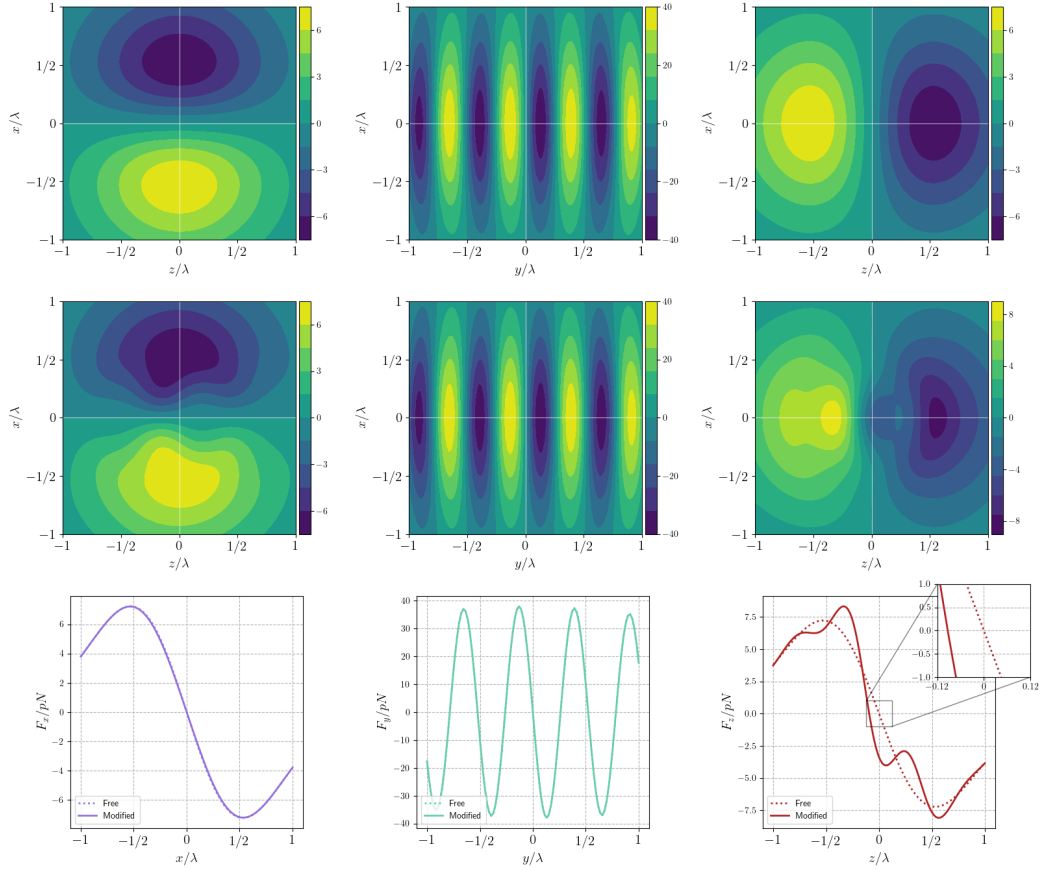


Figure 4.18: Trapping forces acting on a silica nanosphere of radius $r_p = 150$ nm in a two counter-propagating Gaussian beams propagating along \hat{y} . The beams are in-phase at the origin. **Top:** F_x , F_y and F_z components of the trapping force (pN) in free space **Middle:** F_x , F_y and F_z components of the trapping force (pN) including the effect of the spherical mirror **Bottom:** Slice of the contour plots for F_x , F_y and F_z . The inset figure for F_z shows the shift of the equilibrium position.

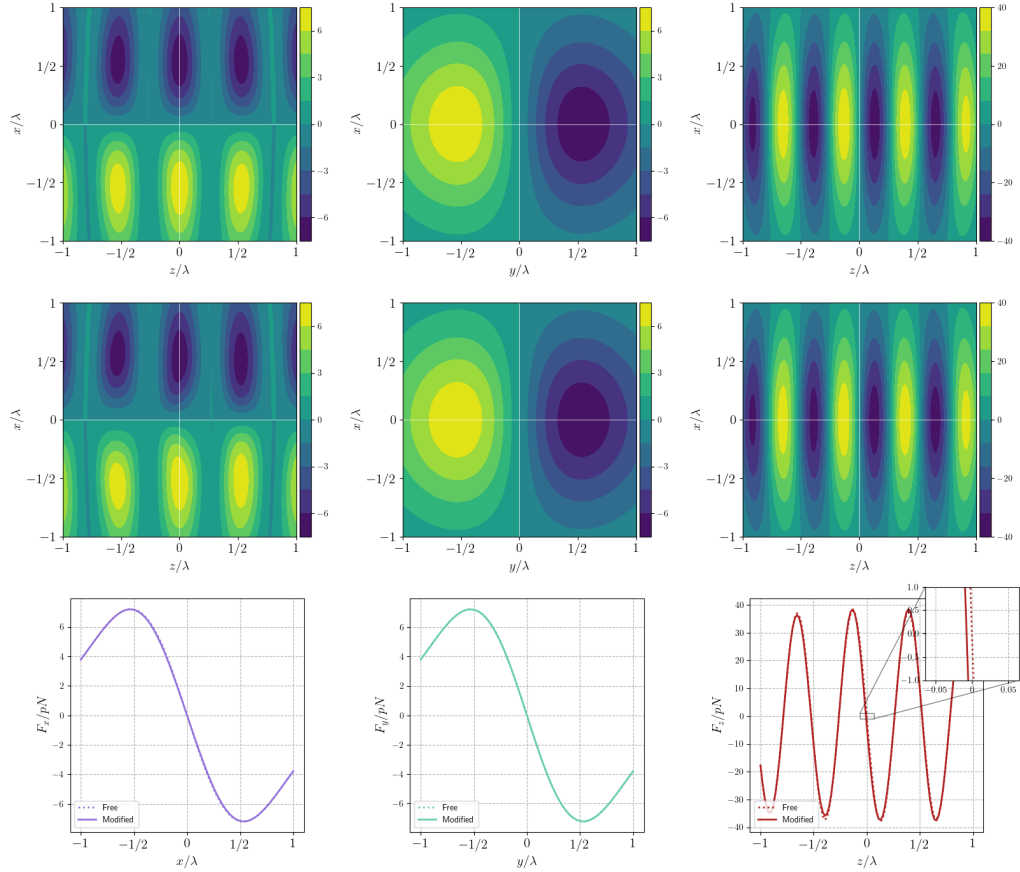


Figure 4.19: Trapping forces acting on a silica nanosphere of radius $r_p = 150$ nm in a two counter-propagating Gaussian beams propagating along \hat{z} . The beams are in-phase at the origin. **Top:** F_x , F_y and F_z components of the trapping force (pN) in free space **Middle:** F_x , F_y and F_z components of the trapping force (pN) including the effect of the spherical mirror **Bottom:** Slice of the contour plots for F_x , F_y and F_z . The inset figure for F_z shows the shift of the equilibrium position.

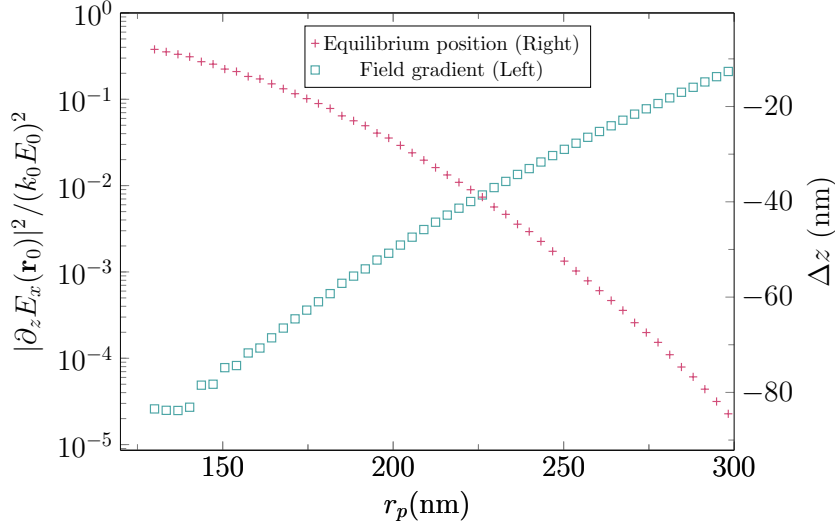


Figure 4.20: Equilibrium position shift Δz and field gradient $|\partial_z \tilde{E}(\mathbf{r}_0)|^2 / (k_0 E_0)^2$ against particle radius r_p . Results are independent of laser power. As a reference for the scale on the y-axis, we note that at the focus of a weakly-focused Gaussian beam $|\partial_z \tilde{E}_x(\mathbf{r}_0)|^2 \approx (k E_0)^2$.

negligible for particles of radius $r_p = 100$ nm. Therefore, if focusing as strong as $\text{NA} = 0.3$ is not available (as would be the case in the proposed SWIFT configuration, see next chapter), one can always ensure that SIBA does not have a significant contribution to trapping by choosing smaller particles.

In the previous chapter, the calculation of backaction noise relies on the vanishing field gradient of the trapping laser. This rests on the assumption that in a standing wave, the scattering force cancels out and the particle's equilibrium position is located at the point of zero-gradient. Although the shifts in equilibrium position for a \hat{z} standing wave are small, we nonetheless compute the gradient at the particle's new equilibrium position to test the validity of this approximation. At the condition $k_0 r_m = n\pi$, $\text{Im}[G_{xx}]$ is twice as large as in free space for a full hemisphere (cf. equation (3.29)). Therefore, a non-vanishing field gradient along the \hat{z} axis gives rise to noise $S_{zz}^F = (\hbar k_0 P_0 / \pi c) (|\partial_z \tilde{E}(\mathbf{r}_0)|^2 / (k_0 E_0)^2)$ where $\tilde{E}(\mathbf{r}_0)$ is the electric field \hat{x} component, evaluated at the position of the particle with the inclusion of the

SIBA correction and E_0 is the trapping field amplitude. In figure 4.20 we plot the equilibrium position shift (here denoted Δz) along the mirror axis and $|\partial_z \tilde{E}(\mathbf{r}_0)|^2 / (k_0 E_0)^2$ against particle radius. Figure 4.20 shows that for radii $r < 200$ nm, the residual field gradient is likely not to be the limiting factor for the suppression of backaction noise when compared to other experimental limitations.

Chapter 5

SWIFT: Standing wave interference fibre trap

The coincidence of the backaction suppression condition on the mirror radius with the location of the trap maximum is a convenient feature of the hemisphere reflection trap. However, this coupling of the trap position to mirror radius is a hindrance on the design of experimental protocols, since the particle has to be shifted from the mirror centre to be efficiently probed. In this chapter, we analyse and document the design process of an alternative fibre-based trap configuration. Here the trapping potential is generated by cleaved optical fibres emitting lasers, independent of the mirror surface, meaning that the mirror radius and the trap position are decoupled.

5.1 Trap description

The setup is shown in figure 5.1. In contrast to standard arrangements in levitated optomechanics, the trapping potential is formed by cleaved, single-mode (SMF-28) fibres radiating $\lambda = 1550$ nm laser light, separated a distance ~ 100 μm . Light leaving a cleaved SMF-28 fibre is well approximated by a Gaussian beam with its waist $w_0 = 5.2$ μm (referred to as the mode field

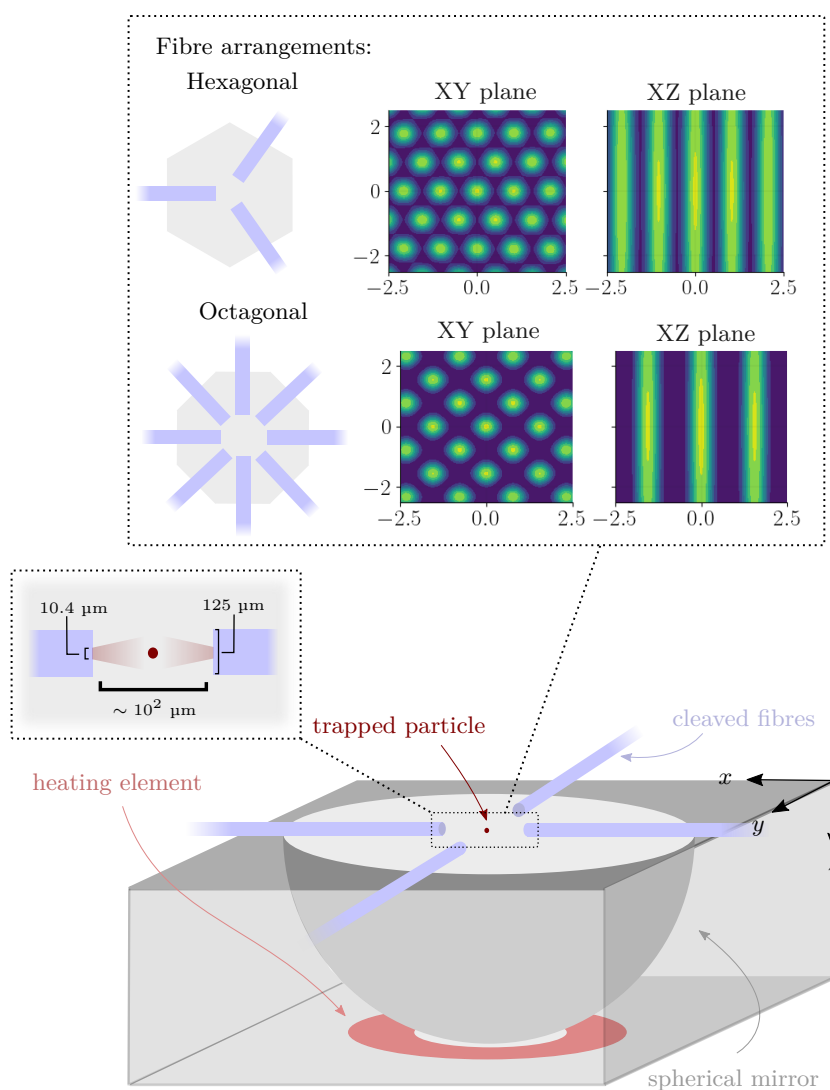


Figure 5.1: Standing wave interference fibre trap (SWIFT). The particle is trapped at the centre of a spherical mirror in an optical lattice formed by light propagating out of optical fibre endfaces. A heating element is used to stabilise mirror temperature, independently of trap position. In the octagonal arrangement, 4 orthogonal fibres are used for trapping with the other 4 used for pick-up of particle scatter. In the hexagonal arrangement, the 3 fibres are used for both trapping and pick-up of scatter. The figure also shows intensity profiles around the centre point of the hexagonal arrangement (top) and the octagonal arrangement (bottom) in the xy and xz planes relative to the coordinate system shown. For the octagonal arrangement, four orthogonal fibres are used for trapping, while the other fibres at 45° are used for pick-up of particle scatter.

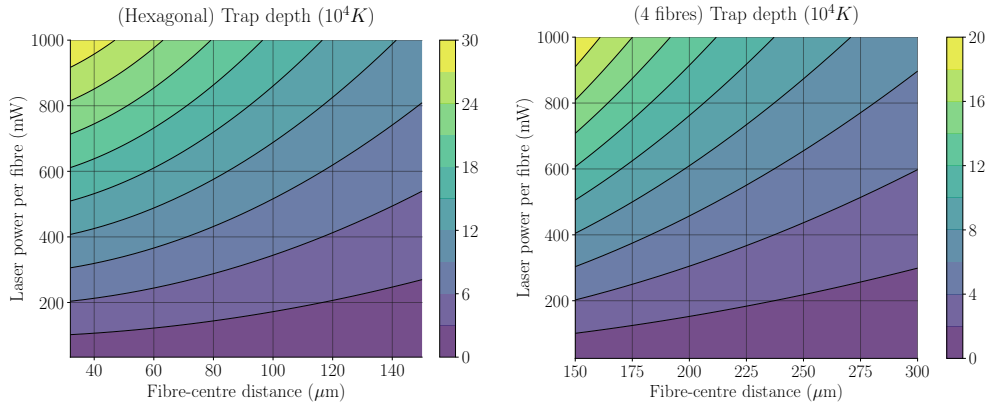


Figure 5.2: Trap depth for laser power per fibre and fibre-centre distance in the hexagonal (left, 3 trapping fibres) and octagonal (right, 4 trapping fibres) fibre arrangements, for a silica particle with radius 150 nm. Note the different distance ranges on the x -axis, which were chosen based on the geometrical limits of the two different configurations.

radius) located at the fibre endface [123]. Throughout this chapter, we will consider the trapping fields radiating from the fibres to be polarised in the same direction, along the symmetry axis of the mirror. Since the beams propagate in a common plane, this results in maximum interference and therefore better modulation of the optical lattice. In both the hexagonal and octagonal fibre arrangements, the fibres generate a cigar-shaped optical lattice profile depicted in figure 5.1. The phases of the trapping beams can be addressed individually, giving the freedom to shift the trapping position with the particle in the xy plane, independent of the mirror radius. Having this degree of control over the trap position in the SWIFT fibre arrangement, also permits direct feedback cooling by phase-modulation in the xy plane, in contrast to the commonly implemented parametric feedback cooling [37]. Such linear feedback is usually implemented using electrostatic forces and is referred to as cold damping [124–126]. The scattering force has a negligible impact near the trap centre for a well aligned configuration. To verify this, we simulate particle dynamics using a Langevin equation driven by a stochastic force corresponding to a thermal bath at atmospheric pressure and the full optical force from equation (2.25). The results are shown in figure 5.4. Note that the particle always ends up near

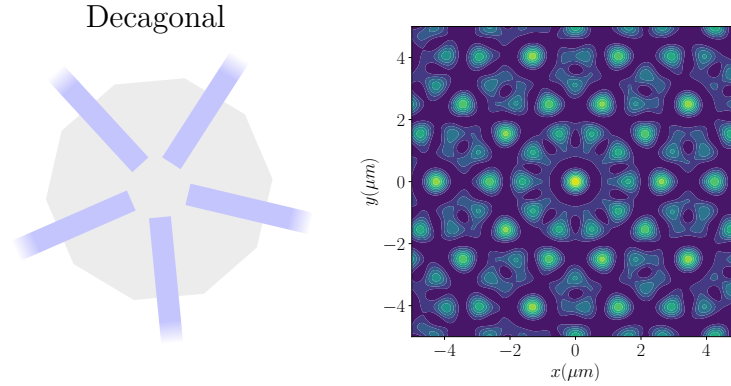


Figure 5.3: An xy intensity profile (right) generated in a decagonal arrangement with a 5-fold symmetry of the fibres (left).

centre of each trap site. Ignoring the impact of the scattering force, the optical force is conservative and we can estimate the trappability with the trap depth of the corresponding optical potential,

$$U = -\frac{\alpha}{4}I(x, y, z) \quad (5.1)$$

where I and α are the total field intensity and free-space particle polarisability respectively. Since the trapping potential is proportional to the intensity at the particle position, in a trap configuration consisting of total laser power P split among N fibres emitting laser fields that constructively interfere at the trap centre we have $U \propto |\sum_i^N E_i|^2 \propto NP$. Although the trap depth scales linearly with the number of trapping fibres, the geometry of the arrangement also plays a role (see figure 5.2); In general it is always possible to bring fibres closer in the hexagonal arrangement since fewer fibres are needed. Fibres stripped of their buffer have a diameter of $125 \mu\text{m}$. With each fibre equidistant from the centre point, this gives a minimum distance of about $30 \mu\text{m}$ and $150 \mu\text{m}$ for the hexagonal and octagonal arrangements respectively. The result is that at the minimum separation of fibres for each configuration, the hexagonal arrangement can reach higher trap depths even when more net optical power is supplied in the octagonal arrangement. We note that not all

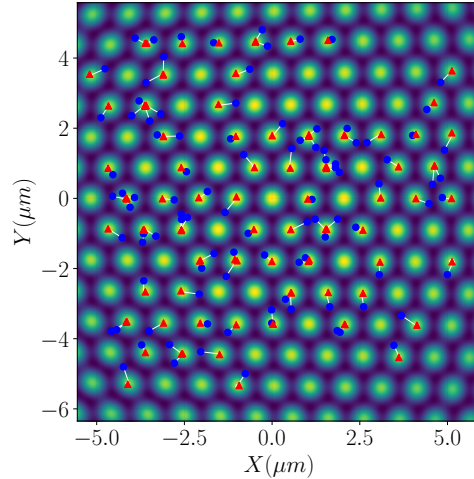


Figure 5.4: Testing the influence of the scattering force in the hexagonal arrangement. 100 particle trajectories from a 3d simulation of the Langevin equation which describes particle dynamics. Particles are initialised at a random position in a $(5 \mu\text{m})^3$ cube (blue circles). The red triangles show the final position of the particles 500 ms later.

two-dimensional fibre arrangements produce a lattice such as those discussed above. For example, decagonal configuration with 5-fold symmetry of the fibres generates a central maximum but not a regular lattice (see figure 5.3). We do not consider such an arrangement in this work, but it may be useful for other applications.

The intensity profiles for the arrangements shown in figure 5.1 suggest that the particle can only be weakly confined by the SWIFT arrangement along the mirror axis relative to the xy lattice plane. Because of this, there is a discrepancy between trap frequencies in the xy plane (fast axes, denoted \perp) and along the mirror (slow, denoted \parallel) axis; estimating the spring constant with $k_i = m\Omega_i^2 \approx -\partial_i^2 U$, allows us to estimate the trap frequencies. For typical parameters we get $\Omega_{\perp}/2\pi = 50$ kHz and $\Omega_{\parallel}/2\pi = 1$ kHz.

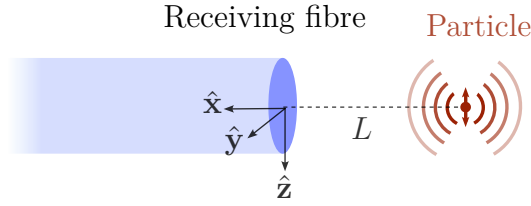


Figure 5.5: Particle scatter fibre coupling calculation diagram

5.2 Scatter collection efficiency

The fibres in the SWIFT configuration are used for both trapping and particle position detection. This is possible because laser light polarised along mirror axis, scattered by the particle can be efficiently coupled into the fibres. In general, not all light incident upon a fibre endface couples to the single mode which the fibre carries. We can compute how much power from particle scatter is coupled into the fibre, using the standard techniques for step-index fibres under the weak-guidance approximation [127], which assumes that the difference in the refractive index between the 125 μm cladding and the 8.2 μm diameter core is small. To simplify the calculation we also assume that the particle is located some distance $L \gg \lambda$ along the central axis orthogonal to a fibre endface (see figure 5.5)¹. Assuming harmonic time dependence throughout, the total transmitted electric field on the fibre endface is split into two orthogonal terms,

$$\mathbf{E}_{\text{tot}} = a_0 \mathbf{e}_0 + \mathbf{E}_{\text{rad}} \quad (5.2)$$

where \mathbf{E}_{rad} is the radiation field which does not couple into the fibre and \mathbf{e}_0 is the normalised electric field of the fundamental mode which remains guided in the fibre with amplitude a_0 . This fundamental mode has a transverse profile given by a Bessel function [128] which is well approximated by a Gaussian beam profile of waist 5.2 μm located at the fibre endface [129]. The coupling

¹Since we are assuming L to be large, the result will remain approximately valid for a particle displaced from the central axis by $\sim \lambda$.

amplitude is given by, [127]

$$a_0 = \frac{1}{2N_0} \int (\mathbf{e}_0 \times \mathbf{H}_{\text{tot}}^*) \cdot \hat{\mathbf{x}} \, dA = \frac{1}{2N_0} \int (\mathbf{h}_0 \times \mathbf{E}_{\text{tot}}^*) \cdot \hat{\mathbf{x}} \, dA \quad (5.3)$$

where \mathbf{h}_0 is the magnetic field corresponding to the fundamental mode, fields \mathbf{E}_{tot} and \mathbf{H}_{tot} denote transmitted fields on the fibre end-face, and the normalisation factor,

$$N_0 = \frac{1}{2} \int (\mathbf{e}_0 \times \mathbf{h}_0^*) \cdot \hat{\mathbf{x}} \, dA = \frac{n\pi w_0^2}{2c\epsilon_0} \quad (5.4)$$

The integration runs over the infinite plane orthogonal to the unit vector $\hat{\mathbf{x}}$ which we truncate to only contain the fibre endface. The coupled power is then obtained from $P = a_0 N_0^2$. The calculation is therefore reduced to finding the transmitted fields on the fibre endface.

We find the transmitted dipole emission fields by decomposing it into s- and p- polarisation components and using the Fresnel coefficients, [13]

$$\begin{aligned} t_s &= \frac{2k_1^x}{k_1^x + k_2^x}, & k_1^x &= \sqrt{k^2 - k_y^2 - k_z^2} \\ t_p &= \frac{2nk_1^x}{n^2k_1^x + k_2^x}, & k_2^x &= \sqrt{n^2k^2 - k_y^2 - k_z^2} \end{aligned} \quad (5.5)$$

where k_1^x and k_2^x are the wavevector components of the dipole emission in medium 1 (assumed vacuum) and the medium 2 (glass fibre) respectively. Here we are assuming that the fibre has a uniform refractive index $n = 1.4682$ [130]. For large L only dipole far-fields reach the fibre endface. This simplifies the calculation because far-fields have a wavevector pointing radially away from the particle location. Using (5.5) with dipole far-fields and substituting into (5.3) we find the result for the coupling amplitude,

$$a_0(L) = \frac{nk^2\pi|\mathbf{p}_0|}{8c\epsilon_0^2N_0} \int t_s(\rho, L) \frac{e^{ik\sqrt{\rho^2+L^2}}}{(\rho^2+L^2)^{3/2}} e^{-\rho^2/2w_0^2} (\rho^2+2L^2)\rho \, d\rho \quad (5.6)$$

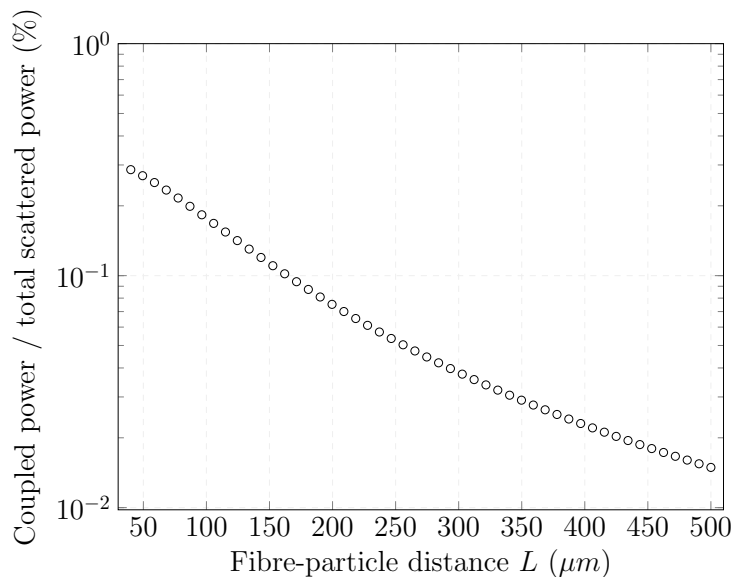


Figure 5.6: Particle scatter coupled into a fibre, normalised to the total scattered power in the hexagonal configuration. The plot accounts for increasing trap depth with decreasing distance L .

where $|\mathbf{p}_0|$ is the dipole moment amplitude, $\rho = \sqrt{y^2 + z^2}$ and,

$$t_s(\rho, L) = 2 \left(1 + \sqrt{1 + \frac{\rho^2}{L^2} \left[n^2 - \frac{\rho^2}{\sqrt{\rho^2 + L^2}} \right]} \right)^{-1} \quad (5.7)$$

Throughout this section, we have assumed that the particle is polarised along mirror axis $\hat{\mathbf{z}}$. In figure 5.6 we plot the scattered power of dipole emission coupled into a fibre, accounting for the increasing trap depth with decreasing distance L . We find that at distance of about 150 μm , 0.1 % of scattered power couples into a single fibre. In the hexagonal arrangement, when detecting on all three fibres, this is approximately equivalent to a collection efficiency from particle at the focus of a lens with $\text{NA} = 0.1$.

In the octagonal arrangement, the trapping fibres cannot be used for pick-up of particle scatter because light coupled across from the opposing trapping fibres swamps the signal. Because of this, in the octagonal arrangement additional pick-up fibres are needed at 45° . These pick-up fibres receive a

clean particle signal with no interference from the trapping fibres, due to the weak divergence of the trapping beams and highly inefficient coupling to an angled fibre. The same is true for the hexagonal arrangement, but in addition there is no cross-talk between trapping fibres and therefore they can be used for both trapping and detection. The glass-air interface of the fibre endfaces reflects back about 4 % of incident power. This small percentage can be used as a reference field for homodyne detection.

5.3 Particle position detection

In an interferometric measurement, displacement in the xy (denoted x_{\perp}) plane generates linear changes in the optical path to the fibre endfaces. Because of this, the fibres detect a signal proportional to the phase change due to displacement along the fibre axis kx_{\perp} . On the other hand, the fibres can only detect second-order displacement along the mirror axis, with the signal proportional to $\Delta\phi = k\sqrt{L^2 + z^2} - kL \approx kz^2/(2L)$. However, since the particle is weakly confined along the mirror axis, its displacement is large; using equipartition theorem $k_B T = m\Omega_i^2 \langle x_i^2 \rangle$ and the earlier estimates of trap frequencies for typical trap parameters we find $(x_{\perp})_{\text{rms}} \approx 35 \text{ nm}$ and $(z)_{\text{rms}} \approx 2 \text{ }\mu\text{m}$. For these values, assuming that the fibre is at a distance $L = 100 \text{ }\mu\text{m}$, displacements in the xy plane and along the mirror axis generate comparable phase modulations of $k(x_{\perp})_{\text{rms}} = 0.12$ and $k(z)_{\text{rms}}^2/L = 0.16$.

Using the hexagonal trap and specifications of our photodetector as an example, we can estimate the signal to noise ratio in a position detection experiment. Assuming that each fibre carries 250 mW of laser power and is separated by 150 μm from the trap centre point, we can numerically compute that a 150 nm radius particle would scatter a total power of about 50 μW . As mentioned in the previous section, at 150 μm each fibre collects 0.1 % of total scattered power at this separation, or 0.05 μW in this case. The interferometric signal power scales as $\sim \phi_{\text{mod}} \sqrt{P_{\text{col}} P_{\text{ref}}}$ where ϕ_{mod} , P_{col} and P_{ref} denote signal phase modulation, collected power and reference power respectively. If the fibre back-reflection is used as the interferometric reference, the reference

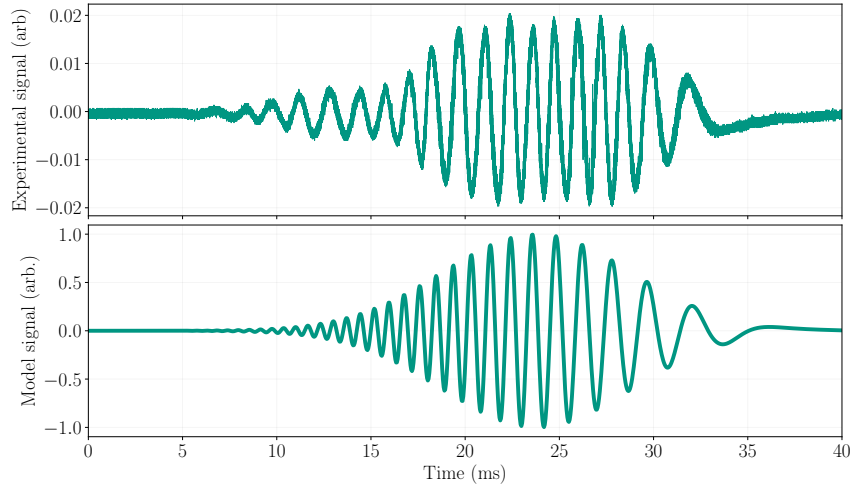


Figure 5.7: (Top): Experimental time-trace of the particle passing through the observable region in the trap (Bottom): Signal reproducing the lineshape above based on the dependence in equation (5.8).

power is equal to about 10 mW, which corresponds to 4 % of the 250 mW laser power incident upon the fibre endface. With the estimates of phase modulation discussed in the previous paragraph, this gives a signal amplitude of about 3.4 μ W. Considering our balanced photodetector PDB440C from Thorlabs which has a noise-equivalent power of 3.9 pW/ $\sqrt{\text{Hz}}$, the motion in three dimensions should be detectable solely using fibres for detection. A benefit and a potential drawback of this detection method is, however, that particles only very near or at the central maximum can be detected. If a particle gets trapped at an optical lattice site several wavelengths away from mirror the centre, the fibres would not capture its motion.

In trapping attempts, particles were introduced using the nebuliser method from above the SWIFT mount. The particles did not stay trapped, and instead would only briefly pass by through the observable region, appearing as short blips on the signal time-trace (see figure 5.7). The lineshape of these events is reproduced by a simple model of the interferometric signal, in which the particle moves at a constant velocity through the central region along the z

axis and probing regions of changing intensity,

$$V(t) \propto \cos\left(\frac{k(vt)^2}{2L}\right) \exp\left(-\frac{(z_0 + vt)^2}{w(L)^2}\right) \quad (5.8)$$

where z_0 is the initial particle height along the mirror axis, v is particle velocity along z , L is the distance to the fibre and $w(L)$ is the beam waist. An example of a captured time trace and its model is shown in figure 5.7.

5.4 Challenges and limitations

Decoupling of the optical potential from the mirror radius makes SWIFT an attractive avenue for studying the backaction suppression effect. The optical potential itself may prove to be versatile for other applications due to its ability to freely translate the trap sites in the lattice plane, and prospects for cooling by phase modulation. When fully functional, SWIFT could operate as a stand-alone device with trapping and detection fibre ports and without the need for maintaining fibre alignment. However, as of the end of this project, SWIFT is still in development and several potential limitations to stable trapping still need to be investigated. In this section we discuss some of the experimental challenges considered in the development of the SWIFT configuration. We also discuss limitations in the application of this fibre trap for the demonstration of backaction suppression, in comparison to the hemisphere reflection standing wave trap. The work on SWIFT is ongoing, and improvements discussed in this section will be implemented in future experiments.

5.4.1 Fibre alignment

The SWIFT configuration crucially relies on precise alignment of the fibres to a common point for trapping and detection. Misalignment of fibres can yield an unstable trapping potential poor detection of particle scatter or detection of a region in space too far from the centre of the spherical mirror.

A good alignment can always be achieved by mounting fibres on translation stages, however since at least three fibres have to be aligned for the SWIFT

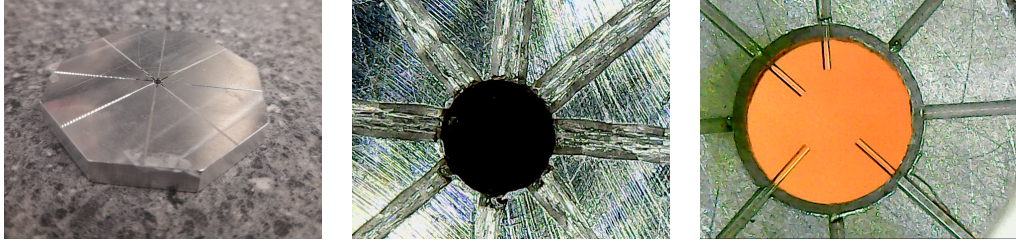


Figure 5.8: (Left) First iteration of the SWIFT mount - v-grooves drilled into a slab of aluminium using a corner of a flat end mill. (Middle) Microscope image of the v-grooves. The surface is visibly rough. (Right) Microscope image of the mount with fibres in place.

configuration, such an implementation is expensive and spatially inefficient. Because of these limitations, we aimed at designing a solid-state mount with aligned grooves to which the fibres can be fixed. Such an implementation of the SWIFT configuration could operate as a stand-alone device with small dimensions and without the need for fibre realignment. During the course of the project, several iterations of the SWIFT configuration were developed, each one aiming to improve fibre alignment (see figures 5.8, 5.10 and the yet untested iteration shown in 5.11). Starting from the second iteration 5.10, the mounts were developed in collaboration with the Southampton Planar Optical Materials Research Group which specialises in the design and fabrication of photonic devices [131, 132].

Alignment was assessed by coupling laser light across a variable gap between opposing fibres. For opposing fibres, the general shape of the curve of coupled power with varying gap size can be assessed using the simple overlap integral, [127]

$$\eta = \frac{|\int e_0 E_0^*(L) dA|^2}{\int |e_0|^2 dA \int |E_0(L)|^2 dA} \quad (5.9)$$

where η is the fraction of total power that gets coupled into the receiving fibre, $e_0 = \exp(-\rho^2/w_0)$ is the electric field mode amplitude and E_0 is the amplitude of the incident field. When the incident field profile is that of an aligned Gaussian beam with its waist a distance L away, then $E_0 =$

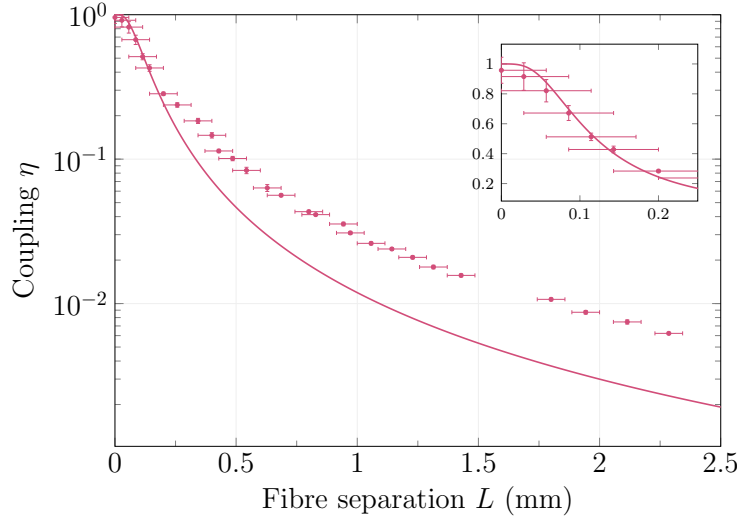


Figure 5.9: Fraction of total radiated power coupled into an opposing fibre separated by a distance L , measured on fibres clamped to the silicon mount. The solid line corresponds to equation (5.10) evaluated at $w_0 = 5.2 \mu\text{m}$.

$(w_0/w(L)) \exp(-\rho^2/w(L)^2)$ and,

$$\eta = 4z_R^2 \frac{L^2 + z_R^2}{(L^2 + 2z_R^2)^2} \quad (5.10)$$

The results of coupling measurements of fibres clamped to the silicon mount are shown in figure 5.9, which shows good agreement of the overlap integral with the data for separations smaller than $250 \mu\text{m}$. The discrepancy is likely due to stray reflections coupling to the receiving fibre at large separations.

5.4.2 Trapping light reflection interference

It is not possible to implement the SWIFT configuration with a full *unaltered* hemispherical mirror. This is simply because the fibre axes can never be aligned in parallel with one another and with the centre of the mirror without obstructing its surface. Any reduction in the mirror surface area would render the suppression effect less effective. For maximum retention of the mirror

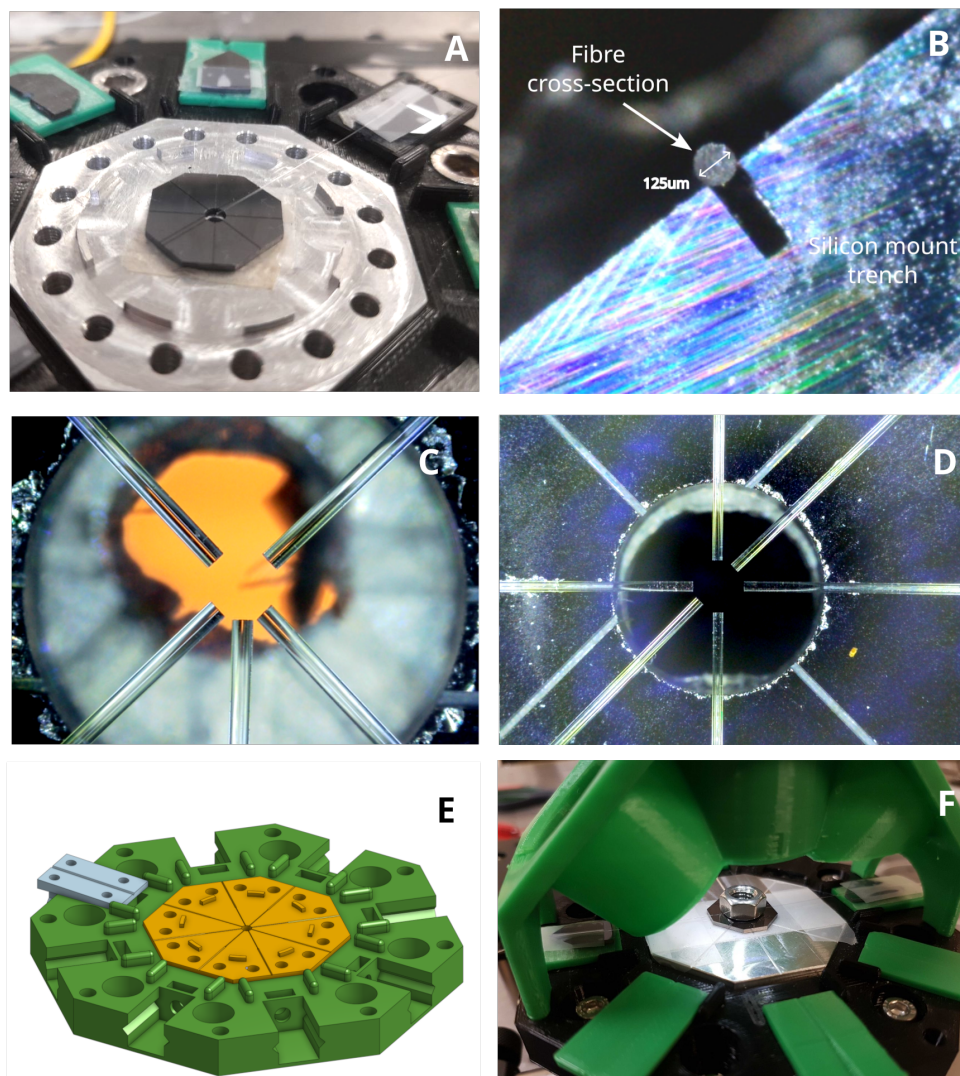


Figure 5.10: Second iteration of the SWIFT configuration. (A) Silicon mount with micromachined trenches developed in collaboration with the Southampton Planar Optical Materials Research Group. (B) Microscope image of the mount cross-section with a fibre on the silicon substrate. (C) and (D) Microscope image of the silicon mount with the fibres in place. (E) Design of the 3d-printed outer mount used for initial delivery of fibres onto the silicon mount for alignment (F) Fibre trap in operation. Hexagonal M3 nut used as an ad-hoc clamping solution.

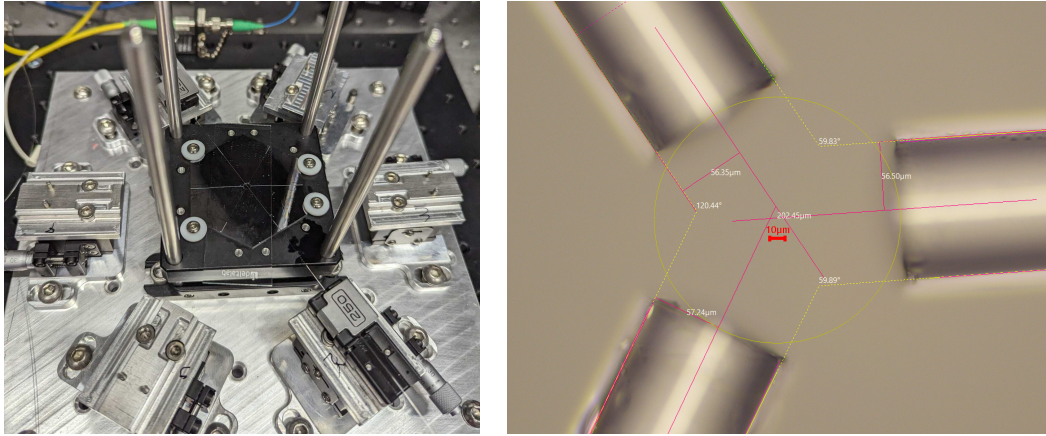


Figure 5.11: Latest iteration of SWIFT for future testing. (Left): Fibres are initially aligned using translation stages and later fixed in place on the SWIFT mount using epoxy glue. (Right): fixed fibre arrangement after alignment. Fibre endfaces positioned $100\ \mu\text{m}$ away from the midpoint. Fibre heights are aligned to less than $1\ \mu\text{m}$ difference.

solid angle, we can imagine milling trenches into the mirror surface to align the fibres with the mirror centre point, or utilising electrostatic forces to shift the equilibrium position of the particle [133]. For a large mirror (with radius $>1\ \text{mm}$) the residual backaction noise from the removed mirror surface should be small. Even so, another issue arises as the trapping light can reflect from the mirror surface and modify the trapping potential, particularly in the hexagonal arrangement in which the trapping fibres would face the metallic surface of the mirror.

We simulate this for a simple arrangement depicted on the left of figure 5.12. We use the SCUFF-EM software package which implements the boundary element method for scattering problems to simulate the reflected fields from the edge of the mirror surface. The amount of memory required in the simulation scales with the number of elements used to mesh the scattering surface. For accurate modelling, most elements need to have dimensions smaller than the wavelength of scattered light. To avoid simulating a whole mm-scale hemisphere, which is not computationally tractable, we simulate only a small patch of the mirror's edge upon which the beam is incident, and

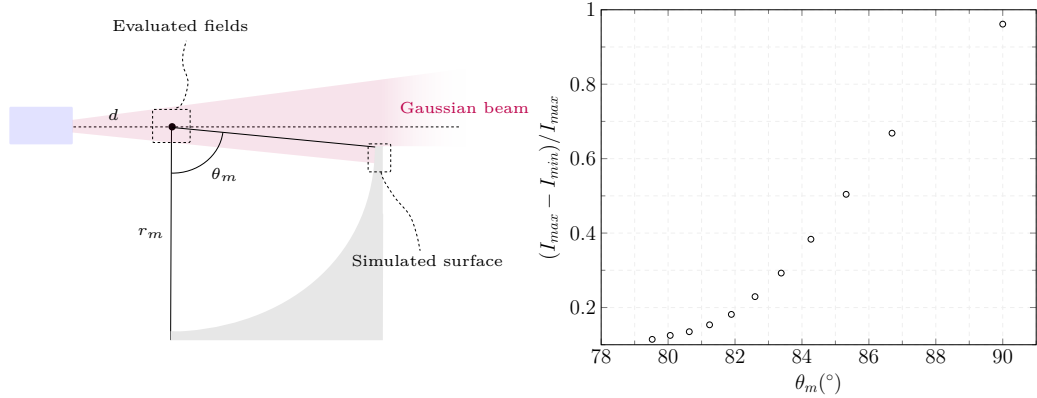


Figure 5.12: Trapping light reflection interference. (Left) Simulation setup. A Gaussian beam aligned with the mirror centre at a distance $d = 100\lambda$, propagating towards a patch of the simulated surface with radius $r_m = 300\lambda$. (Right) Plot of intensity modulation evaluated in a small patch of area $4\lambda^2$ around the mirror centre, plotted against mirror spanning angle θ_m . The simulation was performed using the software suite SCUFF-EM [116, 117] implementing the boundary element method for scattering problems.

that is larger than the beam’s waist at the surface.

Ideally, the intensity of the field in the evaluated region shown in figure 5.12 should be close to uniform. However, interference of the beam with its reflection from the mirror’s edge gives rise to intensity modulation. Large intensity modulation is undesirable as it significantly changes the trapping potential in a way which depends on the mirror radius, and which can destabilise the trap. The simulation results on the right of figure 5.12 shows that the reflection strongly modulates the intensity in the neighbourhood of the mirror centre point for the mirror spanning angle larger than about 70° . This places limits on the maximum θ_m which could realistically be used for demonstrating suppression of backaction using the hexagonal arrangement.

Unlike in the SMART configuration, in SWIFT the particle is polarised along the mirror axis. Figure 5.13 shows the imprecision noise for a particle polarised along the mirror axis (labelled \hat{z} on the plot relative to the coordinate system in figure 3.1) against θ_m at the backaction suppression condition $k_0 r_m = n\pi$ (c.f. figure 3.3). While the figure shows that at about $\theta_m = 70^\circ$ the noise along the mirror axis remains mostly suppressed, we can expect more than

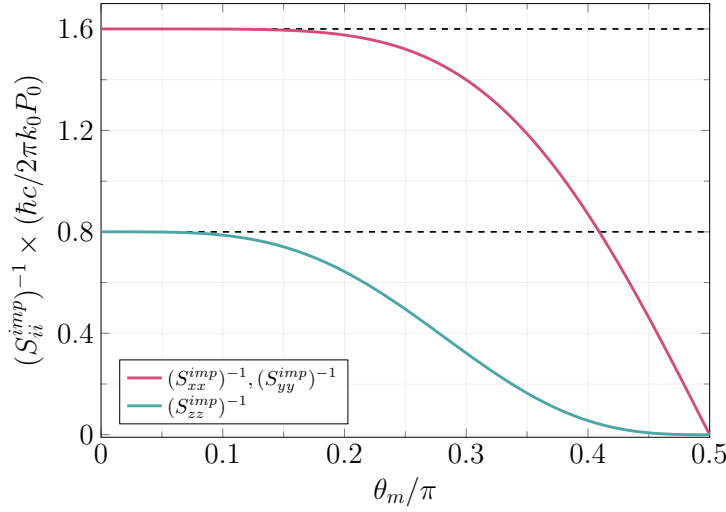


Figure 5.13: Standing wave measurement imprecision S_{ii}^{imp} against spherical mirror NA found by solving (3.12) for a particle polarised along the mirror axis. Filled lines indicate variation with θ_m for $k_0 r_m = n\pi$. Dashed lines indicate free-space levels in a standing wave (at $\theta_m = 0$). For clarity, we note that in a standing wave, the beam axis direction does not enter the calculation.

50% imprecision noise in the orthogonal plane, and correspondingly residual backaction. Based on this consideration, SWIFT does not appear to be the most practical choice for exploiting the suppression effect in three dimensions, but can nonetheless be a sufficient platform for its demonstration.

5.4.3 Residual backaction noise in SWIFT

Just as in section 4.9 for SMART, we analyse the influence of the SIBA force for the SWIFT optical trap potential. We show the trapping forces for the hexagonal SWIFT configuration in figure 5.14. Let us first note some of the similarities and differences between SIBA influence in SWIFT and SMART. In both configurations, SIBA only has a noticeable influence on the force acting along the mirror axis. In SWIFT however, the confinement along the mirror axis is considerably weaker, which leads to a significant reshaping of the trapping potential by the mirror-reflected scatter. Additionally, in contrast to SMART, the bottom left of figure 5.14 shows that the force component F_z has

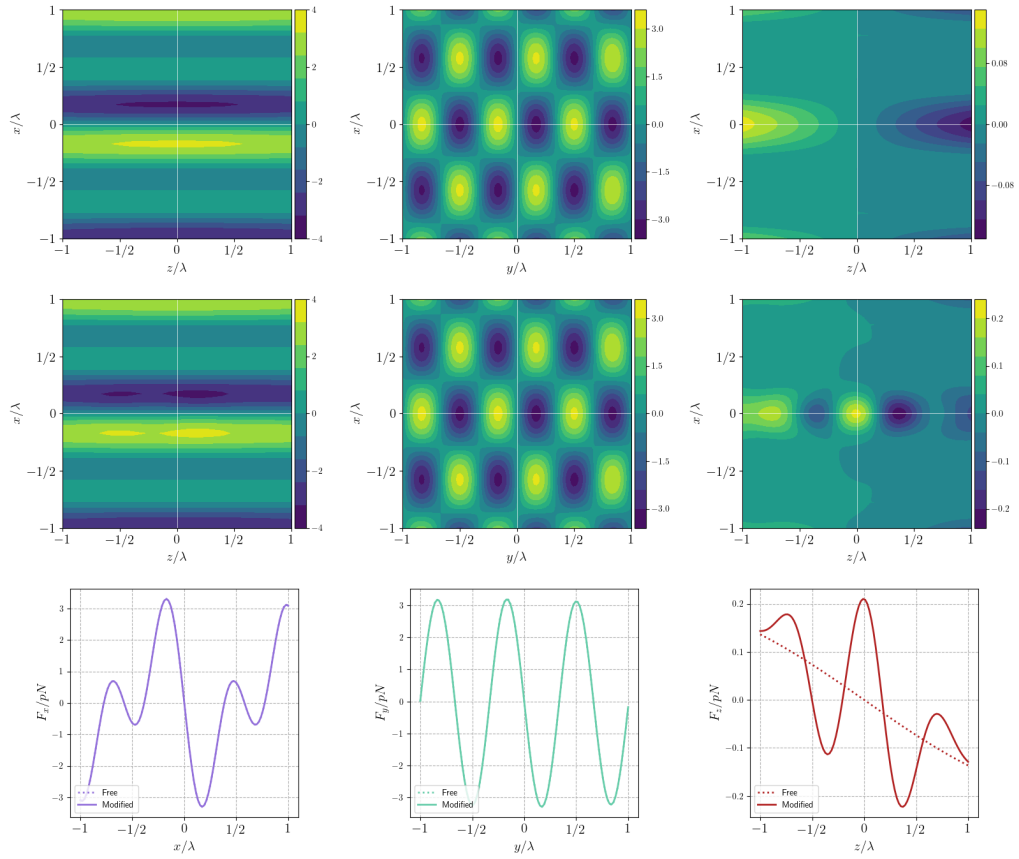


Figure 5.14: Trapping forces acting on a Silica nanosphere of radius $r_p = 150$ nm in the hexagonal SWIFT configuration, with the fibres at a distance of $100 \mu\text{m}$ from the centre point. The beams are in-phase at the origin. **Top:** F_x , F_y and F_z components of the trapping force (pN) in free space **Middle:** F_x , F_y and F_z components of the trapping force (pN) including the effect of the spherical mirror **Bottom:** Slice of the contour plots for F_x , F_y and F_z .

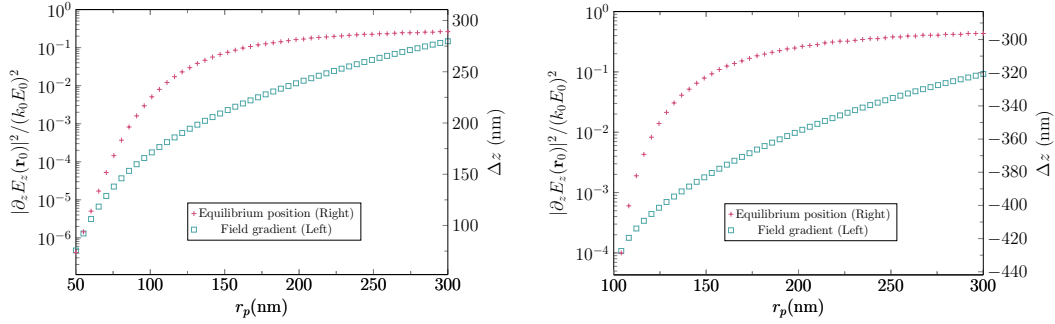


Figure 5.15: Equilibrium position shift Δz and field gradient $|\partial_z \vec{E}(\mathbf{r}_0)|^2 / (k_0 E_0)^2$ against particle radius r_p for the hexagonal SWIFT configuration, with fibres separated by a distance $100 \mu\text{m}$ from the centre point. Results on the left and right plots show results for the positive and negative equilibrium position of the particle respectively.

two equilibrium positions about $z = 0$ (mirror centre).

Using the same arguments as in section 4.9 we now analyse the residual backaction noise experienced by a silica nanosphere at the positive and negative equilibrium positions, due to a non-vanishing field gradient. The result is shown in figure 5.15. In SWIFT, the shift of the trap position away from the mirror centre *decreases* with increasing particle size, and plateaus at around $\Delta z = \pm 300 \text{ nm}$. The shift is an order of magnitude larger than in SMART for equal particle radii, which increases residual backaction according to figure 3.6, but the corresponding residual backaction noise from a non-vanishing field gradient is comparable to SMART.

5.4.4 Residual nanoparticle charge

Silica nanoparticles usually carry some residual charge. In levitated optomechanics, this fact is exploited to control the nanoparticle trap centre position [133] and to cool its motion in a feedback cooling scheme referred to as cold damping [124–126], which relies on applying an electrostatic feedback force on an optically confined particle. This residual charge, however, can potentially render the optical trap unstable if a charged environment exerts

strong electrostatic forces on the particle. This is of particular concern in our SWIFT configuration, as the trap site is surrounded by large dielectric surfaces of the optical fibres at distances of $\sim 100 \mu\text{m}$ which themselves can accumulate charge. This is an issue known from the miniaturisation efforts of ion traps [134,135]. Effects of residual charge may be the current limiting factor on the operation of the SWIFT configuration. Nonetheless, some experimental steps can be taken in the future implementations to minimise these detrimental influences. On one hand, one can strive for discharging the nanoparticle, in which case the particle would no longer be susceptible to electrostatic forces. It has been shown recently, that the net charge of an optically trapped nanoparticle can be controlled on the level of individual elementary charges, without excessive modifications of the trapping architecture [114, 136]. In the context of SWIFT, an auxiliary stable optical trap may be required to implement the discharging scheme.

On the other hand, efforts can be made to neutralise the trap site itself using a neutralising ion gun (for example, Top Gun III from Simco-Ion [137]). In addition an Indium-Tin-Oxide (ITO) coated glass cover could be used, to clamp the fibres in place and serve as a discharge channel.

Conclusion

To summarise, we have found that a suitable structured environment can yield significant reduction of mechanical noise due to laser recoil. We have studied a highly reflective spherical mirror as a particular case, and found that it can be used to inhibit the force noise from laser recoil in three dimensions. The suppression scheme also requires the particle to be trapped in a standing wave trapping field. A partial suppression effect can be achieved with selective patches of the spherical mirror geometry, which could be used to increase the effective collection efficiency in an experiment.

Counter-intuitively, our results show that the suppression condition is also the condition for which the scattered power, usually associated with recoil noise, is maximally enhanced by the spherical mirror. This is in contrast to recent findings [91], which suggest that suppression of emission leads to suppression of backaction noise. Our result can be understood in the context of the position information content in the outgoing particle scatter; at the suppression condition, the image dipole appears identical to the real particle to first order in particle position about the mirror centre, preventing localisation in a position tracking experiment. For all experimental conditions considered, we have shown that this measurement imprecision and the corresponding backaction satisfy the Heisenberg limit of detection. The method presented here shows how an appropriate reflective surface geometry can be used to mitigate backaction, and may enable development of more sophisticated schemes for particles of different sizes and shapes in future experiments. In addition, a wider range of geometries may be suitable, if one

wishes to suppress the backaction noise only in one or two directions.

The amount by which recoil noise can be suppressed using our method will either be limited by experimental factors (such as mirror reflectivity, thermal stability or surface quality) or smaller residual backaction noise terms unaccounted for in our calculation. Our result predicts particle reheating due to backaction, but future studies will require a quantum description to model evolution of particle motion near surfaces [59]. Additional insight might be gained from studies of the modified radiation damping near surfaces, which balance the fluctuations due to backaction [87].

The analysis of our experimental configuration in chapter 4 shows that the suppression conditions can be met conveniently with a focused beam retroreflected from a spherical mirror. The experimental results for the setup constructed in this project demonstrate it to be a robust trapping geometry, which serves as the first step in realising our backaction suppression scheme. Future efforts will need to be placed on developing precise particle loading and positioning protocols within the standing wave trap. Experimental observation of the suppression effect on the particle reheating trajectories will require mitigation of common sources of mechanical noise, which usually swamp the weak effect of backaction, and implementation of feedback cooling. The SMART configuration may be able to facilitate implementation of the optical cold damping scheme in a standing wave, which was recently used for cooling the particle motion close to the ground-state [114]. Successful application of the backaction suppression scheme may extend coherence times of quantum states of motion of trapped particles, and enable new types of experiments, aiming at developing macroscopic quantum superpositions, in which the trapping laser need not be switched off.

Appendix A

Mathematical definitions and results

A.1 Mathematical definitions

In this thesis, we define the time-domain Fourier transform and its inverse with,

$$\begin{aligned}\tilde{a}(\omega) &= \frac{1}{2\pi} \int_{\mathbb{R}} a(t) e^{i\omega t} dt \\ a(t) &= \int_{\mathbb{R}} \tilde{a}(\omega) e^{-i\omega t} d\omega\end{aligned}\tag{A.1}$$

We will also use the following definition of the convolution,

$$\{\tilde{a} * \tilde{b}\}(\mathbf{r}_0, \omega) = \int_{\mathbb{R}} \tilde{a}(\mathbf{r}_0, \omega') \tilde{b}(\mathbf{r}_0, \omega - \omega') d\omega'\tag{A.2}$$

for two scalars, and for a scalar and a vector

$$\{\tilde{a} * \tilde{\mathbf{b}}\}(\mathbf{r}_0, \omega) = \int_{\mathbb{R}} \tilde{a}(\mathbf{r}_0, \omega') \tilde{\mathbf{b}}(\mathbf{r}_0, \omega - \omega') d\omega'\tag{A.3}$$

A.2 Phase shift of focused fields

Consider a field focused along z to $z = 0$ from ∞ to $-\infty$. Angular spectrum representation tells us that we can always represent fields in terms of its two-dimensional Fourier transform of the spatial plane coordinates [13]. With this Fourier representation of the fields in the focal plane $z = 0$ we can write the fields as,

$$\mathbf{E}(x, y, z) = \int \tilde{\mathbf{E}}(k_x, k_y) e^{i\mathbf{k}\cdot\mathbf{r}} dk_x dk_y \quad (\text{A.4})$$

where $\mathbf{k} = (k_x, k_y, k_z)$, $\mathbf{r} = (x, y, z)$ and $\tilde{\mathbf{E}}(k_x, k_y)$ is the angular spectrum representation of \mathbf{E} in the plane $z = 0$. For large distances from the focal plane $r = \sqrt{x^2 + y^2 + z^2}$, the integral in equation (A.4) can be solved by the method of stationary phase with a solution for the far-field, [80]

$$\mathbf{E}(x, y, z) \approx \frac{2\pi i \sigma}{kr \sqrt{|\Delta|}} \tilde{\mathbf{E}}(kp, kq) e^{ikr g(p, q)} \quad (\text{A.5})$$

with $g(p, q) = (px + qy + mz)/r$, $\Delta = g_{pp} - g_{pq}^2$, $\Sigma = g_{pp} + g_{qq}$ where the subscripts denote derivatives and,

$$\begin{aligned} \sigma &= +1, & \Delta > 0, \Sigma > 0 \\ &= -1, & \Delta > 0, \Sigma < 0 \\ &= -i, & \Delta < 0. \end{aligned} \quad (\text{A.6})$$

For the fields considered in this section, we have $k_z = km = -k\sqrt{1 - p^2 - q^2}$ in both half-spaces. Evaluating the solution in equation (A.5) for this condition gives the solutions,

$$\begin{aligned} \mathbf{E}^+(\mathbf{r}) &= \frac{2\pi i}{k^2 r} k_z \tilde{\mathbf{E}}(-k_x, -k_y) e^{-ikr} & z > 0 \\ \mathbf{E}^-(\mathbf{r}) &= -\frac{2\pi i}{k^2 r} k_z \tilde{\mathbf{E}}(k_x, k_y) e^{ikr} & z < 0 \end{aligned} \quad (\text{A.7})$$

where $k_x = kx/r$, $k_y = ky/r$ and $k_z = -\sqrt{k^2 - k_x^2 - k_y^2}$. We can link the two expressions for the far-fields giving the final result,

$$\mathbf{E}^-(\mathbf{r}) = -e^{2ikr} \mathbf{E}^+(-\mathbf{r}). \quad (\text{A.8})$$

which tells us that the far-fields map along antipodes, with a phase corresponding to the path difference $2kr$ and a π phase delay.

Appendix B

Imprecision and backaction calculation details

B.1 Green's function derivatives

The free space dyadic Green's function is given by,

$$\overline{\overline{\mathbf{G}}}_0(\mathbf{r}, \mathbf{r}') = \left(\left[\frac{3}{k^2 R^2} - \frac{3i}{kR} - 1 \right] \hat{R}\hat{R} + \left[1 + \frac{i}{kR} - \frac{1}{k^2 R^2} \right] \overline{\overline{\mathbf{I}}} \right) G_0(R) \quad (\text{B.1})$$

where,

$$G_0(R) = \frac{\exp(ikR)}{4\pi R} \quad (\text{B.2})$$
$$R = |\mathbf{r} - \mathbf{r}'|$$

Because of the functional form of (B.1) it is more convenient to compute the derivative ∂_i with respect to the radial distance R ,

$$\partial_i \overline{\overline{\mathbf{G}}}_0(\mathbf{r}, \mathbf{r}') = \frac{\partial R}{\partial x_i} \frac{\partial}{\partial R} \overline{\overline{\mathbf{G}}}_0(\mathbf{r}, \mathbf{r}') = \hat{R}_i \frac{\partial}{\partial R} \overline{\overline{\mathbf{G}}}_0(\mathbf{r}, \mathbf{r}') \quad (\text{B.3})$$

where \hat{R}_i is the i th component of the unit radial vector \hat{R} whose direction depends on the direction of the derivative. For the second derivative we find,

$$\partial_i \partial'_j \overline{\mathbf{G}}_0(\mathbf{r}, \mathbf{r}') = \left(\left[\hat{R}_i \hat{R}_j - \delta_{ij} \right] \frac{1}{R} \frac{\partial}{\partial R} - \hat{R}_i \hat{R}_j \frac{\partial^2}{\partial^2 R} \right) \overline{\mathbf{G}}_0(\mathbf{r}, \mathbf{r}'). \quad (\text{B.4})$$

The derivative in equation (B.4) is singular at $\mathbf{r} = \mathbf{r}'$ in general, but not when we take the limit $R \rightarrow 0$ for the imaginary part. Evaluating the radial derivatives and taking this limit gives the result,

$$\begin{aligned} \partial_i \partial'_j \text{Im} \left[G_0^{kl}(\mathbf{r}, \mathbf{r}') \right]_{\mathbf{r}=\mathbf{r}'} &= \lim_{R \rightarrow 0} \partial_i \partial'_j \text{Im} \left[G_0^{kl}(\mathbf{r}, \mathbf{r}') \right] \\ &= \frac{k^3}{30\pi} \delta_{ij} (2\delta_{kl} - \delta_{ki} \delta_{lj}) \end{aligned} \quad (\text{B.5})$$

The same result is obtained when one computes the derivative of only the far-field component of the imaginary Green's function, which shows that the $(kR)^{-2}$ and $(kR)^{-3}$ terms do not contribute. This provides some insight into why reflection of only the far-field light is sufficient for full modulation of backaction noise.

B.2 Solutions for perfectly reflecting mirror with varying NA

For a spherical mirror with reflection coefficient $|\rho| = 1$, the solution to (3.12) for varying mirror NA specified by the polar half angle θ_m (see figure 3.1) is given by,

$$S_{\text{imp}}^i = \frac{\hbar c}{2\pi k_0} \frac{1}{P_0} f_i \quad (\text{B.6})$$

where,

$$\begin{aligned} f_x &= 320(256 + \text{Re} \left[\rho e^{2ikr_m} \right] [256 - 270 \cos(\theta_m) + 5 \cos(3\theta_m) + 9 \cos(5\theta_m)])^{-1} \\ f_y &= 320(512 + \text{Re} \left[\rho e^{2ikr_m} \right] [512 - 570 \cos(\theta_m) + 55 \cos(3\theta_m) + 3 \cos(5\theta_m)])^{-1} \\ f_z &= 10(-16 + \text{Re} \left[\rho e^{2ikr_m} \right] [-16 + \cos(\theta_m)^3 (13 + 3 \cos(2\theta_m))])^{-1} \end{aligned} \quad (\text{B.7})$$

Solutions to (3.39) for varying θ_m are given by,

$$\begin{aligned}
 S_{xx}^F(\omega) &= \frac{\hbar k_0}{2\pi c} P_0 \left(\frac{1}{5} + \frac{\text{Re} [\rho e^{2ikr_m}]}{1280} \left[256 - 270 \cos(\theta_m) + 5 \cos(3\theta_m) + 9 \cos(5\theta_m) \right] \right) \\
 S_{yy}^F(\omega) &= \frac{\hbar k_0}{2\pi c} P_0 \left(\frac{2}{5} + \frac{\text{Re} [\rho e^{2ikr_m}]}{1280} \left[512 - 570 \cos(\theta_m) + 55 \cos(3\theta_m) + 3 \cos(5\theta_m) \right] \right) \\
 S_{zz}^F(\omega) &= \frac{\hbar k_0}{2\pi c} P_0 \left(\frac{2}{5} + \text{Re} [\rho e^{2ikr_m}] \left[\frac{1}{80} \cos(\theta_m)^3 [13 + 3 \cos(2\theta_m)] \right] \right)
 \end{aligned} \tag{B.8}$$

Bibliography

- [1] Carlton M. Caves. Quantum-mechanical radiation-pressure fluctuations in an interferometer. *Phys. Rev. Lett.*, 45:75–79, Jul 1980. URL: <https://link.aps.org/doi/10.1103/PhysRevLett.45.75>, doi:10.1103/PhysRevLett.45.75.
- [2] Anatoliĭ Borisovich Manukin V. B. Braginskiĭ. *Measurement of weak forces in physics experiments*. University of Chicago Press, 1977.
- [3] A. A. Clerk, M. H. Devoret, S. M. Girvin, Florian Marquardt, and R. J. Schoelkopf. Introduction to quantum noise, measurement, and amplification. *Rev. Mod. Phys.*, 82:1155–1208, Apr 2010. URL: <https://link.aps.org/doi/10.1103/RevModPhys.82.1155>, doi:10.1103/RevModPhys.82.1155.
- [4] B. P. Abbott, R. Abbott, T. D. Abbott, M. R. Abernathy, F. Acernese, K. Ackley, C. Adams, T. Adams, P. Addesso, R. X. Adhikari, V. B. Adya, C. Affeldt, and Agathos *et al.* Observation of gravitational waves from a binary black hole merger. *Phys. Rev. Lett.*, 116:061102, Feb 2016. URL: <https://link.aps.org/doi/10.1103/PhysRevLett.116.061102>, doi:10.1103/PhysRevLett.116.061102.
- [5] K. L. Ekinici and M. L. Roukes. Nanoelectromechanical systems. *Review of Scientific Instruments*, 76(6):061101, 05 2005. arXiv:https://pubs.aip.org/aip/rsi/article-pdf/doi/10.1063/1.1927327/16000132/061101\1\1_online.pdf, doi:10.1063/1.1927327.

- [6] O. Arcizet, P.-F. Cohadon, T. Briant, M. Pinard, and A. Heidmann. Radiation-pressure cooling and optomechanical instability of a micromirror. *Nature*, 444(7115):71–74, Nov 2006. doi:10.1038/nature05244.
- [7] Markus Aspelmeyer, Tobias J. Kippenberg, and Florian Marquardt. Cavity optomechanics. *Rev. Mod. Phys.*, 86:1391–1452, Dec 2014. URL: <https://link.aps.org/doi/10.1103/RevModPhys.86.1391>, doi:10.1103/RevModPhys.86.1391.
- [8] D. K. Armani, T. J. Kippenberg, S. M. Spillane, and K. J. Vahala. Ultra-high-q toroid microcavity on a chip. *Nature*, 421(6926):925–928, Feb 2003. doi:10.1038/nature01371.
- [9] A. Schliesser, R. Rivière, G. Anetsberger, O. Arcizet, and T. J. Kippenberg. Resolved-sideband cooling of a micromechanical oscillator. *Nature Physics*, 4(5):415–419, May 2008. doi:10.1038/nphys939.
- [10] Matt Eichenfield, Jasper Chan, Ryan M. Camacho, Kerry J. Vahala, and Oskar Painter. Optomechanical crystals. *Nature*, 462(7269):78–82, Nov 2009. doi:10.1038/nature08524.
- [11] T. P. Purdy, R. W. Peterson, and C. A. Regal. Observation of radiation pressure shot noise on a macroscopic object. *Science*, 339(6121):801–804, 2013. URL: <https://www.science.org/doi/abs/10.1126/science.1231282>, arXiv:<https://www.science.org/doi/pdf/10.1126/science.1231282>, doi:10.1126/science.1231282.
- [12] Peter Horak, Gerald Hechenblaikner, Klaus M. Gheri, Herwig Stecher, and Helmut Ritsch. Cavity-induced atom cooling in the strong coupling regime. *Phys. Rev. Lett.*, 79:4974–4977, Dec 1997. URL: <https://link.aps.org/doi/10.1103/PhysRevLett.79.4974>, doi:10.1103/PhysRevLett.79.4974.
- [13] Lukas Novotny and Bert Hecht. *Principles of nano-optics*. Cambridge university press, 2012.

- [14] Jasper Chan, T. P. Mayer Alegre, Amir H. Safavi-Naeini, Jeff T. Hill, Alex Krause, Simon Gröblacher, Markus Aspelmeyer, and Oskar Painter. Laser cooling of a nanomechanical oscillator into its quantum ground state. *Nature*, 478(7367):89–92, Oct 2011. doi:[10.1038/nature10461](https://doi.org/10.1038/nature10461).
- [15] Michael A. Page, Maxim Goryachev, Haixing Miao, Yanbei Chen, Yiqiu Ma, David Mason, Massimiliano Rossi, Carl D. Blair, Li Ju, David G. Blair, Albert Schliesser, Michael E. Tobar, and Chunnong Zhao. Gravitational wave detectors with broadband high frequency sensitivity. *Communications Physics*, 4(1):27, Feb 2021. doi:[10.1038/s42005-021-00526-2](https://doi.org/10.1038/s42005-021-00526-2).
- [16] David Mason, Junxin Chen, Massimiliano Rossi, Yeghishe Tsaturyan, and Albert Schliesser. Continuous force and displacement measurement below the standard quantum limit. *Nature Physics*, 15(8):745–749, Aug 2019. doi:[10.1038/s41567-019-0533-5](https://doi.org/10.1038/s41567-019-0533-5).
- [17] Bei-Bei Li, Lingfeng Ou, Yuechen Lei, and Yong-Chun Liu. Cavity optomechanical sensing. *Nanophotonics*, 10(11):2799–2832, 2021. URL: <https://doi.org/10.1515/nanoph-2021-0256> [cited 2024-01-21], doi:[10.1515/nanoph-2021-0256](https://doi.org/10.1515/nanoph-2021-0256).
- [18] Carlton M. Caves. Quantum-mechanical noise in an interferometer. *Phys. Rev. D*, 23:1693–1708, Apr 1981. URL: <https://link.aps.org/doi/10.1103/PhysRevD.23.1693>, doi:[10.1103/PhysRevD.23.1693](https://doi.org/10.1103/PhysRevD.23.1693).
- [19] Bei-Bei Li, Jan Břílek, Ulrich B. Hoff, Lars S. Madsen, Stefan Forstner, Varun Prakash, Clemens Schäfermeier, Tobias Gehring, Warwick P. Bowen, and Ulrik L. Andersen. Quantum enhanced optomechanical magnetometry. *Optica*, 5(7):850–856, Jul 2018. URL: <https://opg.optica.org/optica/abstract.cfm?URI=optica-5-7-850>, doi:[10.1364/OPTICA.5.000850](https://doi.org/10.1364/OPTICA.5.000850).

- [20] E. Schrödinger. Die gegenwärtige situation in der quantenmechanik. *Naturwissenschaften*, 23(48):807–812, Nov 1935. doi:[10.1007/BF01491891](https://doi.org/10.1007/BF01491891).
- [21] A J Leggett. Testing the limits of quantum mechanics: motivation, state of play, prospects. *Journal of Physics: Condensed Matter*, 14(15):R415, apr 2002. URL: <https://dx.doi.org/10.1088/0953-8984/14/15/201>, doi:[10.1088/0953-8984/14/15/201](https://doi.org/10.1088/0953-8984/14/15/201).
- [22] Yaakov Y. Fein, Philipp Geyer, Patrick Zwick, Filip Kiałka, Sebastian Pedalino, Marcel Mayor, Stefan Gerlich, and Markus Arndt. Quantum superposition of molecules beyond 25 kda. *Nature Physics*, 15(12):1242–1245, Dec 2019. doi:[10.1038/s41567-019-0663-9](https://doi.org/10.1038/s41567-019-0663-9).
- [23] Shabir Barzanjeh, André Xuereb, Simon Gröblacher, Mauro Paternostro, Cindy A. Regal, and Eva M. Weig. Optomechanics for quantum technologies. *Nature Physics*, 18(1):15–24, Jan 2022. doi:[10.1038/s41567-021-01402-0](https://doi.org/10.1038/s41567-021-01402-0).
- [24] Amir Youssefi, Shingo Kono, Mahdi Chegnizadeh, and Tobias J. Kippenberg. A squeezed mechanical oscillator with millisecond quantum decoherence. *Nature Physics*, 19(11):1697–1702, Nov 2023. doi:[10.1038/s41567-023-02135-y](https://doi.org/10.1038/s41567-023-02135-y).
- [25] Ralf Riedinger, Andreas Wallucks, Igor Marinković, Clemens Löschnauer, Markus Aspelmeyer, Sungkun Hong, and Simon Gröblacher. Remote quantum entanglement between two micromechanical oscillators. *Nature*, 556(7702):473–477, Apr 2018. doi:[10.1038/s41586-018-0036-z](https://doi.org/10.1038/s41586-018-0036-z).
- [26] D. J. Wilson, V. Sudhir, N. Piro, R. Schilling, A. Ghadimi, and T. J. Kippenberg. Measurement-based control of a mechanical oscillator at its thermal decoherence rate. *Nature*, 524(7565):325–329, Aug 2015. doi:[10.1038/nature14672](https://doi.org/10.1038/nature14672).

- [27] P. F. Barker and M. N. Shneider. Cavity cooling of an optically trapped nanoparticle. *Phys. Rev. A*, 81:023826, Feb 2010. URL: <https://link.aps.org/doi/10.1103/PhysRevA.81.023826>, doi:10.1103/PhysRevA.81.023826.
- [28] D. E. Chang, C. A. Regal, S. B. Papp, D. J. Wilson, J. Ye, O. Painter, H. J. Kimble, and P. Zoller. Cavity opto-mechanics using an optically levitated nanosphere. *Proceedings of the National Academy of Sciences*, 107(3):1005–1010, 2010. URL: <https://www.pnas.org/doi/abs/10.1073/pnas.0912969107>, arXiv:<https://www.pnas.org/doi/pdf/10.1073/pnas.0912969107>, doi:10.1073/pnas.0912969107.
- [29] O. Romero-Isart, A. C. Pflanzer, F. Blaser, R. Kaltenbaek, N. Kiesel, M. Aspelmeyer, and J. I. Cirac. Large quantum superpositions and interference of massive nanometer-sized objects. *Phys. Rev. Lett.*, 107:020405, Jul 2011. URL: <https://link.aps.org/doi/10.1103/PhysRevLett.107.020405>, doi:10.1103/PhysRevLett.107.020405.
- [30] David C Moore and Andrew A Geraci. Searching for new physics using optically levitated sensors. *Quantum Science and Technology*, 6(1):014008, Jan 2021. URL: <http://dx.doi.org/10.1088/2058-9565/abcf8a>, doi:10.1088/2058-9565/abcf8a.
- [31] A. Ashkin. Acceleration and trapping of particles by radiation pressure. *Phys. Rev. Lett.*, 24:156–159, Jan 1970. URL: <https://link.aps.org/doi/10.1103/PhysRevLett.24.156>, doi:10.1103/PhysRevLett.24.156.
- [32] A. Ashkin and J. M. Dziedzic. Optical Levitation by Radiation Pressure. *Applied Physics Letters*, 19(8):283–285, October 1971. doi:10.1063/1.1653919.
- [33] A. Ashkin, J. M. Dziedzic, J. E. Bjorkholm, and Steven Chu. Observation of a single-beam gradient force optical trap for dielectric particles. *Opt. Lett.*, 11(5):288–290, May 1986. URL: <https://opg.optica.org/ol/abstract.cfm?URI=ol-11-5-288>, doi:10.1364/OL.11.000288.

- [34] Ryota Omori, Tamiki Kobayashi, and Atsuyuki Suzuki. Observation of a single-beam gradient-force optical trap for dielectric particles in air. *Opt. Lett.*, 22(11):816–818, Jun 1997. URL: <https://opg.optica.org/ol/abstract.cfm?URI=ol-22-11-816>, doi:10.1364/OL.22.000816.
- [35] M. D. Summers, D. R. Burnham, and D. McGloin. Trapping solid aerosols with optical tweezers: A comparison between gas and liquid phase optical traps. *Opt. Express*, 16(11):7739–7747, May 2008. URL: <https://opg.optica.org/oe/abstract.cfm?URI=oe-16-11-7739>, doi:10.1364/OE.16.007739.
- [36] Tongcang Li, Simon Kheifets, and Mark G. Raizen. Millikelvin cooling of an optically trapped microsphere in vacuum. *Nature Physics*, 7(7):527–530, Jul 2011. doi:10.1038/nphys1952.
- [37] Jan Gieseler, Bradley Deutsch, Romain Quidant, and Lukas Novotny. Subkelvin parametric feedback cooling of a laser-trapped nanoparticle. *Physical Review Letters*, 109(10), Sep 2012. URL: <http://dx.doi.org/10.1103/PhysRevLett.109.103603>, doi:10.1103/physrevlett.109.103603.
- [38] Vijay Jain, Jan Gieseler, Clemens Moritz, Christoph Dellago, Romain Quidant, and Lukas Novotny. Direct measurement of photon recoil from a levitated nanoparticle. *Physical Review Letters*, 116(24), Jun 2016. URL: <http://dx.doi.org/10.1103/PhysRevLett.116.243601>, doi:10.1103/physrevlett.116.243601.
- [39] Nikolai Kiesel, Florian Blaser, Uroš Delić, David Grass, Rainer Kaltenbaek, and Markus Aspelmeyer. Cavity cooling of an optically levitated submicron particle. *Proceedings of the National Academy of Sciences*, 110(35):14180–14185, 2013. URL: <https://www.pnas.org/doi/abs/10.1073/pnas.1309167110>, arXiv:<https://www.pnas.org/doi/pdf/10.1073/pnas.1309167110>, doi:10.1073/pnas.1309167110.

- [40] Nadine Meyer, Andrés de los Ríos Sommer, Pau Mestres, Jan Gieseler, Vijay Jain, Lukas Novotny, and Romain Quidant. Resolved-sideband cooling of a levitated nanoparticle in the presence of laser phase noise. *Phys. Rev. Lett.*, 123:153601, Oct 2019. URL: <https://link.aps.org/doi/10.1103/PhysRevLett.123.153601>, doi: [10.1103/PhysRevLett.123.153601](https://doi.org/10.1103/PhysRevLett.123.153601).
- [41] Uroš Delić, Manuel Reisenbauer, David Grass, Nikolai Kiesel, Vladan Vuletić, and Markus Aspelmeyer. Cavity cooling of a levitated nanosphere by coherent scattering. *Phys. Rev. Lett.*, 122:123602, Mar 2019. URL: <https://link.aps.org/doi/10.1103/PhysRevLett.122.123602>, doi: [10.1103/PhysRevLett.122.123602](https://doi.org/10.1103/PhysRevLett.122.123602).
- [42] Uroš Delić, Manuel Reisenbauer, Kahan Dare, David Grass, Vladan Vuletić, Nikolai Kiesel, and Markus Aspelmeyer. Cooling of a levitated nanoparticle to the motional quantum ground state. *Science*, 367(6480):892–895, 2020. URL: <https://www.science.org/doi/abs/10.1126/science.aba3993>, arXiv:<https://www.science.org/doi/pdf/10.1126/science.aba3993>, doi: [10.1126/science.aba3993](https://doi.org/10.1126/science.aba3993).
- [43] Johannes Piotrowski, Dominik Windey, Jayadev Vijayan, Carlos Gonzalez-Ballester, Andrés de los Ríos Sommer, Nadine Meyer, Romain Quidant, Oriol Romero-Isart, René Reimann, and Lukas Novotny. Simultaneous ground-state cooling of two mechanical modes of a levitated nanoparticle. *Nature Physics*, 19(7):1009–1013, Jul 2023. doi: [10.1038/s41567-023-01956-1](https://doi.org/10.1038/s41567-023-01956-1).
- [44] Lorenzo Magrini, Philipp Rosenzweig, Constanze Bach, Andreas Deutschmann-Olek, Sebastian G. Hofer, Sungkun Hong, Nikolai Kiesel, Andreas Kugi, and Markus Aspelmeyer. Real-time optimal quantum control of mechanical motion at room temperature. *Nature*, 595(7867):373–377, Jul 2021. doi: [10.1038/s41586-021-03602-3](https://doi.org/10.1038/s41586-021-03602-3).
- [45] Björn Brezger, Lucia Hackermüller, Stefan Uttenthaler, Julia Petschinka, Markus Arndt, and Anton Zeilinger. Matter-wave interferometer

- for large molecules. *Phys. Rev. Lett.*, 88:100404, Feb 2002. URL: <https://link.aps.org/doi/10.1103/PhysRevLett.88.100404>, doi: [10.1103/PhysRevLett.88.100404](https://doi.org/10.1103/PhysRevLett.88.100404).
- [46] James Bateman, Stefan Nimmrichter, Klaus Hornberger, and Hendrik Ulbricht. Near-field interferometry of a free-falling nanoparticle from a point-like source. *Nature Communications*, 5(1):4788, Sep 2014. doi: [10.1038/ncomms5788](https://doi.org/10.1038/ncomms5788).
- [47] Rainer Kaltenbaek, Markus Arndt, Markus Aspelmeyer, Peter F. Barker, Angelo Bassi, James Bateman, Alessio Belenchia, Joel Bergé, Sougato Bose, Claus Braxmaier, Bruno Christophe, Garrett D. Cole, Catalina Curceanu, Animesh Datta, Maxime Debiossac, Uroš Delić, Lajos Diósi, Andrew A. Geraci, Stefan Gerlich, Christine Guerlin, Gerald Hechenblaikner, Antoine Heidmann, Sven Herrmann, Klaus Hornberger, Ulrich Johann, Nikolai Kiesel, Thomas W. LeBrun, Gerard J. Milburn, James Millen, Makan Mohageg, David C. Moore, Gavin W. Morley, Stefan Nimmrichter, Lukas Novotny, Daniel K. L. Oi, Mauro Paternostro, C. Jess Riedel, Manuel Rodrigues, Loïc Rondin, Albert Roura, Wolfgang P. Schleich, Thilo Schuldt, Benjamin A. Stickler, Hendrik Ulbricht, Christian Vogt, and Lisa Wörner. MAQRO – BPS 2023 research campaign whitepaper, 2022. [arXiv:2202.01535](https://arxiv.org/abs/2202.01535).
- [48] Jan Gieseler and James Millen. Levitated nanoparticles for microscopic thermodynamics—a review. *Entropy*, 20(5), 2018. URL: <https://www.mdpi.com/1099-4300/20/5/326>, doi: [10.3390/e20050326](https://doi.org/10.3390/e20050326).
- [49] Nancy Aggarwal, George P. Winstone, Mae Teo, Masha Baryakhtar, Shane L. Larson, Vicky Kalogera, and Andrew A. Geraci. Searching for new physics with a levitated-sensor-based gravitational-wave detector. *Phys. Rev. Lett.*, 128:111101, Mar 2022. URL: <https://link.aps.org/doi/10.1103/PhysRevLett.128.111101>, doi: [10.1103/PhysRevLett.128.111101](https://doi.org/10.1103/PhysRevLett.128.111101).

- [50] Stefan Kuhn, Benjamin A. Stickler, Alon Kosloff, Fernando Patolsky, Klaus Hornberger, Markus Arndt, and James Millen. Optically driven ultra-stable nanomechanical rotor. *Nature Communications*, 8(1), Nov 2017. URL: <http://dx.doi.org/10.1038/s41467-017-01902-9>, doi:10.1038/s41467-017-01902-9.
- [51] Jonghoon Ahn, Zhuqing Xu, Jaehoon Bang, Peng Ju, Xingyu Gao, and Tongcang Li. Ultrasensitive torque detection with an optically levitated nanorotor. *Nature Nanotechnology*, 15(2):89–93, Feb 2020. doi:10.1038/s41565-019-0605-9.
- [52] George Winstone, Zhiyuan Wang, Shelby Klomp, Robert G. Felsted, Andrew Laeuger, Chaman Gupta, Daniel Grass, Nancy Aggarwal, Jacob Sprague, Peter J. Pauzauskie, Shane L. Larson, Vicky Kalogera, and Andrew A. Geraci. Optical trapping of high-aspect-ratio nayf hexagonal prisms for kHz-MHz gravitational wave detectors. *Phys. Rev. Lett.*, 129:053604, Jul 2022. URL: <https://link.aps.org/doi/10.1103/PhysRevLett.129.053604>, doi:10.1103/PhysRevLett.129.053604.
- [53] C. Gonzalez-Ballesteros, M. Aspelmeyer, L. Novotny, R. Quidant, and O. Romero-Isart. Levitodynamics: Levitation and control of microscopic objects in vacuum. *Science*, 374(6564):eabg3027, 2021. URL: <https://www.science.org/doi/abs/10.1126/science.abg3027>, arXiv: <https://www.science.org/doi/pdf/10.1126/science.abg3027>, doi:10.1126/science.abg3027.
- [54] Gerard P. Conangla, Raúl A. Rica, and Romain Quidant. Extending vacuum trapping to absorbing objects with hybrid paul-optical traps. *Nano Letters*, 20(8):6018–6023, 2020. PMID: 32692184. arXiv:<https://doi.org/10.1021/acs.nanolett.0c02025>, doi:10.1021/acs.nanolett.0c02025.
- [55] T. Delord, P. Huillery, L. Schwab, L. Nicolas, L. Lecordier, and G. Hétet. Ramsey interferences and spin echoes from electron spins

- inside a levitating macroscopic particle. *Phys. Rev. Lett.*, 121:053602, Jul 2018. URL: <https://link.aps.org/doi/10.1103/PhysRevLett.121.053602>, doi:10.1103/PhysRevLett.121.053602.
- [56] C. Gonzalez-Ballester, J.A. Zielińska, M. Rossi, A. Militaru, M. Frimmer, L. Novotny, P. Maurer, and O. Romero-Isart. Suppressing recoil heating in levitated optomechanics using squeezed light. *PRX Quantum*, 4:030331, Sep 2023. URL: <https://link.aps.org/doi/10.1103/PRXQuantum.4.030331>, doi:10.1103/PRXQuantum.4.030331.
- [57] G. S. Agarwal. Quantum electrodynamics in the presence of dielectrics and conductors. i. electromagnetic-field response functions and black-body fluctuations in finite geometries. *Phys. Rev. A*, 11:230–242, Jan 1975. URL: <https://link.aps.org/doi/10.1103/PhysRevA.11.230>, doi:10.1103/PhysRevA.11.230.
- [58] C. Henkel, S. Pötting, and M. Wilkens. Loss and heating of particles in small and noisy traps. *Applied Physics B*, 69(5):379–387, Dec 1999. doi:10.1007/s003400050823.
- [59] Kanupriya Sinha and Yiğit Subaşı. Quantum brownian motion of a particle from casimir-polder interactions. *Physical Review A*, 101(3), mar 2020. URL: <https://doi.org/10.1103/PhysRevA.101.032507>, doi:10.1103/PhysRevA.101.032507.
- [60] Lukas Martinetz, Klaus Hornberger, and Benjamin A. Stickler. Surface-induced decoherence and heating of charged particles. *PRX Quantum*, 3:030327, Aug 2022. URL: <https://link.aps.org/doi/10.1103/PRXQuantum.3.030327>, doi:10.1103/PRXQuantum.3.030327.
- [61] E. M. Purcell. Spontaneous Emission Probabilities at Radio Frequencies. *Physical Review*, 69:681, 1946. URL: <http://link.aps.org/doi/10.1103/PhysRev.69.674.2>, doi:10.1103/PhysRev.69.674.2.
- [62] K. H. Drexhage, H. Kuhn, and F. P. Schäfer. Variation of the fluorescence decay time of a molecule in front of a mirror.

- Berichte der Bunsengesellschaft für physikalische Chemie*, 72(2):329–329, 1968. URL: <https://onlinelibrary.wiley.com/doi/abs/10.1002/bbpc.19680720261>, arXiv:<https://onlinelibrary.wiley.com/doi/pdf/10.1002/bbpc.19680720261>, doi:10.1002/bbpc.19680720261.
- [63] P. Goy, J. M. Raimond, M. Gross, and S. Haroche. Observation of cavity-enhanced single-atom spontaneous emission. *Phys. Rev. Lett.*, 50:1903–1906, Jun 1983. URL: <https://link.aps.org/doi/10.1103/PhysRevLett.50.1903>, doi:10.1103/PhysRevLett.50.1903.
- [64] Daniel Kleppner. Inhibited spontaneous emission. *Phys. Rev. Lett.*, 47:233–236, Jul 1981. URL: <https://link.aps.org/doi/10.1103/PhysRevLett.47.233>, doi:10.1103/PhysRevLett.47.233.
- [65] Eli Yablonovitch. Inhibited spontaneous emission in solid-state physics and electronics. *Phys. Rev. Lett.*, 58:2059–2062, May 1987. URL: <https://link.aps.org/doi/10.1103/PhysRevLett.58.2059>, doi:10.1103/PhysRevLett.58.2059.
- [66] A. Blanco, C. López, R. Mayoral, H. Miguez, F. Meseguer, A. Mifsud, and J. Herrero. Cds photoluminescence inhibition by a photonic structure. *Applied Physics Letters*, 73(13):1781–1783, 1998. arXiv: <https://doi.org/10.1063/1.122280>, doi:10.1063/1.122280.
- [67] Paul Adrien Maurice Dirac. *The Principles of Quantum Mechanics*. Oxford,: Clarendon Press, 1930.
- [68] William L Barnes, Simon A R Horsley, and Willem L Vos. Classical antennas, quantum emitters, and densities of optical states. *Journal of Optics*, 22(7):073501, jun 2020. URL: <https://doi.org/10.1088/2040-8986/22/7/073501>, doi:10.1088/2040-8986/22/7/073501.
- [69] Michael Motsch, Martin Zeppenfeld, Pepijn W H Pinkse, and Gerhard Rempe. Cavity-enhanced rayleigh scattering. *New J. Phys.*, 12(6):063022, jun 2010. URL: <http://dx.doi.org/10.1088/1367-2630/12/6/063022>, doi:10.1088/1367-2630/12/6/063022.

- [70] Kasey J. Russell, Tsung-Li Liu, Shanying Cui, and Evelyn L. Hu. Large spontaneous emission enhancement in plasmonic nanocavities. *Nature Photonics*, 6(7):459–462, Jul 2012. doi:[10.1038/nphoton.2012.112](https://doi.org/10.1038/nphoton.2012.112).
- [71] Kosmas L. Tsakmakidis, Robert W. Boyd, Eli Yablonovitch, and Xiang Zhang. Large spontaneous-emission enhancements in metallic nanostructures: towards leds faster than lasers. *Opt. Express*, 24(16):17916–17927, Aug 2016. URL: <https://opg.optica.org/oe/abstract.cfm?URI=oe-24-16-17916>, doi:[10.1364/OE.24.017916](https://doi.org/10.1364/OE.24.017916).
- [72] Sandro Mignuzzi, Stefano Vezzoli, Simon A. R. Horsley, William L. Barnes, Stefan A. Maier, and Riccardo Sapienza. Nanoscale design of the local density of optical states. *Nano Letters*, 19(3):1613–1617, 2019. PMID: 30786717. arXiv:<https://doi.org/10.1021/acs.nanolett.8b04515>, doi:[10.1021/acs.nanolett.8b04515](https://doi.org/10.1021/acs.nanolett.8b04515).
- [73] Lukas Maiwald, Timo Sommer, Mikhail S. Sidorenko, Ruslan R. Yafyasov, Meraj E. Mustafa, Marvin Schulz, Mikhail V. Rybin, Manfred Eich, and Alexander Yu. Petrov. Control over light emission in low-refractive-index artificial materials inspired by reciprocal design. *Advanced Optical Materials*, 10(1):2100785, 2022. URL: <https://onlinelibrary.wiley.com/doi/abs/10.1002/adom.202100785>, arXiv:<https://onlinelibrary.wiley.com/doi/pdf/10.1002/adom.202100785>, doi:[10.1002/adom.202100785](https://doi.org/10.1002/adom.202100785).
- [74] Suli Wu, Hongbo Xia, Jiahui Xu, Xiaoqian Sun, and Xiaogang Liu. Manipulating luminescence of light emitters by photonic crystals. *Advanced Materials*, 30(47):1803362, 2018. URL: <https://onlinelibrary.wiley.com/doi/abs/10.1002/adma.201803362>, arXiv:<https://onlinelibrary.wiley.com/doi/pdf/10.1002/adma.201803362>, doi:[10.1002/adma.201803362](https://doi.org/10.1002/adma.201803362).
- [75] M. D. Leistikow, A. P. Mosk, E. Yeganegi, S. R. Huisman, A. Lagendijk, and W. L. Vos. Inhibited spontaneous emission of quantum dots

observed in a 3d photonic band gap. *Phys. Rev. Lett.*, 107:193903, Nov 2011. URL: <https://link.aps.org/doi/10.1103/PhysRevLett.107.193903>, doi:10.1103/PhysRevLett.107.193903.

- [76] J B Pendry. Shearing the vacuum - quantum friction. *Journal of Physics: Condensed Matter*, 9(47):10301–10320, nov 1997. doi:10.1088/0953-8984/9/47/001.
- [77] Jean-Philippe Mulet, Karl Joulain, Rémi Carminati, and Jean-Jacques Greffet. Enhanced radiative heat transfer at nanometric distances. *Microscale Thermophysical Engineering*, 6(3):209–222, 2002. arXiv:<https://doi.org/10.1080/10893950290053321>, doi:10.1080/10893950290053321.
- [78] Stefan Yoshi Buhmann and Dirk-Gunnar Welsch. Dispersion forces in macroscopic quantum electrodynamics. *Progress in Quantum Electronics*, 31(2):51–130, 2007. URL: <https://www.sciencedirect.com/science/article/pii/S0079672707000249>, doi:10.1016/j.pquantelec.2007.03.001.
- [79] Andrew Zangwill. *Modern electrodynamics*. Cambridge Univ. Press, Cambridge, 2013. URL: <https://cds.cern.ch/record/1507229>.
- [80] Leonard Mandel and Emil Wolf. *Optical Coherence and Quantum Optics*. Cambridge University Press, 1995. doi:10.1017/CB09781139644105.
- [81] G. Hétet, L. Slodička, A. Glätzle, M. Hennrich, and R. Blatt. Qed with a spherical mirror. *Physical Review A*, 82(6), Dec 2010. URL: <http://dx.doi.org/10.1103/PhysRevA.82.063812>, doi:10.1103/physreva.82.063812.
- [82] Felix Tebbenjohanns, Martin Frimmer, and Lukas Novotny. Optimal position detection of a dipolar scatterer in a focused field. *Phys. Rev. A*, 100:043821, Oct 2019. URL: <https://link.aps.org/doi/10.1103/PhysRevA.100.043821>, doi:10.1103/PhysRevA.100.043821.

- [83] Simin Feng and Herbert G. Winful. Physical origin of the gouy phase shift. *Opt. Lett.*, 26(8):485–487, Apr 2001. URL: <https://opg.optica.org/ol/abstract.cfm?URI=ol-26-8-485>, doi:10.1364/OL.26.000485.
- [84] G. Cerchiari, L. Dania, D. S. Bykov, R. Blatt, and T. E. Northup. Position measurement of a dipolar scatterer via self-homodyne detection. *Phys. Rev. A*, 104:053523, Nov 2021. URL: <https://link.aps.org/doi/10.1103/PhysRevA.104.053523>, doi:10.1103/PhysRevA.104.053523.
- [85] Christopher C. Davis. *The optics of Gaussian beams*, page 438–480. Cambridge University Press, 2 edition, 2014. doi:10.1017/CB09781139016629.016.
- [86] Masud Mansuripur and Per K. Jakobsen. Electromagnetic radiation and the self-field of a spherical dipole oscillator. *American Journal of Physics*, 88(9):693–703, 09 2020. arXiv:https://pubs.aip.org/aapt/ajp/article-pdf/88/9/693/13110082/693_1_online.pdf, doi:10.1119/10.0001348.
- [87] Lukas Novotny. Radiation damping of a polarizable particle. *Physical Review A*, 96(3), Sep 2017. URL: <http://dx.doi.org/10.1103/PhysRevA.96.032108>, doi:10.1103/physreva.96.032108.
- [88] L. Novotny, M. Frimmer, A. Militaru, A. Norrman, O. Romero-Isart, and P. Maurer. Optomechanical sideband asymmetry explained by stochastic electrodynamics. *Phys. Rev. A*, 106:043511, Oct 2022. URL: <https://link.aps.org/doi/10.1103/PhysRevA.106.043511>, doi:10.1103/PhysRevA.106.043511.
- [89] G. Araneda, G. Cerchiari, D. B. Higginbottom, P. C. Holz, K. Lakhmanskiy, P. Obšil, Y. Colombe, and R. Blatt. The Panopticon device: An integrated Paul-trap–hemispherical mirror system for quantum optics. *Review of Scientific Instruments*, 91(11):113201, 11 2020. arXiv:<https://pubs.aip.org/aip/rsi/article-pdf/doi/10.>

1063/5.0020661/15965079/113201_1_online.pdf, doi:10.1063/5.0020661.

- [90] Lorenzo Dania, Katharina Heidegger, Dmitry S. Bykov, Giovanni Cerchiari, Gabriel Araneda, and Tracy E. Northup. Position measurement of a levitated nanoparticle via interference with its mirror image. *Phys. Rev. Lett.*, 129:013601, Jun 2022. URL: <https://link.aps.org/doi/10.1103/PhysRevLett.129.013601>, doi:10.1103/PhysRevLett.129.013601.
- [91] Yannick Weiser, Tommaso Faorlin, Lorenz Panzl, Thomas Lafenthaler, Lorenzo Dania, Dmitry S. Bykov, Thomas Monz, Rainer Blatt, and Giovanni Cerchiari. Back action suppression for levitated dipolar scatterers, 2024. [arXiv:2402.04802](https://arxiv.org/abs/2402.04802).
- [92] Jakob Hüpfel, Felix Russo, Lukas M. Rachbauer, Dorian Bouchet, Junjie Lu, Ulrich Kuhl, and Stefan Rotter. A continuity equation for the flow of fisher information in electromagnetic scattering. In *CLEO 2023*, page FW4D.4. Optica Publishing Group, 2023. URL: https://opg.optica.org/abstract.cfm?URI=CLEO_FS-2023-FW4D.4, doi:10.1364/CLEO_FS.2023.FW4D.4.
- [93] Felix Tebbenjohanns, Andrei Militaru, Andreas Norrman, Fons van der Laan, Lukas Novotny, and Martin Frimmer. Optimal orientation detection of an anisotropic dipolar scatterer. *Phys. Rev. A*, 105:053504, May 2022. URL: <https://link.aps.org/doi/10.1103/PhysRevA.105.053504>, doi:10.1103/PhysRevA.105.053504.
- [94] Michael A Taylor, Joachim Knittel, and Warwick P Bowen. Fundamental constraints on particle tracking with optical tweezers. *New Journal of Physics*, 15(2):023018, feb 2013. URL: <https://dx.doi.org/10.1088/1367-2630/15/2/023018>, doi:10.1088/1367-2630/15/2/023018.
- [95] Jorge R. Zurita-Sánchez, Jean-Jacques Greffet, and Lukas Novotny. Friction forces arising from fluctuating thermal fields. *Phys. Rev. A*,

- 69:022902, Feb 2004. URL: <https://link.aps.org/doi/10.1103/PhysRevA.69.022902>, doi:10.1103/PhysRevA.69.022902.
- [96] C Henkel, K Joulain, J-P Mulet, and J-J Greffet. Radiation forces on small particles in thermal near fields. *Journal of Optics A: Pure and Applied Optics*, 4(5):S109, aug 2002. URL: <https://dx.doi.org/10.1088/1464-4258/4/5/356>, doi:10.1088/1464-4258/4/5/356.
- [97] T. Seberson and F. Robicheaux. Distribution of laser shot-noise energy delivered to a levitated nanoparticle. *Phys. Rev. A*, 102:033505, Sep 2020. URL: <https://link.aps.org/doi/10.1103/PhysRevA.102.033505>, doi:10.1103/PhysRevA.102.033505.
- [98] Mohammad Ali Abbassi and Khashayar Mehrany. Inclusion of the backaction term in the total optical force exerted upon rayleigh particles in nonresonant structures. *Phys. Rev. A*, 98:013806, Jul 2018. URL: <https://link.aps.org/doi/10.1103/PhysRevA.98.013806>, doi:10.1103/PhysRevA.98.013806.
- [99] Thomas Agrenius, Carlos Gonzalez-Ballester, Patrick Maurer, and Oriol Romero-Isart. Interaction between an optically levitated nanoparticle and its thermal image: Internal thermometry via displacement sensing. *Phys. Rev. Lett.*, 130:093601, Feb 2023. URL: <https://link.aps.org/doi/10.1103/PhysRevLett.130.093601>, doi:10.1103/PhysRevLett.130.093601.
- [100] Daniel B. Higginbottom, Geoff T. Campbell, Gabriel Araneda, Fengzhou Fang, Yves Colombe, Ben C. Buchler, and Ping Koy Lam. Fabrication of ultrahigh-precision hemispherical mirrors for quantum-optics applications. *Scientific Reports*, 8(1):221, Jan 2018. doi:10.1038/s41598-017-18637-8.
- [101] Yuk Tung Liu and Kip S. Thorne. Thermoelastic noise and homogeneous thermal noise in finite sized gravitational-wave test masses. August 2000. doi:10.1103/PhysRevD.62.122002.

- [102] Jan Gieseler, Romain Quidant, Christoph Dellago, and Lukas Novotny. Dynamic relaxation of a levitated nanoparticle from a non-equilibrium steady state. *Nature Nanotechnology*, 9(5):358–364, May 2014. doi: [10.1038/nnano.2014.40](https://doi.org/10.1038/nnano.2014.40).
- [103] Vijay Jain. *Levitated optomechanics at the photon recoil limit*. Phd thesis, ETH Zurich, 2017. Available at <https://www.research-collection.ethz.ch/handle/20.500.11850/200312>.
- [104] M. Kamba, H. Kiuchi, T. Yotsuya, and K. Aikawa. Recoil-limited feedback cooling of single nanoparticles near the ground state in an optical lattice. *Phys. Rev. A*, 103:L051701, May 2021. URL: <https://link.aps.org/doi/10.1103/PhysRevA.103.L051701>, doi: [10.1103/PhysRevA.103.L051701](https://doi.org/10.1103/PhysRevA.103.L051701).
- [105] T. A. Savard, K. M. O’Hara, and J. E. Thomas. Laser-noise-induced heating in far-off resonance optical traps. *Phys. Rev. A*, 56:R1095–R1098, Aug 1997. URL: <https://link.aps.org/doi/10.1103/PhysRevA.56.R1095>, doi: [10.1103/PhysRevA.56.R1095](https://doi.org/10.1103/PhysRevA.56.R1095).
- [106] Eric D. Black. An introduction to Pound–Drever–Hall laser frequency stabilization. *American Journal of Physics*, 69(1):79–87, 01 2001. arXiv:https://pubs.aip.org/aapt/ajp/article-pdf/69/1/79/10115998/79_1_online.pdf, doi: [10.1119/1.1286663](https://doi.org/10.1119/1.1286663).
- [107] William L Barnes, Simon A R Horsley, and Willem L Vos. Classical antennas, quantum emitters, and densities of optical states. *Journal of Optics*, 22(7):073501, jun 2020. doi: [10.1088/2040-8986/ab7b01](https://doi.org/10.1088/2040-8986/ab7b01).
- [108] Mohammad Ali Abbassi and Khashayar Mehrany. Green’s-function formulation for studying the backaction cooling of a levitated nanosphere in an arbitrary structure. *Phys. Rev. A*, 100:023823, Aug 2019. URL: <https://link.aps.org/doi/10.1103/PhysRevA.100.023823>, doi: [10.1103/PhysRevA.100.023823](https://doi.org/10.1103/PhysRevA.100.023823).

- [109] Chris Dawson and James Bateman. Spectral analysis and parameter estimation in levitated optomechanics. *J. Opt. Soc. Am. B*, 36(6):1565–1573, Jun 2019. URL: <https://opg.optica.org/josab/abstract.cfm?URI=josab-36-6-1565>, doi:10.1364/JOSAB.36.001565.
- [110] Hannes Risken. *Fokker-Planck Equation*, pages 63–95. Springer Berlin Heidelberg, Berlin, Heidelberg, 1996. doi:10.1007/978-3-642-61544-3_4.
- [111] Muddassar Rashid, Marko Toroš, Ashley Setter, and Hendrik Ulbricht. Precession motion in levitated optomechanics. *Phys. Rev. Lett.*, 121:253601, Dec 2018. URL: <https://link.aps.org/doi/10.1103/PhysRevLett.121.253601>, doi:10.1103/PhysRevLett.121.253601.
- [112] Chris Dawson. *Spectral Analysis and Parameter Estimation in Fibre Levitated Optomechanics*. Phd thesis, Swansea University, 2020.
- [113] Gambhir Ranjit, David P. Atherton, Jordan H. Stutz, Mark Cunningham, and Andrew A. Geraci. Attonewton force detection using microspheres in a dual-beam optical trap in high vacuum. *Phys. Rev. A*, 91:051805, May 2015. URL: <https://link.aps.org/doi/10.1103/PhysRevA.91.051805>, doi:10.1103/PhysRevA.91.051805.
- [114] Mitsuyoshi Kamba, Ryoga Shimizu, and Kiyotaka Aikawa. Optical cold damping of neutral nanoparticles near the ground state in an optical lattice. *Opt. Express*, 30(15):26716–26727, Jul 2022. URL: <https://opg.optica.org/oe/abstract.cfm?URI=oe-30-15-26716>, doi:10.1364/OE.462921.
- [115] Gambhir Ranjit, Mark Cunningham, Kirsten Casey, and Andrew A. Geraci. Zeptonewton force sensing with nanospheres in an optical lattice. *Phys. Rev. A*, 93:053801, May 2016. URL: <https://link.aps.org/doi/10.1103/PhysRevA.93.053801>, doi:10.1103/PhysRevA.93.053801.

- [116] M. T. Homer Reid and S. G. Johnson. Efficient Computation of Power, Force, and Torque in BEM Scattering Calculations. *ArXiv e-prints*, July 2013. [arXiv:1307.2966](https://arxiv.org/abs/1307.2966).
- [117] [http://github.com/homerreid/scuff-EM](https://github.com/homerreid/scuff-EM).
- [118] P. Z. G. Fonseca, E. B. Aranas, J. Millen, T. S. Monteiro, and P. F. Barker. Nonlinear dynamics and strong cavity cooling of levitated nanoparticles. *Phys. Rev. Lett.*, 117:173602, Oct 2016. URL: <https://link.aps.org/doi/10.1103/PhysRevLett.117.173602>, doi: [10.1103/PhysRevLett.117.173602](https://doi.org/10.1103/PhysRevLett.117.173602).
- [119] Alex R. Dow, Ashley M. Wittrig, and Hilkka I. Kenttämä. Laser-induced acoustic desorption mass spectrometry. *European Journal of Mass Spectrometry*, 18(2):77–92, 2012. [arXiv:https://doi.org/10.1255/ejms.1162](https://arxiv.org/abs/https://doi.org/10.1255/ejms.1162), doi: [10.1255/ejms.1162](https://doi.org/10.1255/ejms.1162).
- [120] Peter Asenbaum, Stefan Kuhn, Stefan Nimmrichter, Ugur Sezer, and Markus Arndt. Cavity cooling of free silicon nanoparticles in high vacuum. *Nature Communications*, 4(1):2743, Nov 2013. doi: [10.1038/ncomms3743](https://doi.org/10.1038/ncomms3743).
- [121] Mathieu L. Juan, Reuven Gordon, Yuanjie Pang, Fatima Eftekhari, and Romain Quidant. Self-induced back-action optical trapping of dielectric nanoparticles. *Nature Physics*, 5(12):915–919, December 2009. doi: [10.1038/nphys1422](https://doi.org/10.1038/nphys1422).
- [122] Lukas Neumeier, Romain Quidant, and Darrick E Chang. Self-induced back-action optical trapping in nanophotonic systems. *New Journal of Physics*, 17(12):123008, dec 2015. doi: [10.1088/1367-2630/17/12/123008](https://doi.org/10.1088/1367-2630/17/12/123008).
- [123] Jr. Kowalevich, Andrew M, and Frank Bucholtz. Beam divergence from an smf-28 optical fiber. *Naval Research Laboratory, Washington, DC*, 2006.

- [124] Felix Tebbenjohanns, Martin Frimmer, Andrei Militaru, Vijay Jain, and Lukas Novotny. Cold damping of an optically levitated nanoparticle to microkelvin temperatures. *Phys. Rev. Lett.*, 122:223601, Jun 2019. URL: <https://link.aps.org/doi/10.1103/PhysRevLett.122.223601>, doi: 10.1103/PhysRevLett.122.223601.
- [125] M. Iwasaki, T. Yotsuya, T. Naruki, Y. Matsuda, M. Yoneda, and K. Aikawa. Electric feedback cooling of single charged nanoparticles in an optical trap. *Phys. Rev. A*, 99:051401, May 2019. URL: <https://link.aps.org/doi/10.1103/PhysRevA.99.051401>, doi:10.1103/PhysRevA.99.051401.
- [126] Bruno Melo, Marc T. Cuairan, Grégoire F. M. Tomassi, Nadine Meyer, and Romain Quidant. Vacuum levitation and motion control on chip. *Nature Nanotechnology*, Jun 2024. doi:10.1038/s41565-024-01677-3.
- [127] Allan W. Snyder and John D. Love. *Optical Waveguide Theory*. Springer US, 1984. doi:10.1007/978-1-4613-2813-1.
- [128] Professor Joseph M. Kahn. Ee-247: Introduction to optical fiber communications, lecture 3: Wave optics description of optical fibers, Autumn 2006-07.
- [129] A. Kowalewicz and F. Bucholtz. Beam divergence from an smf-28 optical fiber. 2006.
- [130] *Corning® SMF-28® Ultra Optical Fibers: Product Information*. URL: <https://www.corning.com/optical-communications/emea/en/home/products/fiber/optical-fiber-products/smf-28-ultra.html>.
- [131] Sumiaty Ambran, Christopher Holmes, James C. Gates, Andrew S. Webb, Lewis G. Carpenter, Faisal Rafiq Mahamd Adikan, Peter G. R. Smith, and Jayanta K. Sahu. Fabrication of a multimode interference device in a low-loss flat-fiber platform using physical micromachining technique. *J. Lightwave Technol.*, 30(17):2870–2875, Sep 2012. URL: <https://opg.optica.org/jlt/abstract.cfm?URI=jlt-30-17-2870>.

- [132] Christopher Holmes, James C Gates, Lewis G Carpenter, Helen L Rogers, Richard M Parker, Peter A Cooper, Sima Chaotan, Faisal R Mahamd Adikan, Corin B E Gawith, and Peter G R Smith. Direct uv-written planar bragg grating sensors. *Measurement Science and Technology*, 26(11):112001, oct 2015. URL: <https://dx.doi.org/10.1088/0957-0233/26/11/112001>, doi:10.1088/0957-0233/26/11/112001.
- [133] David William Hempston. *Force detection in levitated optomechanics*. Phd thesis, University of Southampton, 2017. Available at <https://eprints.soton.ac.uk/418004/>.
- [134] Andreas Daniel Pfister. *An Integrated Fiber-Based Cavity in a Paul Trap*. Phd thesis, Johannes Gutenberg-Universität Mainz, 2019. Available at https://inis.iaea.org/collection/NCLCollectionStore/_Public/51/066/51066654.pdf.
- [135] M Harlander, M Brownutt, W Hänsel, and R Blatt. Trapped-ion probing of light-induced charging effects on dielectrics. *New Journal of Physics*, 12(9):093035, sep 2010. URL: <https://dx.doi.org/10.1088/1367-2630/12/9/093035>, doi:10.1088/1367-2630/12/9/093035.
- [136] Martin Frimmer, Karol Luszcz, Sandra Ferreiro, Vijay Jain, Erik Hebestreit, and Lukas Novotny. Controlling the net charge on a nanoparticle optically levitated in vacuum. *Phys. Rev. A*, 95:061801, Jun 2017. URL: <https://link.aps.org/doi/10.1103/PhysRevA.95.061801>, doi:10.1103/PhysRevA.95.061801.
- [137] *Top Gun, Ionizing Air Gun*. URL: <https://www.simco-ion.co.uk/products/static-eliminators/ionising-guns/top-gun/>.